

https://dspace.org/

Differential measurements of heavy flavours via the semi-muonic decay channel at ALICE using Monte Carlo simulations

Mabitsela, Retsilisitsoe Mokhatla

2025
University of the Witwatersrand, Johannesburg
https://hdl.handle.net/10539/50249

Mabitsela, Retsilisitsoe Mokhatla. (2025). Differential measurements of heavy flavours via the semi-muonic decay channel at ALICE using Monte Carlo simulations [Master's dissertation, University of the Witwatersrand, Johannesburg]. WIReDSpace. https://hdl.handle.net/10539/50249

Downloaded from a DSpace repository. https://dspace.org/



Differential measurements of heavy flavours via the semi-muonic decay channel at ALICE using Monte Carlo simulations

by

Retsilisitsoe Mokhatla Mabitsela

(323246)

Dissertation

submitted to the Faculty of Science, University of the Witwatersrand, Johannesburg, in fulfilment of the requirements for the degree of

Master of Science

in

High Energy Physics

Supervisor:
Prof. Zinhle Buthelezi

Co-Supervisors:
Dr. Siegfried Förtsch

October 31, 2025

Declaration

I declare that this thesis is my own, unaided work. It is being submitted for the Degree of Master of Science at the University of the Witwatersrand, Johannesburg. It has not been submitted before for any degree or examination at any other University.



(Retsilisitsoe Mokhatla Mabitsela)
Student Number: 323246

Date: October 31, 2025
Place: University of the Witwatersrand

Abstract

Heavy quarks (charm and bottom/beauty quarks), produced during the early stages of high-energy particle collisions with high momentum transfer and short formation time, provide unique probes for studying both the quark-gluon plasma (QGP) and the internal structure of protons due to their flavour conservation in strong interactions. Proton-proton collisions at ultra-relavistic energies serve as essential baseline measurements for studying quantum chromodynamics (QCD) and establishing references for more complex nucleus-nucleus collision systems.

This thesis employs Monte Carlo simulations to investigate heavy-quark production via their hadronisation into open heavy-flavour hadrons, which subsequently decay via the semi-muonic channel, in proton-proton (pp) collisions at the ALICE experiment at the Large Hadron Collider (LHC) at CERN. Detailed comparisons of inclusive single muon differential cross-sections and heavy-flavour decay muon differential cross-sections at centre-of-mass energies of $\sqrt{s} = 5.02$ TeV and $\sqrt{s} = 13$ TeV, at forward pseudorapidity ($-4 \leq \eta \leq -2.5$), are presented. The study encompasses systematic comparisons between standalone PYTHIA 8 simulations and integrated simulations that incorporate PYTHIA and GEANT3 to describe ALICE detector transport. Additionally, this work investigates the impact of different parton distribution functions (PDFs), specifically NNPDF2.3 and CTEQ6.6M, on the simulated yields.

The results are analysed in terms of transverse momentum (p_{T}) differential cross-sections ($\mathrm{d}\sigma/\mathrm{d}p_{\mathrm{T}}$), with particular focus on the normalised yields ($1/N_{\mathrm{evt}} \times \mathrm{d}N/\mathrm{d}p_{\mathrm{T}}$) as a function of p_{T}. The Monte Carlo simulation calculations are ultimately compared with experimental data from ALICE Run 2 (2015-2018) and theoretical perturbative QCD predictions from Fixed-Order Next-to-Leading-Logarithm (FONLL) calculations, providing insights into the accuracy of current theoretical frameworks and simulation tools in describing heavy-quark production at LHC energies.

Dedicated

to

Uncle Johnny Mabitsela, who radiated until his final state... Uncle Siegie Lehmann & Auntie Dolly Lehmann, whose charm and beauty may never decay... If I could project time, I would reverse the drift so that our paths would collide once again...

Acknowledgements

I would like to express my sincere gratitude to everyone who supported me throughout my MSc journey.

First and foremost, my deepest thanks to my supervisors, Prof. Zinhle Buthelezi and Dr. Siegie Foertsch, for their unwavering patience, guidance, and mentorship. Your support, understanding, and encouragement, especially through my challenges and setbacks, have been invaluable. Thank you for giving me the space and time needed to complete my thesis and for believing in my potential. I am truly grateful for your wisdom, dedication, and for seeing me through this journey.

I would also like to extend my gratitude to DSI-NRF, NRF iThemba LABS SA-ALICE, SA-CERN, CERN, and ALICE for their support and collaboration. The partnership between South Africa and CERN has not only advanced my research but has also contributed significantly to building scientific capacity and fostering innovation.

A heartfelt thank you to Wits University for providing me with the opportunity to pursue my qualification and for offering an environment conducive to learning and growth.

Lastly, I would like to acknowledge my family, friends, and colleagues who stood by me through every high and low. Your understanding, encouragement, and love have kept me going.

Thank you all for making this achievement possible.

Contents

Abstract i

List of Figures vi

List of Tables 1

1 Introduction 2
- 1.1 Motivations . . . 2
- 1.2 The Standard Model . . . 4
  - 1.2.1 Families of Elementary Particles in the Standard Model . . . 6
  - 1.2.2 Leptons and the Electromagnetic Interaction . . . 8
  - 1.2.3 Quarks and the Strong Interaction . . . 11
- 1.3 Quantum Chromodynamics . . . 15
  - 1.3.1 QCD Theory . . . 15
  - 1.3.2 Parton Distribution Functions . . . 17
- 1.4 Aims of this Study . . . 24
- 1.5 Thesis Outline . . . 26

2 Heavy-Flavour Studies and the ALICE Experiment 28
- 2.1 pp Collisions and Heavy Flavours . . . 28
  - 2.1.1 pp Collisions . . . 28
  - 2.1.2 Heavy Flavours . . . 31
  - 2.1.3 pQCD in Heavy-Flavour Studies . . . 33
- 2.2 The ALICE Detector . . . 34

2.2.1 The Inner Tracking System (ITS) . . . 37
2.2.2 Central Barrel Forward Detectors . . . 43
2.2.3 The Forward Muon Spectrometer . . . 46
2.3 The ALICE Offline Framework . . . 51
2.3.1 AliRoot . . . 51
2.3.2 The Virtual Monte Carlo . . . 53
2.3.3 Simulation . . . 54
2.3.4 Reconstruction . . . 55

3 Monte Carlo Simulations in PYTHIA 56
3.1 Monte Carlo Event Generators . . . 56
3.2 Overview of PYTHIA . . . 58
3.2.1 PYTHIA 6 and PYTHIA 8 . . . 59
3.2.2 Data Analysis . . . 60
3.2.3 Limitations of PYTHIA . . . 60
3.3 Programme Flow . . . 61
3.4 The Event Record . . . 64
3.5 Particle Data . . . 64
3.6 Tunes . . . 65
3.7 Hard Processes and Parton Showers . . . 66
3.8 Hadronisation . . . 68
3.8.1 Fragmentation . . . 69
3.8.2 Colour reconnection . . . 69
3.9 Particle Decays . . . 70
3.9.1 Complications in Particle Decays . . . 71

4 Analysis Details 72
4.1 Overview . . . 72
4.2 Standalone PYTHIA 8 Monte Carlo Simulations . . . 73
4.2.1 Simulation Strategy . . . 73
4.2.2 Muon Selection . . . 73
4.2.3 Differential Single Muon Yield Determination . . . 75
4.3 ALICE Monte Carlo Productions with AliROOT . . . 78
4.3.1 ALICE MC Productions Using AliROOT & PYTHIA . . . 78
4.3.2 Differential Single Muon Yield Determination . . . 79
4.4 Normalised Differential Yields . . . 82
4.4.1 Analysis of the Centre-of-Mass Energy Dependence . . . 83
4.4.2 Analysis of PDF Dependence . . . 89
4.4.3 Analysis of the Effects of PYTHIA Versions . . . 92
4.4.4 Effects of Accurate Detector Simulation . . . 95

4.5 Differential Cross-Sections 98

5 Discussion of Results and Conclusion **100**

5.1 Results 100

5.2 Conclusion 106

5.3 Outlook 108

References **113**

List of Figures

1.1 Overview of the Standard Model of Elementary Particles. The diagram categorises all known elementary particles into three generations of fermions (quarks and leptons) and bosons (gauge and scalar). Mass, charge, and spin values are specified for each particle, highlighting the fundamental differences and similarities across generations and particle types [1]. 6

1.2 Parton Distribution Functions (PDFs) for different partons (u, d, s, c, b, and gluons) as a function of Bjorken-x at two different scales: (a) $Q^2 = 10\,\mathrm{GeV}^2$ and (b) $Q^2 = 10^4\,\mathrm{GeV}^2$. The gluon distribution is scaled down by a factor of 10 for clarity.[2] 19

2.1 The CERN accelerator complex is a network of accelerators designed to accelerate particles to high energies (6.5 TeV for Run 2). The Large Hadron Collider (LHC) is instrumental in conducting four major experiments: ALICE (A Large Ion Collider Experiment) ATLAS (A Toroidal LHC ApparatuS; CMS (Compact Muon Solenoid); and LHCb (LHC Beauty), in addition to hosting a range of smaller-scale experiments which include TOTEM, LHCf, MoEDAL-MAPP, FASER, and SND@LHC.[3][4][5] 29

2.2 The ALICE detector in Run 2. This figure illustrates the central barrel and muon spectrometer, along with their various subdetectors. The ALICE detector locates events and particles inside the detector using Cartesian and cylindrical coordinates. The Interaction Point (IP), where collisions between accelerated particle beams from the LHC occur, serves as the origin of the Cartesian coordinate system and is located precisely in the middle of the ALICE detector's central barrel. Using Figure 2.1 as a reference, the x-axis runs directly from the origin to the LHC ring's centre. The y-axis extends straight from the origin towards the Earth's surface. The z-axis points from the IP and runs parallel to the LHC's beam path. The z-axis' positive side is designated the A-side and is in the direction of the ATLAS detector. The negative side is the C-side and is in the direction of the CMS detector. The Cartesian and cylindrical systems share a z-axis specification with its origin at the IP. However, these coordinates use the azimuthal angle (ϕ) (which is the angle measured in the xy plane) as well as the radial distance (r) - which is the distance travelled in a straight line from a point to the origin. The Central Barrel spans 360° (or 2π radians) in the ϕ direction and is symmetrically positioned around the IP. The Muon Spectrometer is located on the C-side.[6][7] 35
2.3 Schematic of the ALICE ITS.[8] 38
2.4 Schematic of the SPD barrels and a half-stave: The sensors (silicon pixels) in the SPD are responsible for detecting the charged particles. The Multi-Chip Module (MCM) processes the data collected by the pixels. The bus is a pathway that transmits signals from the pixels to the Multi-Chip Module. The grounding foil electrically isolates the half-stave, preventing any unwanted electrical interactions.[9] 39
2.5 The ALICE SDD layout features two drift regions, each with 256 collection anodes, 33 charge injectors for drift velocity monitoring, and separate voltage dividers.[8] 41
2.6 A schematic of the ALICE Muon Spectrometer.[10] 46
2.7 A schematic side view of the ALICE muon spectrometer demonstrating the paths of two muons.[11] 47
2.8 The organisation of AliRoot framework comprises of various base classes and interfaces for third-party external packages.[12] 52
2.9 The organisation of AliRoot framework comprises of various base classes and interfaces for third-party external packages.[12] 54

3.1 Pythia 8.3 programme structure with its main C++ classes.[13] 62

3.2 A visual representation of a particle collision event, as predicted by a Monte Carlo simulation. At the core of the interaction, indicated by a central red node, is the primary hard collision. Radiating from this point is a branching structure of lines and nodes, illustrating the process of Bremsstrahlung, where secondary particles are emitted, modeled here by parton showers. A secondary hard collision is highlighted by a purple node, indicating another point of significant interaction. The transformation from partons into hadrons is marked by transitions shown with light green nodes. The decays of these hadrons are denoted by dark green nodes. Additionally, the graphic includes yellow lines which denote the emission of soft photon radiation, a low-energy byproduct of the collision and decay processes.[14] . 68

4.1 The computed transverse momentum distributions of all muons (inclusive) before and after kinematic cuts were applied (5.02 TeV left, 13 TeV right). Kinematically, muons with pseudorapidities (η) ranging from -4.0 to -2.5, transverse momenta (p_{T}) from 0.5 GeV/c to 20.0 GeV/c, and momenta (p) from 4.0 GeV/c up to 100 million GeV/c were selected. Geometrically, they had polar angles (θ) from 2.98451 rad to 3.10669 rad, and azimuthal angles (ϕ) between 0 and 2π rad. Additionally, muons originating within 100mm of the primary vertex and having mother particles with PDG IDs between 400 and 599 (indicating heavy quarks) were considered. 76

4.2 The transverse momentum yield distributions of muons from all primary decay sources at $\sqrt{s} = 13$ TeV, after kinematic cuts were applied (standalone PYTHIA 8). This figure delineates the contributions from distinct primary sources: pions (green circles), primary kaons (blue circles), charm (orange circles), beauty (yellow circles), and the sum of all other primary muon sources (red circles). The black line represents the total inclusive muon yield (sum) of the individual sources. 77

4.3 width=14cm 82

4.4 Normalised transverse momentum distribution of all muons (inclusive) for all PDFs in ALICE AliROOT MC productions, covering centre-of-mass energy levels of $\sqrt{s} = 5.02$ TeV and $\sqrt{s} = 13$ TeV. The values of N for the ALICE AliROOT MC productions are stated in Tables 4.3 and 4.4. Note that for $p_{\mathrm{T}} > 8.0$ GeV/c, there are limited statistics for AliROOT with PYTHIA (ALICE MC productions), unlike the case of standalone PYTHIA 8 shown in Figure 4.3. 83

4.5 Comparison of the normalised transverse momentum distributions of all muons from decays of primary particles (total), comparing yields at two centre-of-mass energy, $\sqrt{s}$ = 5.02 TeV and $\sqrt{s}$ = 13 TeV. The left plot illustrates yields from standalone PYTHIA 8 MC productions using the NNPDF2.3 PDF. The right plot depicts results from ALICE PYTHIA 8 MC productions using AliROOT, using the NNPDF2.3 PDF. The bottom pane contains ratio histograms of the normalised yields at $\sqrt{s}$ = 5.02 TeV (numerator) and $\sqrt{s}$ = 13 TeV (denominator). The dotted blue and red lines represent the respective maximum values of the ratios for standalone PYTHIA 8 and ALIROOT. The dotted black line is a reference line to aid with visually comparing the ratios to unity. 84

4.6 Comparison of the normalised transverse momentum distributions of muons from charm, at centre-of-mass energies $\sqrt{s}$ = 5.02 TeV and $\sqrt{s}$ = 13 TeV. The left plot illustrates the normalised yield distributions were computed from standalone PYTHIA 8 Monte Carlo simulations using the NNPDF2.3 PDF. The right plot illustrates the normalised yield distributions were computed from AliROOT with PYTHIA 8, using the NNPDF2.3 PDF. The bottom plot comprises ratios of the normalised yield distributions at $\sqrt{s}$ = 5.02 TeV (numerator) and $\sqrt{s}$ = 13 TeV (denominator). The respective maximum values of the ratios for standalone PYTHIA 8 and ALIROOT are represented by the dotted blue and red lines. The dotted black line indicates unity. 86

4.7 Comparison of the normalised transverse momentum distributions of muons beauty decays, at centre-of-mass energies $\sqrt{s}$ = 5.02 TeV and $\sqrt{s}$ = 13 TeV. The left plot illustrates the normalised yield distributions were computed from standalone PYTHIA 8 Monte Carlo simulations using the NNPDF2.3 PDF. The right plot illustrates the normalised yield distributions were computed from AliROOT with PYTHIA 8, using the NNPDF2.3 PDF. 87

4.8 Comparison of the normalised transverse momentum distributions of all muons from decays of primary particles (total) between PDFs ($\sqrt{s}$ = 13 TeV). The left plot compares normalised yields from standalone PYTHIA 8 MC productions using the CTEQ6.6 and NNPDF2.3 PDFs. The right plot compares normalised yields from standalone PYTHIA 8 MC productions using the NNPDF2.3 and NNPDF3.0 PDFs. 89

4.9 Comparison of the normalised transverse momentum distributions muons from decays of heavy flavours (at centre-of-mass energy $\sqrt{s}$ = 5.02 TeV and $\sqrt{s}$ = 13 TeV). The left plot compares normalised yield distributions from charm decays using standalone PYTHIA 8 with the CTEQ6.6 and NNPDF2.3 PDFs for $\sqrt{s}$ = 5.02. The right plot compares normalised yield distributions from charm decays using standalone PYTHIA 8 with the CTEQ6.6 and NNPDF2.3 PDFs for $\sqrt{s}$ = 13 90

4.10 Normalised transverse momentum distributions of muons from charm (left) and beauty (right) decays, comparing the differences between PYTHIA 6 (CTEQ5) and PYTHIA 8 (NNPDF2.3) at centre-of-mass energy $\sqrt{s}$ = 5.02 TeV, using AliROOT. 93

4.11 Normalised transverse momentum distributions of muons from charm (left) and beauty (right) decays, comparing the effects of accurate detector simulation (AliROOT with PYTHIA 8 and NNPDF2.3) and standalone PYTHIA 8 with NNPDF2.3 ($\sqrt{s}$ = 5.02 TeV). 96

5.1 Differential cross-section distributions of heavy-flavour muons as a function of transverse momentum at $\sqrt{s}$ = 5.02 TeV (left) and $\sqrt{s}$ = 13 TeV (right). The black points represent Run 2 experimental data from ALICE from LHC15n [15], and ongoing studies from LHC18d, LHC18e, LHC18f, LHC18l and LHC18m run periods. The data from 2018 only includes statistical uncertainties [16]. 101

5.2 The black points and lines represent experimental data from ALICE Run 2, including LHC15n [15], LHC18d, LHC18e, LHC18f, LHC18l and LHC18m run periods (with statistical uncertainties only) [16]. Theoretical predictions from FONLL pQCD calculations using the CTEQ6.6 PDF are shown for various contributions: total heavy-flavour muon production (grey solid line), beauty-to-muon decays (red dashed line), charm-to-muon decays (green dashed line), and beauty-to-charm-to-muon cascade decays (blue dashed line). The figure compares experimental data with FONLL calculations and PYTHIA 8 standalone simulations using NNPDF2.3 (orange histogram). The measurements were performed in the pseudorapidity range $-4 < \eta < -2.5$. 103

5.3 Ratios of the differential cross-section $d\sigma/dp_T$ for standalone PYTHIA 8 (NNPDF2.3) to experimental data, and FONLL (CTEQ6.6) to experimental data. The measurements were performed in the pseudorapidity range $-4 < \eta < -2.5$ at $\sqrt{s}$ = 5.02 TeV and $\sqrt{s}$ = 13 TeV. 105

4 Pythia 8.3 programme structure with its main C++ classes.[13] 130

List of Tables

2.1 Properties of open heavy-flavour particles 32

4.1 Key configuration settings in Pythia 8 74
4.2 Selection criteria for muons of interest categorised by cut types. 75
4.3 Simulation parameters for 5.02 TeV ALICE MC productions 78
4.4 Simulation parameters for 13 TeV ALICE MC production 78

CHAPTER 1

Introduction

1.1 Motivations

The study of Quantum Chromodynamics (QCD) and the properties of the quark-gluon plasma (QGP) lies at the heart of the research conducted by the ALICE experiment [8]. At the high energy densities achieved at the Large Hadron Collider (LHC)[17], QCD predicts that a short-lived, hot, and dense fluid-like state of matter known as the quark-gluon plasma is formed, in which quarks and gluons move quasi-freely, temporarily liberated from colour confinement.[18] This state is believed to have existed microseconds after the Big Bang, offering a unique window into the early universe's conditions [17].

The study of QCD and the properties of the QGP lies at the heart of the research conducted by the ALICE experiment [8]. At the high energy densities achieved at the Large Hadron Collider (LHC)[17], QCD predicts that a short-lived, hot, and dense fluid-like state of matter known as the QGP is formed. In this state, quarks and gluons move quasi-freely, temporarily liberated from colour confinement.[18] This state is believed to have existed microseconds after the Big Bang, providing insights into the physics of the early universe [17]. While the temperature and energy density at the LHC are lower than in the early universe, studying this QGP state provides insights into the behaviour of deconfined quark-gluon matter.

The study of the QGP involves observing the behaviour of particles as they interact with

this medium. Experiments at the LHC and the Relativistic Heavy Ion Collider (RHIC) [19][20][21] have demonstrated that the QGP behaves as a nearly perfect fluid with an extremely low shear viscosity to entropy density ratio [22][23]. Certain particles, particularly heavy quarks, such as charm and bottom (beauty), serve as excellent probes to study the QGP. At high energies, pp collisions can be described as the collisions of individual quarks or gluons, also called partons [24]. Because heavy quarks are produced in the early hard scatterings of partons, they are present before the formation of the QGP. Their large masses make them less susceptible to thermal production and annihilation within the QGP, while also reducing their interaction rate with the medium. These characteristics allow them to traverse the evolving QGP medium and experience its entire space-time evolution. Subsequently, heavy quarks hadronise through coalescence with light quarks at the critical temperature or through fragmentation, forming heavy-flavour hadrons [25]. Heavy quarks therefore serve as invaluable probes for studying the QGP, particularly through measurements of the suppression and enhancement of heavy-flavour hadron production cross sections (hadrons containing at least one charm or bottom/beauty quark). In pp collisions, heavy-flavour production provides critical tests for perturbative QCD (pQCD) calculations, including Fixed Order Next-to-Leading Logarithms (FONLL) [26] and other next-to-leading-order frameworks.

At ALICE, the QGP is generated in heavy-ion collisions involving lead-lead (Pb-Pb) nuclei [27]. However, baseline measurements for heavy-flavour production are conducted in pp collisions at the same centre-of-mass energy. Without the effects of nuclei, pp collisions serve as references that enable the isolation of QGP effects on the modification of heavy-flavour production.

The semi-muonic decay channel is one of the preferred ways of measuring heavy-flavour production spectra, especially single muon decays because muons produce a clear and easily detectable experimental signal. Due to the relatively large mass of muons and lifetime, and primarily electromagnetic interactions, muons can travel long distances before decaying and traverse substantial amounts of detector material and absorbers with minimal energy loss. These characteristics make muons ideal particles for identifying and reconstructing trajectories, providing clear signals in detectors. The ALICE detector's forward muon spectrometer is equipped to measure single and dimuon events with high precision [8]. However, heavy-flavour muon spectra are contaminated by significant background contributions from the decays of light hadrons (primarily pions and kaons) and electroweak bosons in the low- and high momentum regions, respectively. Due to the inclusive nature of these muon measurements, it is challenging to distinguish the sources of these decays, preventing the direct separation of heavy-flavour decay muons from other sources.

Monte Carlo simulations are crucial for studying heavy-flavours at ALICE, primarily for estimating background signals and detector effects. Such simulations involve replicating the ALICE detector's responses to create realistic collision events that mirror real-world data. While Monte Carlo methods require significant computational resources and have limited transverse momentum (p_{T}) reach, the present research aims to evaluate their effectiveness in estimating heavy-flavour production cross sections. Comparisons with experimental data from ALICE Run 2 and FONLL pQCD calculations [28] will determine the potential of Monte Carlo simulations as a complementary tool in heavy-flavour analysis. Such an approach may provide new insights into the relative performance of theoretical predictions, experimental measurements, and simulation techniques in the study of heavy-flavour physics in high-energy nuclear collisions.

The rest of this chapter will briefly discuss the background of the Standard Model of fundamental particles and the role of QCD, state the study's aims, and provide an outline of this thesis.

1.2 The Standard Model

The quest to understand the universe and its fundamental constituents is one of humanity's oldest and most profound endeavours. From the first Homo sapiens gazing at the stars to modern physicists probing the fabric of reality, we have been driven by a great curiosity to answer fundamental questions. What is the universe made of? What is matter? How does everything work, and what compels this "everything" to work this way consistently? The Standard Model of Particle Physics represents the culmination of this grand quest, encapsulating science's best understanding of the fundamental particles and forces that govern the universe. The 21st century is an era where many of these age-old questions have found answers, thanks to an unprecedented acceleration of discoveries, particularly during the 20th century, a golden age of physics that saw a flourishing of groundbreaking ideas and experiments.

This chapter aims to celebrate these legacies while demystifying the complex concepts they developed, making the marvels of particle physics accessible and exciting to all curious minds. The task of understanding the universe at its most fundamental level is fraught with logical and philosophical challenges, especially when defining basic concepts such as matter and energy.

For now, a simple definition suffices: matter is physical "stuff" that has the potential to do "something" and occupies non-zero volume, while energy is a fundamental aspect of physical reality that we have no better way to describe. Whether or not it is accepted that matter is just stuff that takes up space and has energy (and is energy too), the main

point is to think of this "stuff" as being made of smaller "things" called "atoms." Atoms are building blocks of matter, but they are not truly fundamental. They can be considered fundamental at a macroscopic scale, which is referred to as the atomic scale, the focus of chemistry. Although it is now understood that an atom is composed of even smaller objects—protons, neutrons, and electrons—an atom is indivisible in the sense that these individual components cannot exist on their own, only as part of an atom. This is an oversimplification, of course. For example, simplest element, hydrogen, which is made up of only one proton and one electron, can exist in the H^+ state where the electron has been stripped off, an ion.

The smallest "things" in the universe come together to form larger and more complex structures, but understanding the nature of these interactions raises several fundamental questions. What causes these smaller "things" to stick together in the first place? Atoms, for instance, combine in various ways, forming molecules and compounds. This "invisible glue" that binds them is the result of fundamental forces and interactions. To delve deeper into these interactions, we must consider the concept of "fundamental forces." A fundamental force, or interaction, is one that cannot be reduced to more basic interactions. There are four known fundamental forces in nature: gravity, electromagnetism, the strong nuclear force, and the weak nuclear force. These forces govern the behaviour of particles and the formation of matter at all scales.

- **Gravity**: The weakest of the four forces; it acts over long distances and is responsible for the attraction between masses.
- **Electromagnetism**: This force acts between charged particles, governing the behaviour of electrons and protons in atoms.
- **Strong Nuclear Force**: The strongest force; holds the nucleons of atoms together, overcoming the repulsive force between positively charged protons. It also holds the quarks together in hadrons.
- **Weak Nuclear Force**: Describes radioactive decay and certain nuclear reactions.

The Standard Model of particle physics encapsulates our understanding of these fundamental forces (excluding gravity) and the elementary particles that constitute matter. It describes how particles interact through these forces, providing a framework for understanding the behaviour of matter at the smallest scales. This description of physics boils down to defining matter and fundamental forces/interactions in their most fundamental units. Both matter and forces can be described in terms of "particles," which creates the framework that is called the Standard Model of Physics. This model, while incredibly successful, is still incomplete and continues to be refined as new discoveries are made.

1.2.1 Families of Elementary Particles in the Standard Model

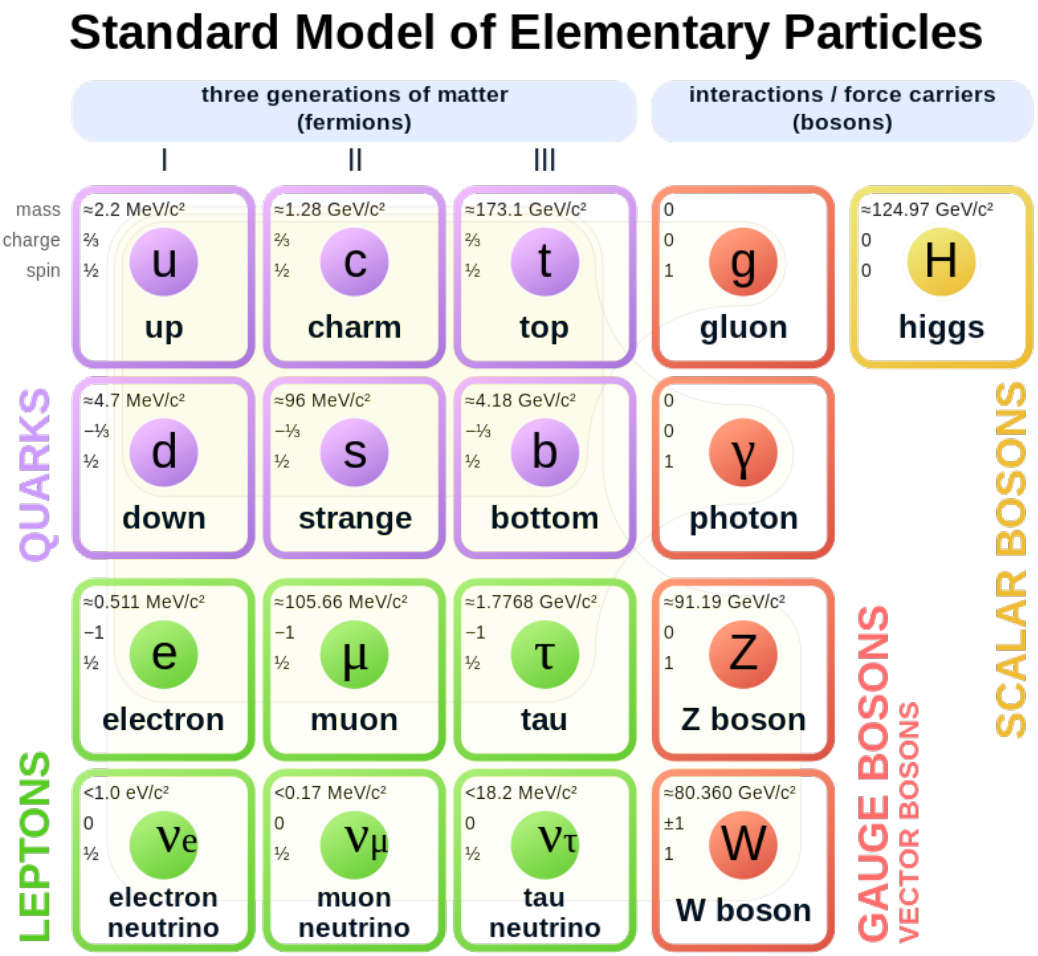


Figure 1.1: Overview of the Standard Model of Elementary Particles. The diagram categorises all known elementary particles into three generations of fermions (quarks and leptons) and bosons (gauge and scalar). Mass, charge, and spin values are specified for each particle, highlighting the fundamental differences and similarities across generations and particle types [1].

The Standard Model of physics (illustrated in Figure 1.1) is ultimately a system of mathematical equations describing the behaviour and interactions of subatomic particles. As the most rigorously tested and accurate scientific theory to date, it is the cornerstone of our understanding of the universe [29]. This framework not only elucidates how elementary particles interact through fundamental forces but also provides a foundation for comprehending the universe's structure and behaviour at its most basic level. While the quantum revolution of the early 20th century abruptly challenged classical notions of predictability, the development of the Standard Model was a gradual process. It emerged

through the collective efforts of numerous physicists over several decades, piece by piece forming a new order in our understanding of particle physics [30].

The Standard Model categorises fundamental particles into distinct families: leptons, quarks, and bosons. Leptons and quarks are collectively known as fermions. These particles are grouped according to fundamental properties such as mass and electrical charge. However, a less familiar but crucial property called "spin" plays a vital role in the organisation of the Standard Model. Spin, here, also referred to as a quantum state, is a fundamental property of subatomic particles, and differs significantly from the macroscopic concept of rotation. Rather than physical spinning, it represents an intrinsic angular momentum – an inherent characteristic independent of a particle's motion through space. Thus, the spin should not be a concept that one visualises but should be understood as a fundamental property that influences particle behaviour in magnetic fields and interactions with other particles, much like electric charge determines electromagnetic interactions.

Particles with intrinsic spin possess a magnetic moment because of their angular momentum. In the presence of a magnetic field, the spin of a particle interacts with the field through this magnetic moment, resulting in torque that causes the spin vector to undergo rotational motion, called precession, around the direction of the magnetic field. The quantum mechanical nature of spin leads to quantisation of spin states, resulting in discrete energy levels (the Zeeman effect) [31][32][33][34].

Ultimately, spin can be used to classify the families of fundamental particles of the standard model. The term "fermion," derived from the surname of the Italian physicist Enrico Fermi, was coined by the English theoretical physicist Paul Dirac [35]. Fermions are particles that obey the Pauli exclusion principle and possess half-odd-integer spin values (1/2, 3/2, etc.). This category includes both elementary particles, such as electrons, and composite particles, such as protons. Conversely, the term "boson," named by Dirac in honour of Indian physicist Satyendra Nath Bose, refers to particles with integer spin values (0, 1, 2, etc.) [36]. Elementary bosons, such as gluons, act as force carriers, mediating interactions between other particles. The Higgs boson, uniquely, contributes to the phenomenon of mass. Not all bosons are elementary particles. While fundamental bosons like photons, W/Z bosons, gluons, and the Higgs boson are elementary particles in the Standard Model, mesons are composite bosons because they are composed of quarks. However, in general, when the term boson is used, it is usually used in reference to the elementary particles.

Leptons are a family of elementary particles that do not feel the strong interaction and possess unique quantum mechanical properties that have profound implications for their physical characteristics. The lepton family comprises six known particles, arranged in

three generations. A charged lepton is paired with a corresponding neutral lepton (or neutrino) in each generation. The electron and its neutrino form the first generation, followed by the muon and muon neutrino in the second generation, and the tauon and tau neutrino in the third. Charged leptons participate in various physical phenomena, including atomic structure and decay processes, while neutrinos, being electrically neutral, interact primarily through the weak nuclear force. The generations exhibit an increasing mass pattern, with the electron being the lightest and the tauon the heaviest of the charged leptons [29][33][34][37].

Quarks, also fermions, mirror leptons in their generational structure [38]. Each of the three generations contains two types of quark, with masses increasing from one generation to the next [39]. Up- and down quarks, forming the first generation, are the primary components of protons and neutrons. The second generation's charm and strange quarks appear in higher-mass particles produced in high-energy environments such as interacting cosmic rays or particle accelerator-induced reactions. The top and bottom quarks of the third generation, due to their substantial mass and brief lifespans, are typically observed mainly in advanced high-energy physics experiments [40].

The Standard Model recognises five elementary bosons [30]. The Higgs boson, with spin 0, plays a crucial role in the phenomenon of mass through the Higgs mechanism, which imparts mass to elementary particles such as the W and Z bosons and fundamental fermions (quarks and leptons) by their interactions with the Higgs field [41]. Four spin-1 bosons act as force carriers: the photon mediates the electromagnetic force, eight types of gluon carry the strong force, and the neutral and charged weak bosons (Z and W$\pm$) are responsible for the weak force [42]. While a spin-2 boson called the graviton has been proposed as the force carrier for gravity, efforts to integrate gravity into the Standard Model have thus far been unsuccessful [43].

1.2.2 Leptons and the Electromagnetic Interaction

Leptons and quarks are integral to the structure and function of the universe, from the stability of atoms to the dynamics of cosmic phenomena. The interactions between fermions are largely governed by the electromagnetic force, alongside the strong nuclear force, weak nuclear force, and gravity [44]. The electromagnetic force acts between particles that exhibit a property known as electric charge. Electrons, for instance, are negatively charged, whereas protons (composed of positively charged up- and negatively charged down quarks) are positively charged. The designation of positive and negative is somewhat arbitrary. These terms simply represent opposite states: particles with like charges repel each other, and those with opposite charges attract, and these interactions are mediated by photons [45]. There is also a neutral charge state, which does not engage in electromagnetic inter-

actions but can still participate in other fundamental forces. Charged particles interact electromagnetically, influencing everything from the stability of atoms to the complex mechanisms of biological systems and technological devices. The electromagnetic force itself is mediated by photons, which are electrically neutral but are integral in facilitating these interactions [44].

Understanding the electromagnetic force's role and its mediation by photons is vital. This force not only binds electrons to atomic nuclei but also orchestrates the interactions of particles at all scales, from atomic to cosmic. The arbitrary nature of charge definition underscores the deeper principles of symmetry and balance that are central to modern physics. The concept of electric charge is central to the study of electromagnetism, a field with a rich and complex history. The unification of electric and magnetic forces into a single theory of electromagnetism was achieved by James Clerk Maxwell in the 1860s [46]. Magnetism, initially thought to be distinct, was later understood to be deeply interconnected with electricity. This connection was evident in phenomena such as electromagnetism, where electric currents create magnetic fields, and vice versa. This interplay was quantitatively described by Maxwell's equations, highlighting that changing electric fields could induce magnetic fields, and moving magnets could produce electricity [44].

By the early 1930s, the fundamental picture of particle physics had become relatively straightforward. Atoms were understood to be composed of protons and neutrons in the nucleus, with electrons orbiting this central mass. The neutron, discovered by James Chadwick in 1932, completed this basic atomic model [47]. However, the discovery of new particles soon complicated this picture. The muon, discovered by Carl D. Anderson and Seth Neddermeyer in 1936, was the first hint of a more complex subatomic world [48]. Initially mistaken for the theorised meson because of its mass, the muon was eventually understood to be a heavier cousin of the electron, forming the second generation of leptons.

Around the same time, the concept of the neutrino was developing. In 1930, Wolfgang Pauli proposed the existence of a neutral, nearly massless particle to explain the continuous energy spectrum observed in beta decay [49]. Enrico Fermi later named this particle the "neutrino" [50]. As the understanding of leptons grew, so did the realisation that each charged lepton might have an associated neutrino. The electron neutrino proposed by Pauli was the first. In 1962, the existence of the muon neutrino was demonstrated by Leon M. Lederman, Melvin Schwartz, and Jack Steinberger, showing that more than one type of neutrino existed [51]. This discovery, which earned them the 1988 Nobel Prize, established the concept of neutrino flavours corresponding to the known leptons. The picture was completed with the discovery of the tau lepton by Martin Lewis Perl and his colleagues between 1974 and 1977 [52]. Like the electron and muon, the tau was also expected to have an associated neutrino. Evidence for the tau neutrino came

from observations of "missing" energy and momentum in tau decay, analogous to the phenomena that led to the discovery of the electron neutrino. Thus, three generations of leptons were established, each consisting of a charged lepton (electron, muon, tau) and its corresponding neutrino (electron neutrino, muon neutrino, tau neutrino) [53].

This generational structure became a fundamental aspect of the Standard Model of particle physics. The experimental detection of neutrinos proved challenging due to their weak interactions with matter. The first confirmation of neutrino detection came in 1956 from Clyde Cowan and Frederick Reines, a discovery that later earned Reines a share of the 1995 Nobel Prize in Physics [54][55]. Another milestone occurred in 1965 when Reines and his team detected the first naturally occurring neutrinos in a deep underground experiment [56]. The final piece of the neutrino puzzle fell into place in 2000 when the DONUT collaboration at Fermilab announced the first direct detection of tau neutrino interactions [49]. This made the tau neutrino the second-to-last particle of the Standard Model to be directly observed, with only the Higgs boson, which was ultimately discovered at the LHC in 2012 [57].

The concept of antimatter, which plays a crucial role in our understanding of particle physics, emerged from theoretical predictions and was later confirmed through experimental discoveries. Each fermion has a corresponding antiparticle with the same mass but opposite charge and other quantum numbers. In 1928, Paul Dirac's work on reconciling quantum mechanics with special relativity led to the theoretical prediction of antimatter [35]. His equations suggested the existence of a positively charged electron, which seemed paradoxical at the time. This theoretical prediction was dramatically confirmed in 1932 when Carl Anderson discovered the positron while analysing cosmic rays [52]. The positron, identical to the electron in mass but opposite in charge, provided the first experimental evidence of antimatter, revolutionising our understanding of particle physics. Following the positron's discovery, scientists began searching for other antiparticles. The antiproton was discovered in 1955 by Emilio Segrè and Owen Chamberlain at the University of California, Berkeley, using the Tevatron particle accelerator [58]. This discovery earned them the Nobel Prize in Physics in 1959. The antineutron was discovered shortly thereafter, in 1956, by Bruce Cork et al., also using the Tevatron [59]. Despite being electrically neutral like the neutron, the antineutron can be distinguished by its opposite magnetic moment and its ability to annihilate with ordinary matter.

Antiparticles of other fermions were either discovered or inferred as new particles were found. The antimuon, for instance, was observed in cosmic rays, while the existence of antineutrinos was confirmed through reactor experiments [60]. The discovery of antimatter particles completed the picture of fermions in the Standard Model, with each matter particle having an antimatter counterpart. This symmetry between matter and antimat-

ter remains one of the most intriguing aspects of particle physics, particularly given the observed matter-antimatter asymmetry in the universe [61].

1.2.3 Quarks and the Strong Interaction

Hadrons are subatomic particles that are essential components of the universe's matter. Unlike molecules held together by electromagnetic forces, hadrons are composed of quarks and are bound together by the strong force, a fundamental force of nature that is extremely powerful over very short distances [38]. This category includes particles such as protons and neutrons. Hadrons are categorised into two broad families based on the number of quarks they contain: baryons and mesons [62]. Baryons, including well-known particles like protons and neutrons, are composed of an odd number of quarks—usually three. This odd-number configuration is essential for defining a baryon. On the other hand, mesons are made up of an even number of quarks, specifically a quark and an antiquark pair. This pairing of quarks and antiquarks characterises all mesons, such as pions, which play a critical role in mediating the strong force that holds the atomic nucleus together [63]. The specific properties of hadrons, such as their mass and charge, are largely determined by their quark composition, referred to as valence quarks [24]. For instance, a proton is made up of two up quarks and one down quark. Each up quark carries a positive charge of $+\frac{2}{3}$, while the down quark has a negative charge of $-\frac{1}{3}$. Summing these charges $+\frac{2}{3} + \frac{2}{3} - \frac{1}{3} = +1$, the overall charge of the proton is +1.

In recent years, physics experiments have revealed "exotic" hadrons that contain more than three quarks, challenging previous understandings of quark combinations [64]. For example, a tetraquark consists of four quarks (two quarks and two antiquarks), and was first discovered in 2007 by the Belle Collaboration and later confirmed by the LHCb collaboration in 2014 [65]. Additionally, the LHCb collaboration discovered two types of pentaquarks in 2015, which consist of five quarks [66]. These discoveries expand the conventional categories of hadrons, introducing new forms of subatomic matter and deepening our understanding of quark interactions.

Before 1971, the binding mechanism of atomic nuclei posed a significant puzzle to physicists. It was understood that the nucleus consisted of protons and neutrons—protons being positively charged and neutrons electrically neutral [67]. According to classical physics, the like charges of protons should repel each other strongly enough to shatter the nucleus. However, atomic nuclei are notably stable, suggesting the presence of another, even stronger force. This realisation led to the postulation of the strong nuclear force, a fundamental force that acts between protons and neutrons, collectively known as nucleons, to hold the nucleus together despite the repulsive electromagnetic forces among protons [68]. The strong nuclear force, or nuclear force, is predominantly attractive and is

what binds nucleons together to form the nucleus of an atom. It acts powerfully over very short distances—about 0.8 femtometres (or 0.8×10^{-15} metres). Beyond approximately 2.5 fm, the force diminishes rapidly and becomes negligible, helping to limit the size of the nucleus [69]. Interestingly, at distances shorter than 0.7 fm, the nuclear force becomes repulsive, preventing nucleons from being crushed into each other. This repulsion sets a lower limit on how close nucleons can be packed, ultimately influencing the overall size of the nucleus [70].

In 1935, Hideki Yukawa made a significant theoretical breakthrough by predicting the existence of mesons based on his analyses of the relationship between the mass of a force-mediating particle and the range of the force it mediates [63]. Yukawa postulated that a particle with a certain mass must exist to carry the strong nuclear force over a limited range within the nucleus. Initially, the discovery of the muon in 1936, which was then referred to as the "mu meson," seemed to confirm Yukawa's prediction because its mass was within the expected range [71]. However, subsequent experiments revealed that the muon did not participate in the strong nuclear interactions. It was not until 1947 that Cecil Powell experimentally discovered the pion, which correctly fit the criteria for Yukawa's meson and mediated the strong nuclear force [72].

The quark model was independently proposed in 1964 by the physicists Murray Gell-Mann and George Zweig [38][62]. Zweig referred to the elementary particles as "aces," while Gell-Mann named them "quarks." This model fundamentally changed the understanding of particle physics by suggesting that baryons (which include protons and neutrons) and mesons are composed of these elementary particles. Initially, the model included three types of quark: up, down, and strange, which accounted for the composition and properties of most known hadrons. By the 1970s, further development in particle physics led to a deeper understanding of the strong nuclear force. Contrary to earlier beliefs that it was a fundamental force, it became apparent that what was observed as the strong nuclear force was actually an emergent phenomenon from a more fundamental force known as the strong interaction. This interaction, governed by the theory of quantum chromodynamics (QCD), confines quarks within protons, neutrons, and other hadrons [73]. In QCD, quarks carry a property termed "colour charge," a metaphorical term with no visual implication, which governs their interaction. Quarks with different colour charges attract each other due to the strong interaction, and the gluon is the particle responsible for mediating this force [39].

In 1968, groundbreaking experiments at the Stanford Linear Accelerator Center (SLAC) revealed that protons are composed of smaller, point-like objects, challenging the notion that protons were elementary particles [74]. Initially, physicists were hesitant to label these constituents as quarks, a term proposed in theoretical models. Instead, Richard

Feynman introduced the term "partons" to describe these fundamental components [24]. These objects observed at SLAC were later identified as up and down quarks as the quark model developed and other quark flavours were discovered. The term "parton" continues to be used broadly to refer to the components of hadrons, including quarks, antiquarks, and gluons.

The existence of another component of the Gell-Mann and Zweig three-quark model, the strange quark, was indirectly validated through these scattering experiments at SLAC. Its necessity was underscored by its role in explaining the properties of kaons (K) and pions (π), which had been discovered in cosmic rays as early as 1947 [75].

Further theoretical advancements were made in the early 1970s. Sheldon Glashow and James Bjorken proposed additions to the Gell-Mann–Zweig model, predicting another flavour of quark, termed "charm" [76]. In 1970, Glashow, together with John Iliopoulos and Luciano Maiani, developed a theoretical framework that proposed the necessity of the charm quark, which had not yet been discovered [77].

The charm quark was finally observed in November 1974, almost simultaneously, by two research teams, one led by Burton Richter at SLAC, and the other by Samuel Ting at Brookhaven National Laboratory [78][79]. The observations identified mesons comprising charm quarks and charm antiquarks, which are notably recognised in particles initially named with two symbols, J and ψ, but officially known as the J/ψ meson.

The quark model expanded to include six flavours by 1973 when Makoto Kobayashi and Toshihide Maskawa noted that their experimental observations could be explained by the presence of two additional quarks [80]. The first to name these additional quarks as "top" and "bottom" was Haim Harari in a 1975 paper [81]. The bottom quark was subsequently observed in 1977 by a team at Fermilab led by Leon Lederman [82], which strongly suggested the existence of its partner, the top quark. However, it was not until 1995 that the top quark was finally observed at Fermilab, revealing a mass much larger than anticipated, comparable to that of a gold atom [83].

In the early 1970s, Murray Gell-Mann, along with Harald Fritzsch and Heinrich Leutwyler, introduced the field theory of Quantum Chromodynamics (QCD), a significant advance in the understanding of subatomic interactions [73]. QCD was proposed to describe how quarks and gluons interact within hadrons. Central to QCD is the concept of colour charge, analogous to electric charge in electromagnetism, but with unique properties distinguishing it from any other kind of charge.

Unlike electric charge, which is observed as either positive or negative, colour charge in QCD comes in three types: red, blue, and green, as well as their corresponding anticolours:

anti-red, anti-blue, and anti-green [73]. This property of colour charge leads to complex interactions within the nucleus. The gluon, the boson responsible for mediating the strong interaction between quarks, possesses a colour charge, enabling it not only to mediate but also to participate in the strong interaction. This dual role differentiates gluons from photons (the mediators of electromagnetic force), which carry no electric charge and, therefore, do not participate in electromagnetic interactions.

A fundamental aspect of QCD is that the total colour charge of a free particle must be neutral. Quarks and gluons always combine in such a way that the resulting particle, whether a baryon or a meson, is colour-neutral. For instance, baryons are made up of three quarks, each carrying a different colour, and mesons consist of a quark and an antiquark with opposing colour charges, ensuring that all hadrons are colour-neutral [84].

Gluons themselves are subject to the principles of colour charge. Although there are theoretically nine possible combinations of colour and anticolour for gluons, only eight types are independent in QCD due to the way colour fields combine [85]. These eight types of gluons each carry a mix of colour and anticolour, such as red-antired, blue-antiblue, and so forth. This complexity allows gluons to bind quarks together in configurations that form stable particles, despite the inherently chaotic nature of colour interactions.

The introduction of QCD profoundly changed our understanding of the fundamental forces and particles that constitute the universe. By explaining the strong interaction in terms of colour charge and gluons, QCD provided a framework that not only describes how quarks are held within protons and neutrons but also predicts the existence of other types of particles and interactions [86]. This theory remains a cornerstone of modern particle physics and continues to influence new theories and discoveries in the field. The development of QCD and the understanding of colour charge are pivotal in explaining why the atomic nucleus does not fly apart despite the intense repulsive forces between the positively charged protons it contains [87]. By comprehending these complex interactions, scientists can better grasp the fundamental structures and forces that orchestrate the universe at the most microscopic levels.

Each of the four fundamental forces – strong, weak, electromagnetic, and gravitational – is associated with specific mediator bosons:

- The electromagnetic interaction is mediated by photons. Charged leptons (electrons, muons, and taus) possess an electric charge and interact electromagnetically. Neutrinos are electrically neutral, and they do not couple to photons and thus do not experience electromagnetic forces directly. The neutrality of neutrinos with respect to electromagnetic interactions is particularly significant, as it allows these particles to traverse vast cosmic distances largely unimpeded, making them valu-

able probes of astrophysical phenomena [88]. Quarks carry fractional electric charges and participate in electromagnetic interactions, though this is often masked by their confinement within hadrons. Additionally, W bosons carry electric charge, and Z bosons are electrically neutral.

- The strong interaction is mediated by gluons. Quarks carry one of three colour charges (red, green, or blue) and participate strongly in gluon-mediated interactions. Gluons are force carriers, and they possess both colour and anticolour, enabling them to interact with quarks and other gluons. Leptons lack colour charge entirely, rendering them immune to strong interactions. This "colour-blindness" of leptons is a crucial feature that distinguishes them from quarks and plays a significant role in the structure of matter [89]. This explains why electrons, muons, and taus can exist as free particles, while quarks are perpetually confined within hadrons.

- The gravitational force is theoretically mediated by gravitons (but has not yet been observed).

A key aspect of this framework is that only certain particles are susceptible to specific forces, which translates into specific bosons interacting with certain fermions. This selectivity in interactions is a fundamental feature of the Standard Model and explains the diverse behaviour of particles in different contexts. The specificity of these interactions is not arbitrary, but follows from the underlying symmetries and quantum numbers that characterise each particle [33]. An intriguing aspect of force-mediating bosons is their capacity for self-interaction. Generally, bosons do not self-interact, with the notable exception of gluons [84].

1.3 Quantum Chromodynamics

1.3.1 QCD Theory

QCD is the fundamental theory that describes the strong interaction, one of the four fundamental interactions in nature. QCD is a non-Abelian gauge theory rooted in the $SU(3)$ colour symmetry group [90]. Quarks and gluons carry one of three colour charges (red, green, or blue), and gluons are gauge bosons that mediate the strong interaction amongst quarks. Gluons are represented in the adjoint representation of $SU(3)$ and correspond to the eight independent generators of the group. The non-Abelian nature of $SU(3)$ manifests in the non-commutative properties of its generators. For generators T_a and T_b of $SU(3)$, their commutator $[T_a, T_b] = if_{abc}T^c$ is generally non-zero, where f_{abc} are the structure constants of the group. This non-commutativity leads to unique phenomena such as gluon self-interactions, since gluons carry colour charge, unlike Abelian theories

such as Quantum Electrodynamics (QED), where photons do not self-interact [91]. The ability of gluons to interact with each other is a distinctive aspect of QCD, leading to complex phenomena such as colour confinement and asymptotic freedom.[84][92] The $SU(3)$ group consists of 3×3 unitary matrices with determinant 1, which rotate quark colour states (red, green, blue) into superpositions of one another whilst preserving the total probability and colour charge. These rotations form the mathematical foundation of the strong interaction: demanding that physical laws remain unchanged under such colour transformations at every point in spacetime requires the existence of eight gluon fields that mediate the force between quarks. Understanding the $SU(3)$ colour symmetry and its implications is crucial for grasping the rich phenomenology of QCD, including:

The $SU(3)$ group consists of 3×3 unitary matrices with determinant 1, which transform quark colour eigenstates amongst themselves through unitary operations that preserve probability normalisation and colour charge conservation. Local gauge invariance under these colour transformations necessitates the introduction of eight gauge fields corresponding to the group generators, which manifest physically as the gluon fields mediating the strong interaction between quarks.

The $SU(3)$ group consists of 3×3 unitary matrices with determinant 1, which perform transformations on the quark colour states whilst preserving probability conservation and colour charge. The requirement of local gauge invariance under these colour transformations at every spacetime point necessitates the introduction of eight gauge fields, which correspond to the gluons mediating the strong interaction between quarks.

- Asymptotic freedom: the weakening of the strong force at high energies
- Colour confinement: the impossibility of isolating colour-charged particles
- Hadronisation: the process by which quarks and gluons combine to form colour-neutral hadrons

When calculating cross-sections in high-energy collisions, these three phenomena need to be accounted for. Perturbative Quantum Chromodynamics (pQCD) is based on the principle that the strong coupling constant α_s decreases logarithmically with increasing energy scale. This behaviour allows for the application of perturbation theory in QCD calculations at high energies [93]. In high-energy pp collisions at the LHC, collisions are best understood through the parton model, first proposed by Feynman [94]. The proton is not a point-like particle, leading to the assumption that it is composed of smaller point-like constituents. Feynman described hadrons as being made up of these point-like components, known as partons (quarks and gluons). Consequently, hadron collisions can be interpreted as collisions between individual partons.

A crucial concept in pQCD is factorisation, which allows the separation of short-distance (perturbative) and long-distance (non-perturbative) effects. Hadronic cross-sections can be decomposed into perturbatively calculable partonic processes and non-perturbative hadronic structure using the factorisation theorem:

$$\sigma = \sum_{i,j,k} \int dx_1 dx_2 dz \, f_i(x_1, \mu_F^2) f_j(x_2, \mu_F^2) \hat{\sigma}_{ij}(x_1 x_2 s, \mu_F^2, \mu_R^2) D_k(z, \mu_F^2) \tag{1.1}$$

where $f_i(x, \mu_F^2)$ and $f_j(x, \mu_F^2)$ are the parton distribution functions (PDFs) describing the probability of finding a parton of type i or j carrying momentum fraction x of the hadron's momentum, $\hat{\sigma}_{ij}$ is the partonic cross-section for the hard scattering process calculable in perturbative QCD, and $D_k(z, \mu_F^2)$ is the fragmentation function describing how parton k hadronises into particles carrying momentum fraction z. The factorisation scale μ_F separates the perturbative hard scattering from the non-perturbative hadronic structure, while the renormalisation scale μ_R defines the energy scale at which the strong coupling constant α_s is evaluated. This is a universal formulation that can describe hadronic processes as the composition of perturbative interactions and non-perturbative structure encoded that are in PDFs and fragmentation functions.[95]

1.3.2 Parton Distribution Functions

Understanding pp collisions requires a detailed knowledge of proton structure. A proton consists of the following:

- Three valence quarks (two up quarks and one down quark), contributing only about 0.2% of the proton's mass.
- A "sea" of quark-antiquark pairs and gluons account for the majority of the proton's mass and internal dynamics. The gluon field energy constitutes approximately 99.8% of the proton's mass, highlighting the crucial role of gluons in proton structure.

At the core of the QCD explanation of hadron collisions lies the concept of Parton Distribution Functions (PDFs). These functions, denoted as $f_i(x, Q^2)$, describe the probability of finding a parton of type i carrying a momentum fraction x of the proton's total momentum, when probed at an energy scale Q^2 [96]. PDFs serve as the crucial link between theoretical calculations of partonic cross-sections and measurable hadronic cross-sections in collider experiments. They encapsulate the non-perturbative aspects of proton structure and are extracted from global experimental data using phenomenological fits.

In the context of heavy-flavour production in pp collisions, PDFs play a pivotal role by

providing the initial conditions for parton-parton interactions. These interactions occur at high momentum transfer (Q^2), where the strong coupling constant $\alpha_s(Q^2)$ decreases logarithmically with increasing Q^2 (asymptotic freedom), enabling perturbative QCD calculations [84]. The dominant production mechanisms for heavy quarks at LHC energies are gluon-gluon fusion and quark-antiquark annihilation, making the results particularly sensitive to the gluon PDF at low x and high Q^2. At LHC energies, the gluon PDF dominates at low x due to the steep rise in gluon density as x decreases, a feature critical for modelling heavy-flavour production.

Given the critical role of gluons in heavy-flavour production, the choice of PDF set can significantly impact the predicted yields and theoretical consistency across different frameworks. For this study, the comparison of simulation results using different PDF sets, specifically NNPDF2.3 (default in PYTHIA 8.3) and CTEQ6.6M (default in FONLL calculations), provides insight into how PDF uncertainties affect predicted heavy-flavour muon yields. These comparisons are crucial for understanding systematic uncertainties in our measurements and for testing the consistency of different theoretical frameworks.

In the high-energy regime of LHC collisions, the internal dynamics of the colliding protons become relevant. The collision process can be decomposed into several stages, each governed by different aspects of QCD, beginning with initial-state radiation (ISR) and followed by final state radiation (FSR). Prior to the hard scatter, the incoming partons may emit gluons or split into quark-antiquark pairs. This process is described by the Dokshitzer-Gribov-Lipatov-Altarelli-Parisi (DGLAP) evolution equations [97]. The ISR modifies the momentum distribution of the partons entering the hard interaction, affecting the kinematics of the collision.

For example:

- Gluon splitting: $g \to gg$ or $g \to q\bar{q}$
- Quark radiation: $q \to qg$

FSR occurs after the hard scatter, when outgoing partons may emit additional gluons or create quark-antiquark pairs. This process, like ISR, is described by the DGLAP equations and leads to the development of parton showers [98]. The outgoing partons continue to emit QCD radiation as they propagate away from the interaction point. Both ISR and FSR contribute to the development of parton showers, where a single high-energy parton branches into multiple lower-energy partons.

Soft processes involve low momentum transfer and are associated with the underlying event and multiple parton interactions. Although less energetic, soft processes contribute significantly to the overall structure of the event and the multiplicity of particles [99].

Two important concepts for understanding parton interactions are Bjorken-x and momentum transfer. Bjorken-x is a dimensionless variable representing the fraction of the proton's total momentum carried by a particular type of parton. The variable x ranges from 0 to 1 and is crucial in describing the kinematics of deep inelastic scattering and other high-energy processes [100]. Momentum transfer (Q^2) is a quantity that represents the magnitude of the momentum exchanged in the interaction. Higher Q^2 values correspond to harder, more energetic collisions that probe smaller distance scales within the proton.

The NNPDF (Neural Network Parton Distribution Function) collaboration provides sets of PDFs determined using machine learning techniques, specifically neural networks, to extract parton distributions from experimental data. NNPDF3.1 represents their third generation analysis with improved methodology [101]. Figure 1.2 illustrates the NNPDF3.1 NNLO PDFs for different partons as a function of Bjorken-x at two different Q^2 scales. At low x, the density of the gluons increases significantly as Q^2 increases, reflecting the partonic structure of the proton on smaller distance scales.

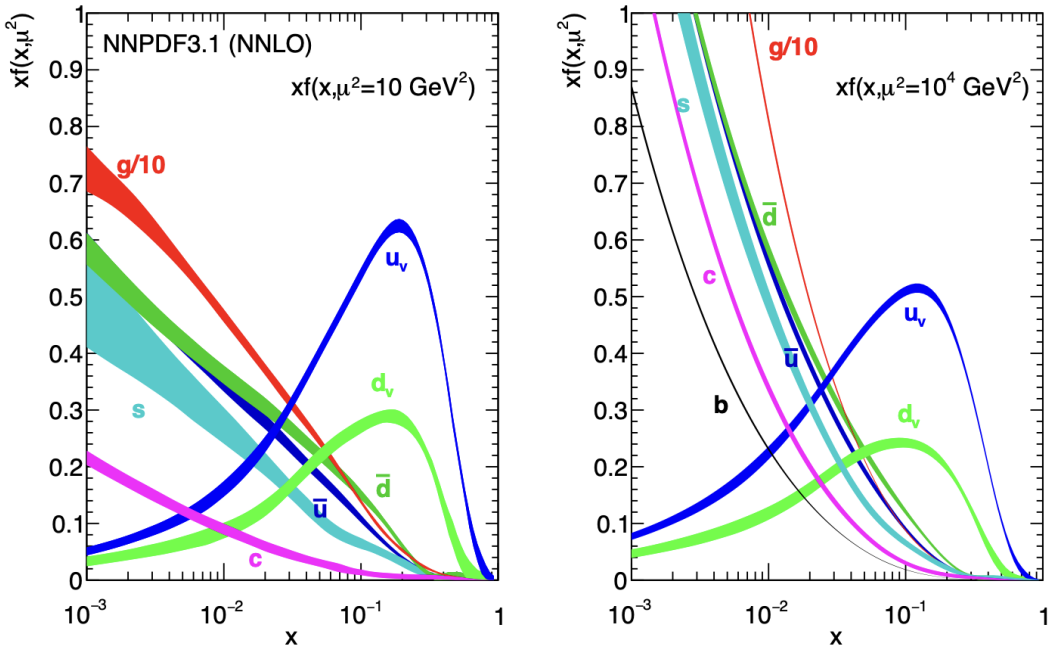


Figure 1.2: Parton Distribution Functions (PDFs) for different partons (u, d, s, c, b, and gluons) as a function of Bjorken-x at two different scales: (a) $Q^2 = 10\,\mathrm{GeV}^2$ and (b) $Q^2 = 10^4\,\mathrm{GeV}^2$. The gluon distribution is scaled down by a factor of 10 for clarity.[2]

Following the hard scatter and parton showers, the process of hadronisation occurs. When partons begin to move away from each other after collision, the force between them intensifies as the energy stored in the strong interaction field increases with distance. At

a certain point, it becomes energetically favourable to create new quark-antiquark pairs from the vacuum. These newly created quarks and antiquarks then combine with the original partons to form colourless hadrons. Although this process occurs at low Q^2 and cannot be perturbatively calculated, it is modelled using phenomenological approaches such as the Lund string model [102]. Hadronisation is the process where partons combine to form colourless hadrons. These hadrons are generally unstable and decay into stable particles such as protons, neutrons, leptons, and neutrinos [103].

The remnants of the protons that did not participate in the hard scatter also interact, collectively referred to as the underlying event (UE), and produce additional particles that contribute to the energy and particle distributions observed in the detector. When two protons collide, typically only one parton from each proton participates in the hard scatter, leaving behind the remaining partons that made up the original protons, which are the beam remnants. These leftover partons carry colour charge and momentum and undergo hadronisation. The underlying event encompasses all these activities not directly associated with the hard scatter, including both the hadronisation of beam remnants and additional soft parton interactions.

Multiple Parton Interactions (MPI) add further complexity to individual collision events. MPIs occur when more than one pair of partons within the same pp collision undergo hard scattering. This leads to increased particle multiplicity and contributes to the overall complexity of the underlying event [104]. These processes significantly influence the energy distribution and particle multiplicity observed in the detector [99].

In high-luminosity environments, an additional experimental challenge arises from pileup, where multiple independent pp collisions occur within the same bunch crossing. This phenomenon increases background noise and complicates event reconstruction, making it challenging to isolate the hard scattering event of interest from the overlapping collision signatures [105].

The physical justification for PDFs stems from the principle of factorisation in Quantum Chromodynamics (QCD) [95]. This principle allows for the separation of short-distance, high-energy interactions of partons from the long-distance, low-energy dynamics within the proton. The key insight is that the timescales of parton interactions within the proton (approximately $1/\Lambda_{QCD}$, where Λ_{QCD} is the QCD scale parameter) are much longer than the timescales of the hard scattering process (approximately $1/Q$). This separation of scales enables the treatment of parton wavefunctions within the proton as effectively frozen during the hard interaction, leading to a probabilistic interpretation of parton distributions [106].

The evolution of PDFs with the energy scale Q^2 is governed by the DGLAP equations

[97]. These equations describe how the parton content of the proton changes at different energy scales, accounting for the phenomenon of Bjorken scaling violation observed in deep inelastic scattering experiments [76]. This scaling violation reveals the dynamic nature of the proton's structure, where gluon radiation and quark-antiquark pair creation become increasingly important at higher energies. The determination of PDFs is a complex task that combines theoretical predictions with experimental data through a process known as global QCD analysis [106].

This analysis can be viewed as a nonlinear regression problem, where the goal is to learn a set of functions (the PDFs) from a diverse range of experimental data. The process involves:

- Parameterisation of PDFs on a starting scale Q_0^2.
- Evolving these PDFs to other scales using the DGLAP equations.
- Calculating observable cross-sections by convolving the evolved PDFs with perturbatively calculated partonic cross-sections.
- Comparing these predictions with experimental data and optimising the PDF parameters to achieve the best fit.

This procedure relies on the universality of PDFs, a fundamental property that allows PDFs extracted from one set of processes to be applied to predictions for other processes. This universality is a direct consequence of the factorisation theorems in QCD [95].

The factorisation approach has been successfully applied to a wide range of processes, from deep-inelastic scattering (DIS) to hadron-hadron collisions. In DIS, for instance, the factorisation formula takes the form:

$$\sigma_{DIS} = \sum_i \int dx, f_i(x, Q^2), \hat{\sigma}_i(x, Q^2) \tag{1.2}$$

where σ_{DIS} is the measurable cross-section, $f_i(x, Q^2)$ are the PDFs, and $\hat{\sigma}_i(x, Q^2)$ are the perturbatively calculable partonic cross-sections [106].

The success of this approach in describing a vast array of experimental data across many orders of magnitude in both x and Q^2 is evidence of the power of QCD and the concept of factorisation. However, challenges remain, particularly in the description of the proton's spin structure and in understanding the behaviour of PDFs at very small x values, where gluon saturation effects may become important [96].

The continued exploration of hadron structure keeps PDFs at the forefront of research

in particle physics. Their accurate determination is crucial for precision measurements at the LHC and future colliders, as well as for searches for physics beyond the Standard Model. The interplay between theory, experiment, and global analysis in the study of PDFs exemplifies the collaborative nature of modern particle physics research.

Experimental Input

The PDFs relies heavily on a diverse set of experimental measurements. These experiments probe different aspects of hadron structure across a wide range of kinematic regimes, providing the necessary constraints to extract PDFs with high precision. The extraction of Parton Distribution Functions (PDFs) relies on a diverse set of hadronic processes, each probing different aspects of nucleon structure. These processes can be broadly categorised into several groups, each offering unique insights into the partonic content of hadrons:

- **Deep Inelastic Scattering (DIS):** Fixed-target and collider DIS experiments form the backbone of PDF determination. Notable facilities include HERA for electron-proton collisions and fixed-target experiments at CERN SPS, SLAC, and Fermilab [96].
- **Semi-Inclusive Deep Inelastic Scattering (SIDIS):** SIDIS (and DIS) primarily probe the quark sector, with sensitivity to both valence and sea quarks. Experiments like COMPASS at CERN and HERMES at DESY have provided valuable information on flavour-separated quark distributions [106].
- **Drell-Yan (DY) Process:** Both fixed-target and collider experiments have measured this process, offering insights into sea quark distributions [98]. These processes are particularly sensitive to antiquark distributions. Collider measurements of W and Z boson production are particularly powerful in constraining flavour-separated quark and antiquark distributions [96].
- **Jet and Hadron Production:** These processes are crucial for constraining the gluon distribution. Key experiments include those at the Tevatron (D0, CDF) and the LHC (ATLAS, CMS, ALICE, and LHCb) [96]. These processes are crucial in constraining the gluon distribution, especially at high x and high Q^2 [98].
- **Top Quark Production:** Measurements of top pair and single top production provide additional constraints on the gluon and heavy quark distributions at high scales. Measurements from the LHC provide additional constraints on gluon and heavy-quark distributions at high scales.[107]

Note that while unpolarised PDF determinations benefit from a wide array of processes and high-precision data, polarised and nuclear PDF extractions often have more limited

data sets available. The complementarity of these processes, spanning different kinematic regions and sensitive to different parton flavours, is crucial for a comprehensive determination of PDFs. Global QCD analyses leverage this diverse set of measurements to constrain PDFs across the full range of x and Q^2, providing a coherent picture of nucleon structure that is essential for precise predictions at hadron colliders [108].

Current Determinations of Parton Distribution Functions

Parton Distribution Functions (PDFs) come in two main varieties: unpolarised and polarised. Unpolarised PDFs describe the momentum distribution of partons in a hadron without regard to their spin orientation, whereas polarised PDFs characterise the difference in parton distributions between different spin states of the hadron. This spin-dependent information is crucial for understanding the origin of hadron spin and the dynamics of quarks and gluons in polarised hadron collisions.

In the realm of unpolarised PDFs, recent global determinations include CT18, MMHT14, NNPDF3.1, JAM19, and ABMP16 [96]. These analyses differ in their methodological approaches, from data selection to parameterisation choices and error propagation techniques. Although there is significant overlap in the experimental data they include, each group makes unique choices that influence their final results. Most use variable flavour number schemes in their theoretical framework, with ABMP16 being a notable exception, opting for a fixed flavour number scheme. Recent updates in unpolarised PDF determinations have focused on incorporating new LHC data, particularly from top quark and jet production measurements. Some groups have also extended their analyses to include the determination of the photon PDF. The photon PDF accounts for the contribution of photons within the proton, arising from QED effects, to parton-parton interactions. This is especially relevant for processes involving initial-state photons, such as photon-gluon fusion or electroweak corrections to hadronic processes. Simultaneously determining the photon PDF alongside the strong coupling constant α_s further refines our understanding of hadron structure and the interplay between QCD and QED effects in high-energy collisions.

The study of polarised PDF determinations has seen significant progress with recent analyses, including LSS15, DSSV14, NNPDFpol1.1, and JAM17 [106]. These studies are predominantly performed at next-to-leading order (NLO) in QCD, reflecting the current state of theoretical calculations in polarised scattering. NLO calculations account for one-loop corrections to the leading-order predictions, improving the precision of theoretical results. A more detailed discussion of NLO and next-to-next-to-leading order (NNLO) accuracy in QCD calculations is provided in the context of heavy-flavour studies in Section 2.1.2.

Unpolarised and polarised PDF determinations show striking contrasts in their precision and data constraints. Unpolarised PDFs, benefiting from a wealth of experimental data, offer a more precise picture of hadron structure, particularly for valence quarks and gluons at medium x [96]. In contrast, polarised PDFs, constrained by a narrower dataset, present a more uncertain view across all parton flavours [106]. This disparity is most evident in sea-quark distributions. Although unpolarised sea quarks are reasonably well determined, their polarised counterparts show significant uncertainties and disagreements between analyses, especially for strange quarks. The gluon distribution tells a similar story: well-constrained in the unpolarised case, it has only recently revealed a sizable polarisation in the intermediate x range, thanks to RHIC data, while remaining largely uncertain at very low and high x [109]. Heavy-quark treatments also diverge, with unpolarised PDFs incorporating perturbative charm and bottom contributions, and even exploring intrinsic components. Polarised heavy-quark distributions, however, remain largely uncharted due to limited experimental constraints. These differences underscore the complementary nature of polarised and unpolarised PDF studies. While unpolarised PDFs provide a more complete picture of hadron structure, polarised PDFs offer unique insights into spin dynamics, each contributing to the evolving understanding of strong interactions in distinct ways.

The ongoing development of both unpolarised and polarised PDF determinations, driven by new data and refined theoretical and methodological approaches, highlights the dynamic nature of this field. The differences observed between various PDF sets emphasise the importance of using multiple sets in theoretical predictions. This practice allows for a more comprehensive assessment of PDF-related uncertainties in physical observables, a crucial consideration in precision physics at hadron colliders and in understanding hadron structure.

The theoretical foundations of both unpolarised and polarised PDF determinations, as well as their applications in high-energy physics, are rooted in the framework of perturbative QCD (pQCD). This framework provides the tools necessary for describing strong interactions at high energies and forms the basis for many of the theoretical predictions discussed above.

1.4 Aims of this Study

Heavy-flavour physics is a key area of study for probing perturbative aspects of Quantum Chromodynamics (QCD). In this work, heavy flavours refer to particles containing at least one heavy quark, specifically charm (c) or beauty/bottom (b) quarks. This study focuses on open heavy-flavour particles, which consist of a single heavy quark paired with a lighter quark (e.g., D mesons, B mesons, and Λ_c baryons), rather than quarkonia. Open

heavy flavour provides distinct advantages, as it is directly produced in hard scatterings during the early stages of a collision and serves as a clean probe of the QCD medium without the complexities of quarkonium suppression or regeneration [110].

Monte Carlo simulations, which form the backbone of this study, treat heavy quarks perturbatively because of their large masses ($m_c \approx 1.3$ GeV/c^2, $m_b \approx 4.2$ GeV/c^2) relative to the QCD scale, allowing a clear separation of short-distance hard scatterings from long-distance hadronisation processes. Heavy-flavour hadrons are identified primarily through their decay products, and this analysis focuses particularly on muons from heavy-flavour decays, as their long lifetime and penetrating nature allow for effective detection and precise measurements in forward regions of the detector.

The forward pseudorapidity region ($-4 \leq \eta \leq -2.5$) is particularly well suited for this study due to the unique capabilities of the ALICE detector, which is optimised for low-momentum particle identification in this range. Additionally, the forward region is sensitive to asymmetries in heavy-flavour production, providing complementary insights to midrapidity measurements.

One of the first objectives of this study is to investigate the differential yield of muons from heavy-flavour decays as a function of transverse momentum, dN/dp_T, in the forward pseudorapidity region, $-4 \leq \eta \leq -2.5$.

This research seeks to:

1. Analyse the impact of varying simulation parameters on single muon normalised yield ($1/N_{\mathrm{evt}} \times \mathrm{d}N/\mathrm{d}p_{\mathrm{T}}$) as a function of p_{T}, including:
   - Centre-of-mass energies (5.02 TeV and 13 TeV),
   - Parton Distribution Functions (PDFs): NNPDF2.3 (which is the default PDF in PYTHIA 8.3), and CTEQ6.6M (the default PDF in FONLL, a framework combining fixed-order pQCD calculations with next-to-leading-logarithmic resummation to predict heavy-flavour production cross-sections at hadron colliders [28]),
   - PYTHIA versions (6 and 8).
2. Contrast results from standalone PYTHIA simulations with those from integrated AliRoot-PYTHIA simulations, where AliRoot is the ALICE experiment's offline software framework for event generation, detector simulation, and data reconstruction (including GEANT detector simulations).
3. Compare the simulated inclusive single muon normalised p_{T}-yields of heavy-flavour

decay muons (e.g., charm and beauty) with the experimentally measured inclusive heavy-flavour decay muon normalised p_{T}-yield from ALICE Run 2 data (2015-2018). Background contributions from light hadron decays and other sources are accounted for or excluded as appropriate.

4. Compare the simulated inclusive differential heavy-flavour decay muon p_{T} cross-sections with ALICE Run 2 data (2015-2018) and FONLL pQCD calculations.

This comprehensive approach aims to provide insights into heavy-flavour production in pp collisions at $\sqrt{s} = 5.02$ and 13 TeV at the LHC. It particularly focuses on key processes such as gluon-gluon fusion, quark-antiquark annihilation, and flavour excitation, while validating simulation techniques against experimental data and exploring the interplay of various physical parameters in the production of muons from heavy-flavour hadron decays.

1.5 Thesis Outline

This thesis presents a comprehensive study of heavy-flavour production in high-energy pp collisions, structured in seven chapters that collectively build a cohesive narrative.

Chapter 1 establishes the theoretical and experimental context that motivates this research. It begins with an overview of the Standard Model and its fundamental particles, followed by a discussion of QCD. The chapter then focuses on heavy-flavour production, emphasising its significance in understanding the QGP.

Chapter 2 provides an overview of heavy flavours in pp collisions and a detailed examination of the ALICE detector, focusing on components crucial for heavy-flavour particle detection. Particular attention is paid to the Inner Tracking System (ITS) and the Forward Muon Spectrometer. The chapter also describes the ALICE Online and Offline systems, offering insight into data acquisition and processing during the experiment.

Chapter 3 introduces the Monte Carlo simulations using the PYTHIA framework, essential for studying pp collisions. This chapter discusses the transition from PYTHIA 6 to PYTHIA 8, detailing the simulation settings and particle data handling. It also addresses the strengths and limitations of these simulations, particularly in the context of the ALICE Offline Framework.

Chapter 4 presents the analysis methodology in detail. It outlines the strategy for standalone PYTHIA 8 simulations, including configuration settings, event generation, and muon selection procedures. This chapter also discusses the determination of differential single muon yields and the associated systematic uncertainties, highlighting the rigour of

the analysis process.

Chapter 5 compares the simulation results with experimental pp collision data from ALICE, from the period 2015-2018, during Run 2. This chapter presents a detailed comparison of inclusive single-muon differential cross-sections and heavy-flavour differential cross-sections. The analysis assesses the agreement between PYTHIA simulations, FONLL calculations, and experimental observations, discussing the implications for the current understanding of QCD and heavy-flavour production. Lastly, this chapter synthesises the key findings of the study, explores the implications of the results for theoretical models, and identifies potential areas for further investigation. This chapter also discusses the limitations of the current study, providing a balanced view of research results, summarises the main findings, and offers an outlook on future research directions. This chapter contextualises the study's contributions within the broader field of high-energy physics and the ongoing development of experimental and theoretical tools in the study of heavy-flavour production and QCD.

Through this structured approach, the thesis integrates theoretical foundations, experimental techniques, simulations, and rigorous analysis to present a comprehensive study of heavy-flavour production. Each chapter builds upon the previous ones, creating a narrative that is hopefully intellectually engaging and conveys the importance of our findings.

CHAPTER 2

Heavy-Flavour Studies and the ALICE Experiment

This chapter provides an overview of Heavy-Flavour physics in pp collisions and A Large Ion Collider Experiment (ALICE) at CERN (see Figure 2.1). ALICE is designed as a dedicated heavy-ion detector to investigate the properties of the QGP, by studying heavy-ion collisions, particularly lead-lead (Pb-Pb) collisions. ALICE also explores pp and proton-lead (p-Pb and Pb-p) collisions, which serve as both a comparison to Pb-Pb collisions and independent studies in their own right.

2.1 pp Collisions and Heavy Flavours

2.1.1 pp Collisions

The Large Hadron Collider (LHC) operates by accelerating two counter-rotating beams of protons to relativistic speeds and colliding them at designated interaction points. Each beam consists of numerous "bunches", with each bunch containing approximately 1.15×10^{11} protons [111]. The distance between consecutive bunches is 7.5 m, which, given the fast light speed of the protons, translates into a bunch spacing of 25 ns. This spacing is crucial for the LHC's operation and collision rate. In the 27 km circumference of the LHC, there are theoretically about 3550 possible bunch positions, although not all are filled during operation.

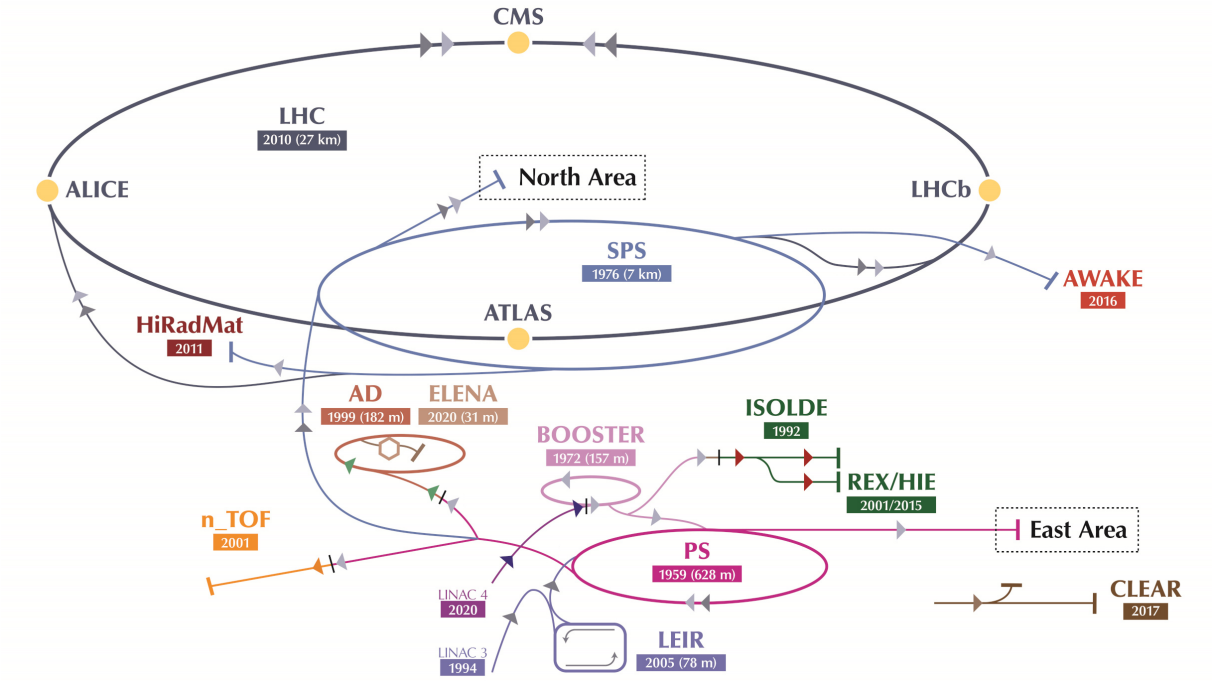


Figure 2.1: The CERN accelerator complex is a network of accelerators designed to accelerate particles to high energies (6.5 TeV for Run 2). The Large Hadron Collider (LHC) is instrumental in conducting four major experiments: ALICE (A Large Ion Collider Experiment) ATLAS (A Toroidal LHC ApparatuS; CMS (Compact Muon Solenoid); and LHCb (LHC Beauty), in addition to hosting a range of smaller-scale experiments which include TOTEM, LHCf, MoEDAL-MAPP, FASER, and SND@LHC.[3][4][5]

To maximise collision probability, these bunches are compressed to a cross-sectional area of approximately $16 \times 16\,\mu\text{m}^2$ at the interaction points, where the transverse beam size (σ) is determined by the beta function (β^*) according to $\sigma = \sqrt{\frac{\epsilon\beta^*}{\gamma}}$, with ϵ being the beam emittance and γ the Lorentz factor [112]. Despite this compression, the actual probability of two specific protons colliding remains incredibly low, approximately 4×10^{-21}, due to the minuscule size of the protons relative to the bunch dimensions.

The collision rate is a key parameter in LHC operations. It is quantified by luminosity (L), which measures the number of particle collisions that occur per unit area per unit time in an interaction region, with $L \propto 1/\beta^*$ for fixed beam parameters. With 11,245 bunch crossings per second and considering about 20 "effective" collisions per crossing, the LHC achieves approximately 600 million collisions per second. This high collision rate is crucial for studying rare phenomena and potential new physics. In 2015, the LHC aimed to operate with beams accelerated to 6.5 TeV and implement 25 ns bunch spacing. At the ATLAS and CMS interaction points, a β^* of 80 cm was used to achieve high-luminosity collisions by focusing the beams. In contrast, at the ALICE interaction point, a much larger β^* of approximately 10 metres was used for pp collisions. This larger β^* reduces

the luminosity and thus the number of multiple pp interactions, which is essential for ALICE's physics programme studying dense QCD environments, where precise event reconstruction requires clearly separated collision events. Detector pile-up makes it difficult to distinguish individual collisions, so this trade-off between luminosity and reconstruction precision is crucial for ALICE's measurements, unlike ATLAS and CMS, which prioritise high statistics for rare phenomena searches. At maximum luminosity, numerous primary vertices (collision points) are expected, which presents both opportunities and challenges for data analysis.

At the LHC, pp collisions can be broadly classified into two categories:

- Elastic Scattering: In these events, protons interact without breaking apart, essentially "bouncing" off each other while remaining intact [113]. The study of elastic scattering provides insight into the spatial distribution of partons within the proton.
- Inelastic Scattering: This more common type of collision at high energies involves partons from different protons interacting and fragmenting, leading to a cascade of new particles [102]. The products of these collisions typically include: Jets of hadrons formed from the hadronisation of quarks and gluons, leptons, photons, and occasionally exotic particles or evidence of new physics. Inelastic scattering events are crucial for probing fundamental aspects of quantum chromodynamics (QCD) [57].

In high-energy pp collisions, the interacting entities are the constituent partons (quarks, antiquarks, and gluons) rather than the protons as whole entities [94]. These parton interactions can be categorised as:

- Quark-quark interactions
- Quark-gluon interactions
- Gluon-gluon interactions

Each type of interaction contributes differently to observed phenomena. For instance, gluon-gluon interactions are primarily responsible for jet production and the creation of heavy particles [114].

The high-energy environment of the LHC provides unique conditions to investigate:

- The dynamics of parton interactions (quark-quark, quark-gluon, and gluon-gluon) at extreme energies
- The evolution of parton distribution functions (PDFs) [96]

Moreover, LHC collisions enable the exploration of less common proton constituents, such as intrinsic charm quarks [115]. Unlike sea quarks, intrinsic charm quarks are thought to be a bound component of the proton's non-perturbative structure, arising from Fock states like $|uudc\bar{c}\rangle$. Although not as prevalent as up- or down quarks, intrinsic charm can significantly impact collision outcomes, particularly in the production of charm-related particles at high momentum fractions or transverse momenta.

2.1.2 Heavy Flavours

Heavy-flavour physics is particularly valuable for probing both perturbative and non-perturbative aspects of QCD [116]. Heavy flavours are particles that contain at least one heavy quark, such as charm (c) or beauty/bottom (b) quarks. These particles differ from those composed solely of lighter quarks (up, down, and strange) and are generally classified into two categories: open heavy-flavour and quarkonia.

Open heavy-flavour particles consist of a heavy quark paired with a lighter quark. Examples include charmed mesons such as D^0 ($c\bar{u}$), D^+ ($c\bar{d}$), D_s ($c\bar{s}$) and charmed baryons such as Λ_c (cud), whose properties are presented in Table 2.1. The bottom quark counterparts include mesons such as B^0 ($d\bar{b}$) and B^+ ($u\bar{b}$).

Quarkonia are bound states consisting of a heavy quark and its corresponding antiquark, such as charmonium ($c\bar{c}$) and bottomonium ($b\bar{b}$). These states are particularly valuable for studying strong interactions because their large quark masses simplify theoretical calculations, making them less sensitive to non-perturbative QCD effects. In addition, their well-defined quantum states, such as J/ψ and Υ, provide relatively clean experimental signatures in high-energy collisions, making them easier to detect and study compared to states involving lighter quarks.

For heavy quarks, the mass (m_Q) is significantly larger than the non-perturbative scale; taking the $m_Q \to \infty$ limit is a good approximation. This introduces spin-flavour heavy-quark symmetry, significantly influencing the properties of hadrons containing a single heavy quark [117].

In pp collisions, heavy quarks are produced predominantly through perturbative QCD processes [118]. The main production mechanisms include:

- **Gluon Fusion:** At high energies, particularly at the LHC, gluon fusion becomes the dominant process for heavy-quark production [28]. In this process, two gluons from the colliding protons interact to produce a heavy quark-antiquark pair: $gg \to Q\bar{Q}$.
- **Flavour Creation:** This includes quark-antiquark annihilation ($q\bar{q} \to Q\bar{Q}$) in addition to gluon fusion. At lower energies, quark-antiquark annihilation can be

significant, but it becomes less important relative to gluon fusion as the collision energy increases [119].

- **Flavour Excitation:** A heavy quark from the sea-quark content of one proton is excited into the final state through interaction with a parton from the other proton.
- **Gluon Splitting:** A gluon splits into a heavy quark-antiquark pair, typically as part of the parton shower process.

The relative importance of these processes depends on the collision energy and the kinematic region of interest. At LHC energies, gluon fusion dominates the production of both charm and bottom quarks, especially at low transverse momentum and central rapidity [28]. The production cross-sections for charm and beauty quarks increase with the centre-of-mass energy ($\sqrt{s}$) in pp collisions, primarily due to the increasing gluon luminosity at small momentum fractions x.

Particle	Quark Content	Mass (MeV/c^2)	Decay Time τ ($\times 10^{-15}$ s)	Decay Length $c\tau$ (μm)
$D^{\pm}$	$c\bar{d}$	1869.65 ± 0.05	1040 ± 7	311.8
D^0	$c\bar{u}$	1864.83 ± 0.05	410.1 ± 1.5	122.9
D_s^+	$c\bar{s}$	1968.34 ± 0.07	500.8 ± 4.5	149.9
Λ_c^+	cud	2286.46 ± 0.14	200.0	60
$B^{\pm}$	$u\bar{b}$	5279.32 ± 0.14	1.638 ± 0.004	491.1
B^0	$d\bar{b}$	5279.63 ± 0.15	1.520 ± 0.004	455.7

Table 2.1: Properties of open heavy-flavour particles

The production of heavy quarks occurs primarily via quark-antiquark annihilation or gluon-gluon fusion. At high collision energies, gluons can form pre-resonance states during initial hard scattering processes. Gluons can dissipate energy through radiative and collisional loss mechanisms. Radiative energy loss, dominant at high p_{T}, involves partons losing energy through gluon radiation. At low p_{T}, the collisional energy loss is more significant [120].

Experiments at various colliders, including RHIC and the LHC, have made significant contributions to our understanding of heavy-flavour physics [121][122]. The ALICE experiment at the LHC has provided precise measurements of charm and beauty production in pp collisions [123]. These measurements, combined with theoretical calculations such as FONLL, have greatly improved the understanding of heavy-quark production [26]. Moreover, the study of the production of heavy flavours in pp collisions serves as a critical focus

area in the ALICE experiment's pursuit of understanding the properties of the QGP and the nature of strong interactions. The baseline pp measurements allow for analysis of the modification of heavy-flavour production cross-sections through energy loss in larger collision systems, as one of multiple approaches to deriving valuable insights into the properties of the QGP [124].

2.1.3 pQCD in Heavy-Flavour Studies

Perturbative Quantum Chromodynamics (pQCD) plays a crucial role in the study of heavy-flavour physics, particularly in understanding the production and properties of hadrons containing charm and bottom quarks. The relatively large masses of charm and bottom quarks, approximately 1.3 GeV/c^2 and 4.2 GeV/c^2, respectively, provide a hard scale that justifies the use of perturbative methods [28].

Heavy-quark production in hadronic collisions can be described using the factorisation theorem, which separates the process into short-distance (perturbative) and long-distance (non-perturbative) components.

$$\sigma_{AB\to HX} = \sum_{i,j} \int dx_1 dx_2 f_i^A(x_1, \mu_F^2) f_j^B(x_2, \mu_F^2) \hat{\sigma}_{ij\to Q\bar{Q}}(x_1, x_2, \mu_F^2, \mu_R^2) D_{Q\to H}(z, \mu_F^2) \quad (2.1)$$

Here, f_i^A and f_j^B are the parton distribution functions (PDFs) of the two colliding hadrons, A and B, $\hat{\sigma}_{ij\to Q\bar{Q}}$ is the partonic cross-section calculable in pQCD, and $D_{Q\to H}$ is the fragmentation function describing the hadronisation of the heavy quark [119].

The pQCD calculations for heavy quark production are typically performed to next-to-leading order (NLO) or even next-to-next-to-leading order (NNLO) accuracy. These calculations include contributions from gluon fusion ($gg \to Q\bar{Q}$), quark-antiquark annihilation ($q\bar{q} \to Q\bar{Q}$), and flavour excitation processes ($Qg \to Qg$) [125].

One of the key applications of pQCD in heavy-flavour physics is the calculation of differential cross-sections. For example, the p_{T} distribution of heavy hadrons can be computed as:

$$\frac{d\sigma}{dp_T} = \int dz \frac{d\hat{\sigma}}{d\hat{p}_T}(\hat{p}_T = p_T/z, \mu_R, \mu_F) D(z, \mu_F) \quad (2.2)$$

where z is the momentum fraction carried by the hadron, and μ_R and μ_F are the renormalisation and factorisation scales, respectively [28].

Although pQCD is highly successful at high energies, it breaks down at low energies

where α_s becomes large. In this regime, non-perturbative methods such as lattice QCD become necessary [87][98]. Experimental validation of pQCD predictions is crucial and is carried out at facilities such as the LHC. The ALICE experiment at CERN's LHC, while primarily designed for heavy-ion collisions, also contributes to pQCD studies through pp collision data [126].

The following sections focus solely on the detectors used in the measurements of muons from the decays of heavy-flavours.

2.2 The ALICE Detector

ALICE measures a wide range of particles, including hadrons, electrons, and photons, in its central barrel, while the purpose-built muon spectrometer enables the detection and analysis of muons. Particle identification and tracking to low transverse momentum close to zero (approximately 0.1 GeV/c) is a crucial capability of ALICE, allowing for the precise determination of particle types based on their characteristics, such as energy loss, time of flight, and momentum. ALICE performs various measurements and studies to deepen our understanding of collision dynamics and the properties of the produced particles. Particle multiplicity, which refers to the number of particles produced as a function of their transverse momentum and pseudorapidity, is one of the measurements conducted by ALICE. Particle correlations are also investigated to explore the relationships and patterns among particles, providing insights into the collective behaviour and interactions within the QGP.

The ALICE detector, illustrated in Figure 2.2, is located 56 metres underground at Point 2 near Saint-Genis-Pouilly, France. It is positioned between the ATLAS, located at Point 1, and the CMS experiments at Point 5. It is a massive structure measuring 16 metres in height, 16 metres in width, and 26 metres in length, with a total weight of 10,000 tonnes. The detector receives particle beams from the Large Hadron Collider (LHC) from both the ATLAS side (A side) and the CMS side (C side).

The ALICE Experiment explores heavy-flavour production via multiple decay channels and jet production, providing information about the energy loss mechanisms in the QGP. These are just a few examples of the measurements and studies carried out by ALICE. The detector's capabilities extend to various aspects of heavy-ion collisions, enabling a comprehensive exploration of the QGP and shedding light on fundamental questions about the properties of matter under extreme conditions. The study of heavy-flavour production in pp collisions provides a critical reference for understanding fundamental QCD processes. Studies of pp collisions serve as a baseline for more complex collision systems such as p-Pb and Pb-Pb. These measurements help to test theoretical models, such as perturba-

tive QCD, and establish benchmarks for observing medium-induced effects in heavy-ion collisions. By analysing heavy-flavour production in pp collisions, we can better interpret results from nuclear collisions and improve our understanding of the strong interaction under different conditions.

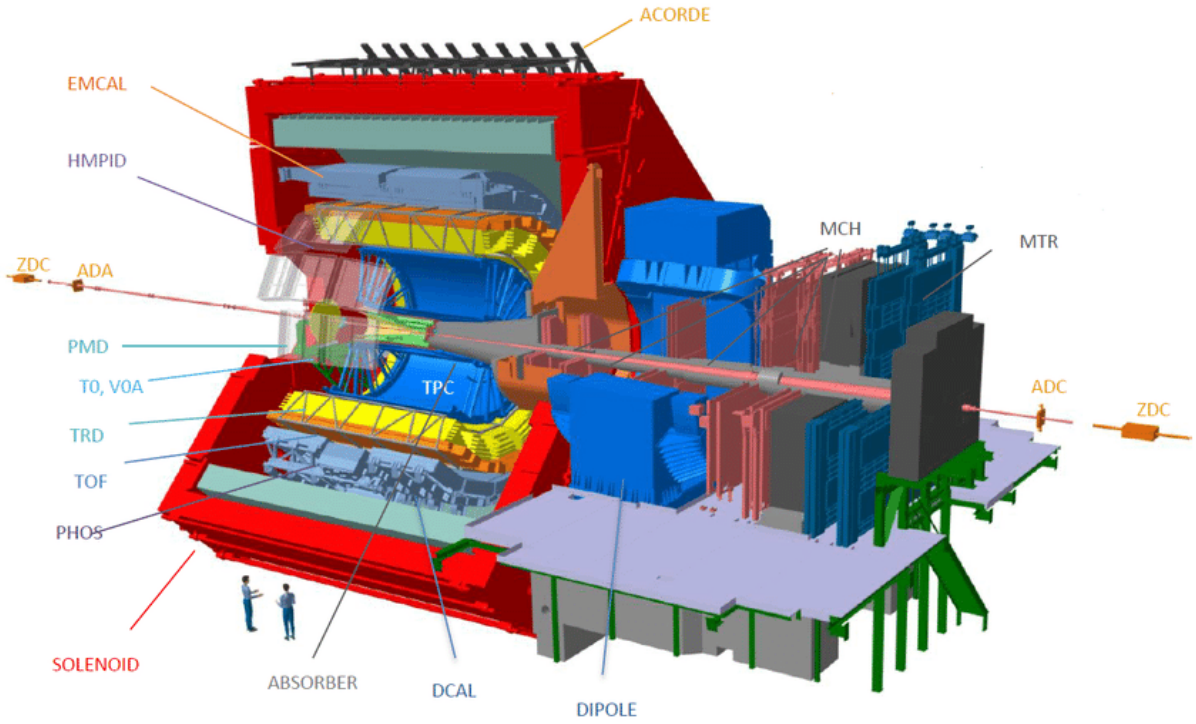


Figure 2.2: The ALICE detector in Run 2. This figure illustrates the central barrel and muon spectrometer, along with their various subdetectors. The ALICE detector locates events and particles inside the detector using Cartesian and cylindrical coordinates. The Interaction Point (IP), where collisions between accelerated particle beams from the LHC occur, serves as the origin of the Cartesian coordinate system and is located precisely in the middle of the ALICE detector's central barrel. Using Figure 2.1 as a reference, the x-axis runs directly from the origin to the LHC ring's centre. The y-axis extends straight from the origin towards the Earth's surface. The z-axis points from the IP and runs parallel to the LHC's beam path. The z-axis' positive side is designated the A-side and is in the direction of the ATLAS detector. The negative side is the C-side and is in the direction of the CMS detector. The Cartesian and cylindrical systems share a z-axis specification with its origin at the IP. However, these coordinates use the azimuthal angle (ϕ) (which is the angle measured in the xy plane) as well as the radial distance (r) - which is the distance travelled in a straight line from a point to the origin. The Central Barrel spans 360° (or 2π radians) in the ϕ direction and is symmetrically positioned around the IP. The Muon Spectrometer is located on the C-side.[6][7]

The ALICE detector comprises a central barrel and a forward muon spectrometer. In its central barrel, the ALICE detector incorporates the Inner Tracking System (ITS, $|\eta| < 0.9$), Time Projection Chamber (TPC, $|\eta| < 0.9$ for full track length), and Time-Of-Flight (TOF, $|\eta| < 0.9$) detector. These components track particles, determine their vertices, and identify them within the midrapidity range.

The Central Barrel includes several key detectors, each playing a vital role in the ALICE experiment:

- **High Momentum Particle Identification Detector (HMPID)** ($-0.6 < \eta < 0.6$): Provides particle identification (PID) at high momentum ranges.
- **Transition Radiation Detector (TRD)** ($-0.84 < \eta < 0.84$): Identifies electrons and measures their energy loss.
- **Electromagnetic Calorimeters (EMCal)** ($|\eta| \leq 0.7$, $\Delta\phi = 107°$): Measures energy deposition from electrons and photons.
- **Photon Spectrometer (PHOS)** ($|\eta| \leq 0.12$, $\Delta\phi = 100°$): Specialised for precise photon detection.

Surrounding the barrel is the **L3 solenoid magnet**, with a radius of 5.93 metres, a length of 11.90 metres, and a maximum magnetic field of 0.5 T, crucial for bending charged particle tracks. Additional complementary detectors include:

- **Zero Degree Calorimeters (ZDC)** ($\theta \approx 0°$, with electromagnetic calorimeters ZEM at $4.8 < \eta < 5.7$): Detect spectator nucleons for event centrality determination.
- **Forward Multiplicity Detector (FMD)** ($-3.4 < \eta < -1.7$ and $1.7 < \eta < 5.0$): Measures charged particle multiplicity in the forward region.
- **Photon Multiplicity Detector (PMD)** ($2.3 < \eta < 3.7$): Detects photon multiplicity.
- **ACORDE scintillators** ($-1.3 < \eta < 1.3$, $-60° < \phi < 60°$): Installed on the L3 magnet for cosmic ray detection.

These components are essential for characterising events and triggering responses, offering a detailed overview of collision processes. More information on ALICE's full range of detectors is available in the referenced literature.[8][127][128][129][130][131]

The ALICE Forward Muon Spectrometer, located outside the L3 magnet, operates within the pseudorapidity range of $-4.0 < \eta < -2.5$, focusing on the detection of muons origi-

nating from the decay of heavy-flavour hadrons such as D and B mesons, as well as W and Z bosons. It is particularly adept at measuring quarkonium states (including J/ψ, ψ(2S) and the Υ family) with a mass resolution sufficient to distinguish between the various bottomonium states. Additionally, it facilitates the study of low-mass vector mesons (ρ, ω, ϕ) through their decay into muon pairs (μ^+/μ^-). The muon spectrometer's configuration includes a series of components: a front absorber, shielding around the inner beam pipe; a passive muon filter to discriminate against background particles; a dipole magnet to bend muon trajectories for momentum measurement; and an arrangement of tracking and trigger chambers for accurate detection and measurement of muons.[132]

2.2.1 The Inner Tracking System (ITS)

A significant problem that needs to be solved by the ALICE detector is the accurate determination of particle trajectories, which is important for reconstructing collision events and identifying particles and the decays that took place. Many particles are produced in *pp* collisions, and these particles follow unique paths from the interaction point. In heavy-ion collisions, significantly more particles are produced, and the detector must be able to simultaneously track and identify these particles accurately. We expect a multiplicity of $dN_{ch}/d\eta = 8000$ per event for charged particles, which requires excellent precision and granularity.[8]

The ITS (illustrated in Figure 2.3) primarily aims to track charged particles in their earliest states after a collision occurs. It is ideally positioned as close as possible to the collision point, allowing it to determine the primary vertex, the spatial coordinates of the collision. The ITS is also responsible for determining the points where unstable particles initially decay, known as secondary vertices. It is crucial to separate particles produced directly in the collision from those resulting from subsequent decays to determine the underlying interactions and the production of particles in the initial hard processes to a high degree of accuracy. Furthermore, the ITS also plays a role in determining collision centrality, which measures the overlap between the two nuclei in heavy-ion collisions.[133]

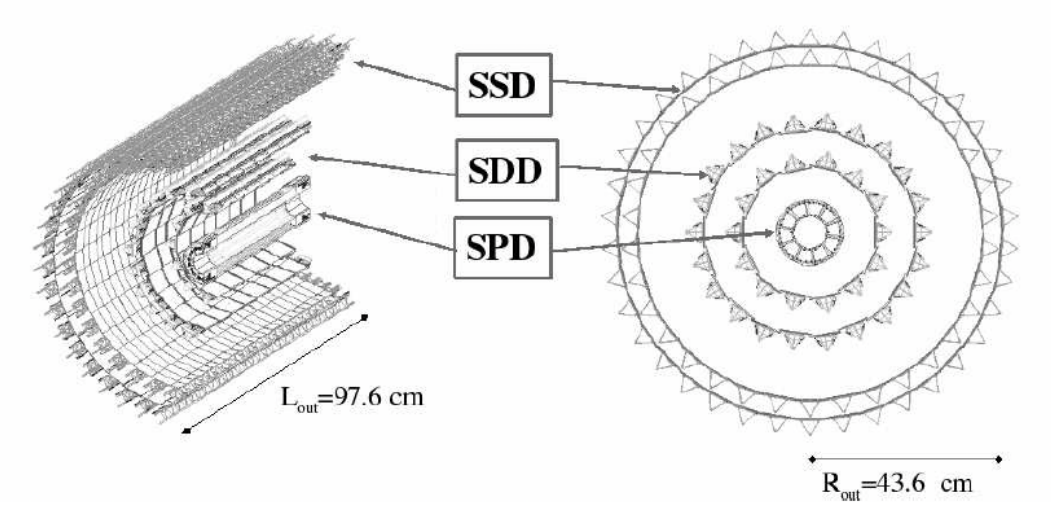


Figure 2.3: Schematic of the ALICE ITS.[8]

When charged particles are moving in a magnetic field, their motions follow curved trajectories. Determining the points at which the particles hit the detectors allows for reconstructing the trajectories as curved tracks. The transverse momentum of a particle (p_{T}) can be calculated from the curvature of its reconstructed track. Thus, the accuracy of the ITS tracking is paramount. The ITS must be highly accurate in determining the positions of particles close to the interaction point to avoid creating significant uncertainties in computed trajectories further away from the initial collision. A cylindrical layout consisting of multiple concentric layers of silicon detectors allows for efficient tracking of particle trajectories by determining their spatial coordinates as they pass through each layer.

Due to the 'high resolution of the ITS', a unique feature of the ALICE detector is its ability to track low-p_{T} (≈ 0.1 GeV/c) particles. In this context, resolution refers to the smallest differences in values that can be measured. High resolution is crucial for accurately identifying low-p_{T} particles because these particles have tracks with high curvatures that are difficult to track over long distances. Additional design requirements included the ability to withstand the extremely high radiation levels produced at the interaction point. The ITS was designed with silicon to minimise any effects on particle trajectories and energies as they interact with the detector.[8][133]

The Run 1 and 2 ITS consisted of three types of silicon detectors: The innermost detector was the Silicon Pixel Detector (SPD); the Silicon Drift Detector (SDD) formed the middle layer; and the outermost layer, the Silicon Strip Detector (SSD) was the furthest from the interaction point. Each detector consists of two layers of silicon detection elements, which provide a point of interaction (and tracking) along the trajectory of a particle.

Combining these points formed all six layers, allowing for the accurate reconstruction of particle trajectories. The three silicon detectors employed different detector designs that complemented each other regarding resolution and particle identification (PID) capabilities.

Silicon Pixel Detector (SPD)

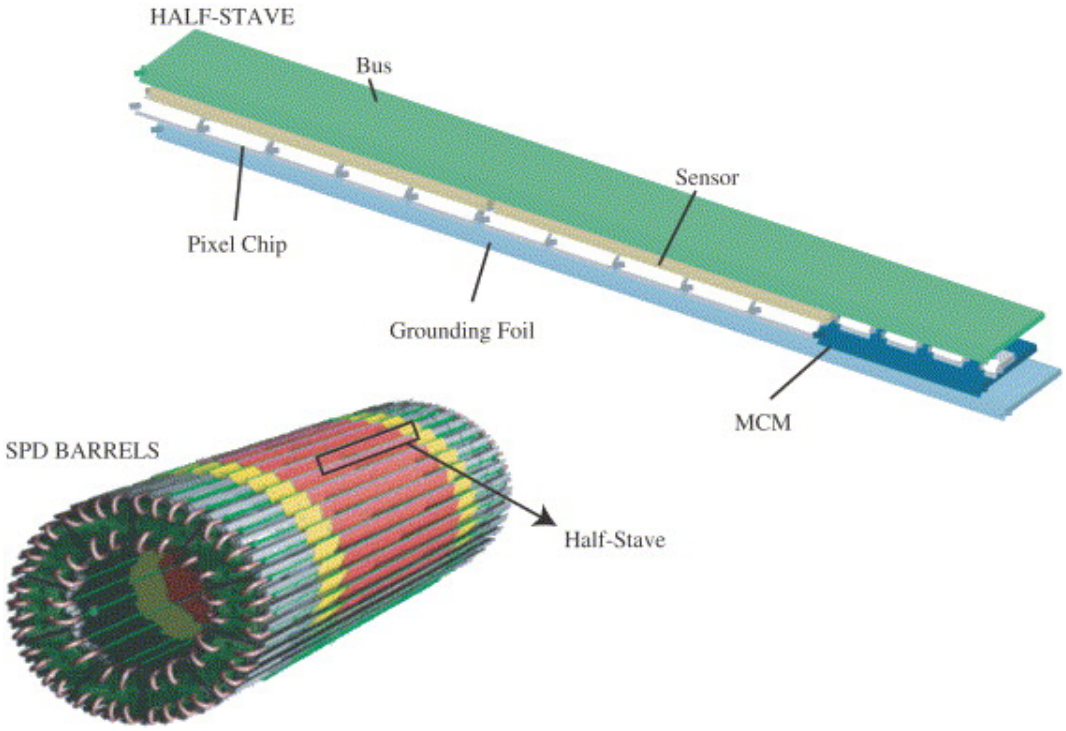


Figure 2.4: Schematic of the SPD barrels and a half-stave: The sensors (silicon pixels) in the SPD are responsible for detecting the charged particles. The Multi-Chip Module (MCM) processes the data collected by the pixels. The bus is a pathway that transmits signals from the pixels to the Multi-Chip Module. The grounding foil electrically isolates the half-stave, preventing any unwanted electrical interactions.[9]

The Silicon Pixel Detector, pictured in Figure 2.4, is placed closest to the interaction point, and provides the best spatial resolution and is optimised for primary vertex determination and measuring the impact parameter (the shortest distance from the primary vertex point to the trajectory of a produced particle). The SPD provides an almost instantaneous digital output when signals exceed a certain threshold and thus plays an important role in the L0 trigger system (which determines whether a particle event is interesting enough to record for further analysis).

The primary detector module of the SPD is the half-stave. A half-stave consists of two arrays (called "ladders") of silicon detector diodes that serve as pixels. The diodes are

reverse-biased, allowing current to flow only when a certain voltage threshold is exceeded. Each diode acts as an individual detector that produces a signal when a particle passes through it. Each pixel has dimensions of 50 μm x 425 μm, and the detector ensemble can capture and process the data from these pixels in 256 μs. Therefore, the SPD's readout is binary, and the signal from each pixel is categorised as either 'on' or 'off'. The pixels, therefore, create "images" of particle paths, allowing for precise tracking and particle identification.

Another critical component of a half-stave is the Multi-Chip Module (MCM), which contains multiple integrated circuits for processing the data collected by the ladders. The MCMs are connected to the ends of the half-staves and control the front-end electronics responsible for the initial data processing stage. The SPD consists of 10 lightweight carbon fibre sectors on the inner layer and eight half-staves on the outer layer mounted around the beam pipe to form a complete cylinder. Therefore, the SPD contains 120 half-staves, 240 ladders, 1200 pixel readouts, and 9.8 million cells.

The SPD is designed to be robust and sustain its performance in an environment with very high radiation levels. However, the amount of material (or material budget) that the SPD comprises has to be restricted to limit the impact of interactions of particles with the detector materials and ensure greater accuracy in measurements. The material budget constraint is determined by the quantity X_0, known as the radiation length. The radiation length, measured in units of $g.cm^{-2}$, represents the mass per unit area of material that reduces a particle's energy by $1/e$ due to bremsstrahlung. Each layer of the SPD has a material budget that is limited to 1% of X_0. The SPD barrel is also encased in a radiation shield that prevents heat from radiating towards the SDD, which is the next layer of the ITS.[8][9][134]

Silicon Drift Detector (SDD)

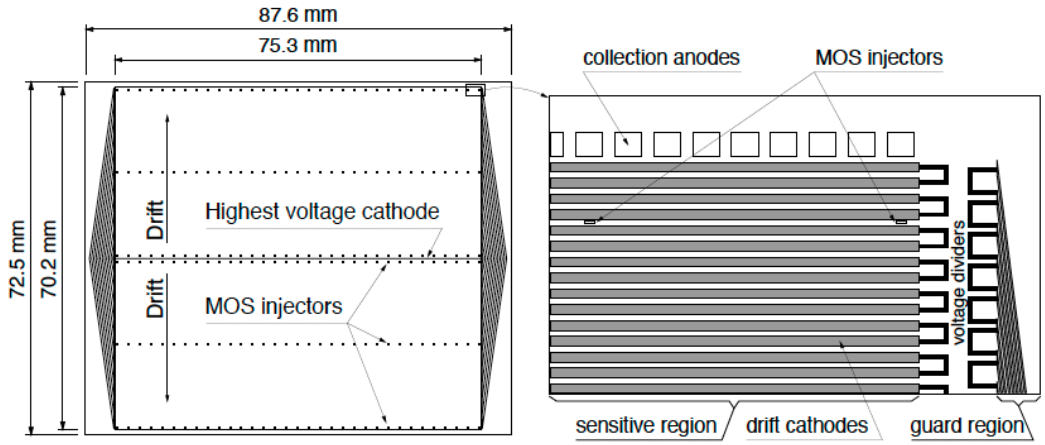


Figure 2.5: The ALICE SDD layout features two drift regions, each with 256 collection anodes, 33 charge injectors for drift velocity monitoring, and separate voltage dividers.[8]

The SDD comprises the third and fourth layers of the ITS and is optimised for two-dimensional position tracking and particle identification by specific energy loss (dE/dx). The value of dE/dx represents a particle's energy loss as it passes through the detector materials and is critical for identifying the particle's species.

Silicon Drift Detectors operate based on the principle of charge drift, which is the movement of charged particles in an applied electric field. When a charged particle from a collision event passes through the silicon of the SDD, it ionises the silicon atoms, creating electron-hole pairs. An electric field causes the electrons to drift towards a region of positive charge (a series of anodes). The electric field strength and the mobility of the electrons in silicon determine the drift velocity of the electrons. The drift time, or the time it takes the electrons to reach the anodes, is used to determine one of the coordinates of the particle hit point. The charge distribution among the anodes determines the second coordinate. In this way, the SDD can provide high-resolution two-dimensional position information for each particle event. Furthermore, the total charge collected at the anodes gives energy loss information, which helps identify the type of particle that caused the ionisation. SDDs were chosen because they provide very high-resolution detection in two dimensions, making them suitable for tracking when there is a high track density.

An individual SDD is split into two adjacent 35 mm long drift regions, each equipped with 256 charge collection anodes, separated by a central cathode that generates an electric field, causing free electrons generated by particle interactions to move in opposite directions in the two regions. A second power supply for each region ensures that the biasing of the collecting region (where the electrons accumulate) is maintained independently of

the drift voltage. This independent biasing is crucial as it ensures that the collection of charges is not affected by fluctuations in the drift voltage. In addition, voltage dividers in the guard region integrated into these drift regions maintain consistent electric fields across the detector. The location of the collection points allows the detector to determine where a particle interaction occurred. The granularity of the detector is determined by the number of anodes, their pitch, and size. An individual SDD has an active area of 7.02 x 7.53 cm and a pitch of 294 mm. Three rows of Metal-Oxide-Semiconductor (MOS) charge injectors are employed to track the velocity of drift electrons. Furthermore, tracking of drift electrons is highly sensitive to temperature. Therefore, MOSs enable continuous monitoring of the drift velocity and allow temperature-related adjustments as necessary.

There are two layers of 260 SDDs in total. The SDDs are mounted onto Carbon Fibre Reinforced Plastic (CFRP) ladders, providing structural support while maintaining a limited material budget. The inner SDD layer has a radius of 14.9 cm and a length of 59.5 cm, and consists of 14 ladders that each support six detectors. The outer layer comprises 22 ladders (each with eight detectors), and has a radius of 23.8 cm and a length of 67 cm.[8][135][8]

Silicon Strip Detector (SSD)

Silicon Strip Detectors play a vital role in matching tracks from the ITS to the Time Projection Chamber (TPC) and aiding in PID via dE/dx, especially for particles with low momentum.

The fundamental sensor module of the SSD is a 300μm thick silicon strip sensor with an active region measuring 75mm $\times$ 42mm. A sensor comprises 768 strips on either side, each with a 95μm pitch. A double-sided strip acts like a miniature diode with a negative side (n-side) and a positive side (p-side). As a charged particle moves through the detector, it causes ionisation of the silicon atoms, causing the free electrons to drift across the electric field across the n-side and p-side. This drift generates an electric current that measures the particle's position on both the p-side and n-side. The strips are laid down in angled positions, creating a "stereo pattern", allowing particles to cross multiple strips, resulting in more accurate measurements of position and trajectory and enhancing spatial resolution. The SSD's spatial resolution is primarily influenced by the pitch of the sensor readout strips and charge-sharing (the distribution of charge among adjacent strips).

Each strip detector has two hybrid circuits (that integrate semiconductor and passive components) that contain six front-end HAL25 chips that process the initial sensor signal. The six HAL25 chips amplify, shape and transmit signals via aluminium-polyimide cables to the EndCap Modules (ECMs), which buffer the signals. These buffered analogue signals are then sent to the Front-End ReadOut Modules (FEROMs) for analogue-to-

digital conversion. The modules are arranged in two concentric layers comprising 1m long carbon fibre ladders, with the fifth layer and sixth layer containing 34 ladders (with 22 modules) and 38 ladders (with 25 modules), respectively. This arrangement adds up to 72 ladders and 1692 modules for the SSD.

The system is optimised to have a low material budget to minimise multiple scattering and unwanted particle interactions within the detector material. The SSD material predominantly comprises sensors, contributing to an average material thickness encountered by traversing particles of 2.2% X_0.[8][136][137]

2.2.2 Central Barrel Forward Detectors

V0 Detector

The V0 detector is essential for efficient event triggering and detailed collision analysis at ALICE. In the context of ALICE, triggering refers to the mechanism that identifies which events are noteworthy enough to be captured for additional analysis in real-time. This system effectively discards less significant events by applying predefined criteria to focus on the most relevant occurrences. The V0 detector has excellent time and charge resolution, and its primary purpose extends beyond merely triggering events. It is crucial for distinguishing beam-beam interactions from various background events, including beam-gas interactions. The V0 system was designed to provide reliable triggering and centrality determination across the full range of collision multiplicities in both pp and A–A collisions. In pp collisions, the detection efficiency for at least one charged particle in both arrays reaches approximately 84% when secondary particles and environmental effects are included. The system employs various trigger modes including Minimum Bias (MB), Multiplicity Trigger (MT), semi-Central Trigger (CT1), and Central Trigger (CT2), with centrality classification based on the number of fired counters and total charge collected by the arrays. Furthermore, the V0 detector is a valuable tool for measuring beam luminosity and assessing charged particle multiplicity and azimuthal distributions.[8]

The V0 comprises two scintillator counter arrays, V0A and V0C. The arrays are positioned asymmetrically on either side of the interaction point. The V0A array is positioned approximately 340 cm from the interaction point, spanning the pseudorapidity range of $2.8 \leq \eta \leq 5.1$. Conversely, V0C is located closer, at about 90 cm in the negative z-direction, covering $-3.7 \leq \eta \leq -1.7$. The V0A and V0C arrays utilise a segmented design to enhance their particle detection capabilities. Each array is divided into four radial rings, and a further eight azimuthally divided sections. This segmentation improves the spatial and temporal measurement of collision events, providing crucial information for event selection and enhancing the performance of the dedicated tracking detectors. The V0 detector utilises BC404 plastic scintillators, known for their robustness and sensitivity.

The V0A array features scintillators with a thickness of 2.5 cm, while those in V0C are slightly thinner at 2 cm. These dimensions are tailored to optimise the detector's efficiency in capturing and processing collision-induced signals.[127]

The V0 detector employs a dual-trigger system. The first aspect of this dual-trigger system is centred on time-based triggers. These triggers are designed to synchronise with the signals emitted by the scintillator counters within the V0 detector. This synchronisation is crucial for accurately identifying events within specific time frames, enabling the detector to effectively distinguish genuine collision events from background noise or non-collisional interactions. This capability is vital for selecting minimum bias events and rejecting background events, a common occurrence in beam-induced interactions within the LHC. The V0 detector also employs a charge-based trigger system to complement the time-based triggers. This second trigger type analyses the total charge collected by the detector arrays. By measuring the accumulated charge, the V0 detector can categorise collision events in terms of their intensity and centrality (which is a measure of how colliding nuclei overlap). Such categorisation is critical for understanding the dynamics of particle production during collisions, as the nature and quantity of particles produced are directly influenced by the centrality of the interaction.

The effectiveness of the V0 detector in the ALICE experiment is further enhanced by its advanced readout electronics and data acquisition system. This architecture is designed to handle multiple operational modes, a necessity due to the diverse nature of collision events at the LHC. Central to this architecture is the Channel Interface Unit (CIU) board. The CIU integrates Photomultiplier Tubes (PMTs) signals, vital in detecting light from the scintillator counters. It also digitises the timing of these signals, converting them from analogue to digital format for streamlined processing. Additionally, the CIU is responsible for pre-processing data for the various trigger types and storing data during Level 0 (L0) and Level 2 (L2) triggers, each signifying different stages of the ALICE experiment's trigger protocol. The Channel Concentrator Interface Unit (CCIU) board complements the CIU, managing broader system functionalities crucial for the V0 detector's operation. The CCIU handles the clock signal distribution to ensure synchronisation across the detector's components. It also generates calibration triggers, which are vital for maintaining the accuracy and reliability of the detector. Furthermore, the CCIU organises data from the CIU boards and provides interfaces to connect to the Experiment Control System (ECS), ensuring efficient and coordinated data handling and processing.[127][138]

T0 Detector

The T0 detector plays a pivotal role in the precise timing of collision events at the ALICE experiment. This detector is essential for setting a starting time for the Time-of-Flight

(TOF) detector, which is crucial in particle identification. The T0 detector, comprises two arrays of Cherenkov counters. The T0A and T0C arrays are positioned on either side of the interaction point; T0C is 72.7cm from the IP, with a pseudorapidity coverage of $-3.28 \leq \eta \leq -2.97$, and the T0A array is placed approximately 375cm from the interaction point, with a pseudorapidity range of $4.61 \leq \eta \leq 4.92$.

The primary function of the T0 detector is to generate the Level 0 (L0) trigger signals, the earliest and most fundamental triggers in the ALICE experiment's data acquisition system. L0 triggers are crucial because they act as the initial gatekeepers, determining in real-time which collision events are recorded for detailed analysis. The L0 trigger decision is made based on information available within a very short time frame after the collision, typically within a few microseconds. The T0 detector is essential for ensuring that only events which meet predefined criteria are captured for further study. The T0 detector has fast timing discriminators and mean timers to achieve high precision and speed. Timing discriminators are electronic circuits designed to detect the presence of a signal above a certain threshold. These circuits are crucial in the T0 detector for identifying valid signals from the Cherenkov counters that indicate a particle collision has occurred. The mean timer, another critical component, calculates the average time of signals received from the T0C and T0A arrays. This average time is used to accurately determine the collision's timing, with a resolution as precise as 50 picoseconds. Such high precision is crucial for the Time-of-Flight (TOF) detector in ALICE, which relies on these timing signals to identify different types of particles produced in collisions.[127]

The electronics of the T0 detector are divided into front-end electronics (located near the arrays) and main T0 electronics (housed outside the L3 magnet). These components include the Clock and Pulse Distribution module (CPDM), TDC Readout Module (TRM), and Data Readout Module (DRM) cards. The CPDM distributes the 40MHz LHC clock to other components. The TRM card features a High-Performance Time-to-Digital Converter (HPTDC) which is crucial for the detector's timing resolution, distinguishing it from other devices. The DRM card interfaces with the ALICE DAQ system, encoding and transmitting data for further analysis.[8][127]

In addition to providing timing signals, the T0 detector assists in luminosity measurements, further enhancing its utility in the ALICE experiment. Its design, incorporating Cherenkov counters and fine-mesh photomultiplier tubes (PMTs), allows it to operate effectively in the L3's magnetic field, an essential requirement for its placement within the ALICE detector setup.

2.2.3 The Forward Muon Spectrometer

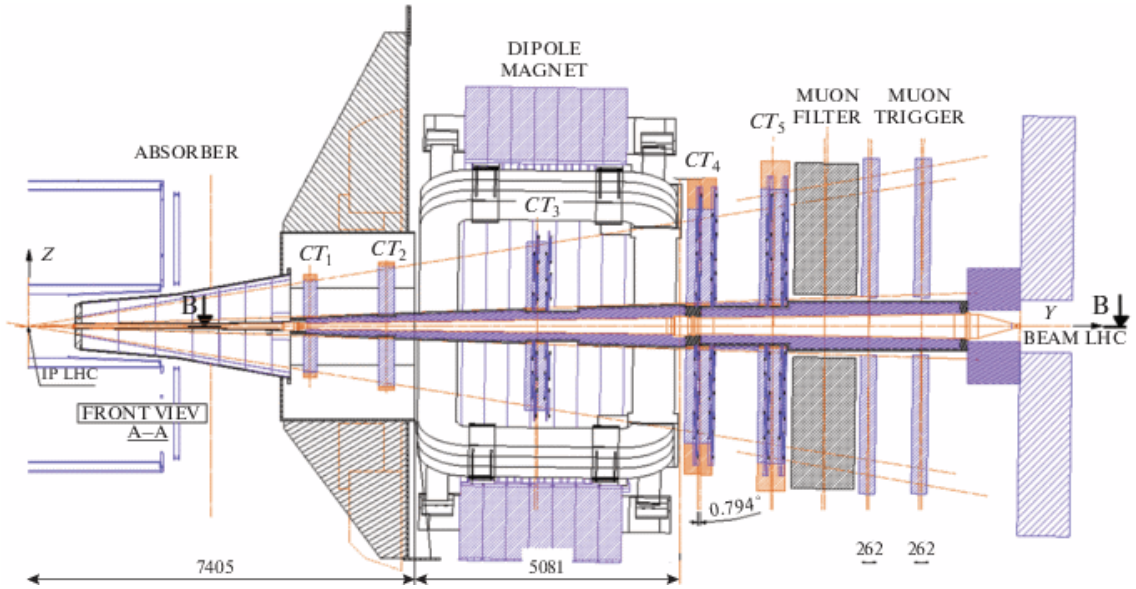


Figure 2.6: A schematic of the ALICE Muon Spectrometer.[10]

The muon spectrometer, pictured in Figure 2.6, is a specialised detector designed to detect and measure the spectrum of muons. The muon spectrometer primarily focuses on inclusive measurements of muon spectra, such as total yield or cross-section. Due to its design, it lacks the detailed tracking and vertexing capabilities necessary to trace the origins of the muons accurately. Consequently, while it effectively measures the quantity and energy distribution of muons, it struggles to differentiate between muons directly produced in collisions and those from the decay of particles like heavy-flavour hadrons or electroweak bosons. Therefore, to determine the trajectories of muons with high precision, utilising tracking data from the ITS, which is closer to the interaction point, is essential. Matching ITS tracks with tracks measured by the muon spectrometer helps to identify the tracks of muons produced in collisions. The measurements from the central barrel detectors thus complement the muon spectrometer's measurements, allowing for the study of heavy-flavours via the hadronic and leptonic decay channels. However, performing such precise measurements of muons can be challenging due to a significant background of hadron signals. This background complicates the measurement of muon pairs and the accurate measurement of transverse momentum to zero.

Minimising multiple scattering is another critical factor to consider for the muon spectrometer. Furthermore, a high event multiplicity poses a significant challenge. To address the multiple scattering and high multiplicity issues, the muon spectrometer required absorbers with strong hadron absorption ability and a dimuon trigger system that matches the trigger rate that the Data Acquisition (DAQ) system can handle. The muon spec-

trometer utilises the V0A and V0C detectors as a combined fast interaction trigger to increase robustness against the beam-gas background. Additionally, the spectrometer is equipped with two main trigger modes: the "low-" and "high-" p_{T} single muon triggers (0.5 GeV/c and 4.2 GeV/c respectively).[8][132][139]

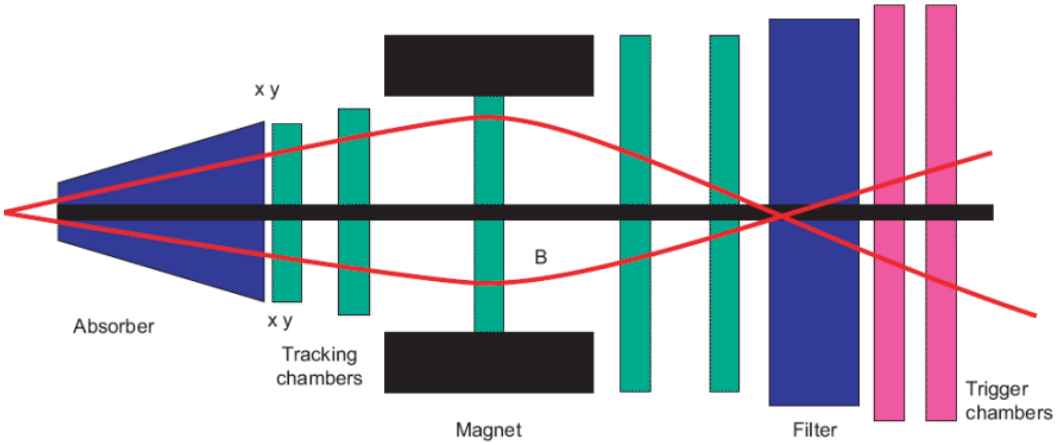


Figure 2.7: A schematic side view of the ALICE muon spectrometer demonstrating the paths of two muons.[11]

Muons are relatively heavy leptons and interact minimally with matter, allowing them to penetrate through several metres of material with minimal deflection and no absorption. This means that information about their origin is retained, allowing the muon spectrometer to be placed downstream of the collision point. The muon spectrometer's geometrical acceptance needs to be sufficiently large to ensure the accuracy of dimuon measurements. The main interactions are expected to occur in the mid-rapidity region, so the muon spectrometer's rapidity range needs to cover $-4 < \eta < -2.5$ as a compromise. This is equivalent to a polar angle range of $171° < \theta < 178°$.[132]

The muon spectrometer (Figure 2.6) comprises several sub-components, each with a specific function:

- An inner beam shield (15m long) that acts as a small angle absorber
- A passive front absorber positioned 90cm away from the interaction point (in the z direction), which helps to filter out unwanted particles
- A passive muon-filter wall made of 1.2m thick iron that is designed to stop most undesired particles but allows muons to pass through
- A tracking system that comprises five tracking stations that measure the trajectories of muons

- A trigger system comprised of two stations, which selects muons for further analysis
- A 5m long dipole magnet with a centre 9.9m from the interaction point that bends the paths of charged particles in a measurable and predictable way [8][140][139][132]

Absorbers

The front absorber is a conically shaped carbon, steel and concrete structure that reduces the primary hadron flux (pions and kaons) from collisions and shields the muon spectrometer's detectors from secondary low-energy particles (predominantly electrons). The front absorber is 4.13m long and is situated within the L3 magnet before the first tracking station and the dipole magnet of the muon spectrometer. It is located at a minimum of 90cm from the interaction point to accommodate the size of the ITS and avoid interfering with the central barrel detectors. The second function of the front absorber is to suppress the background of muons originating from the secondary decay of pions and kaons by constraining their free path while allowing muons with a momentum above a specific threshold to pass through. The front absorber's design required materials with lower atomic numbers and limited thickness to reduce straggling and multi-scattering.

The beam shield is an absorber tube constructed of tungsten, lead, and stainless steel that encases the beam pipe. The beam shield covers a θ angle of 2° to protect the tracking detectors from particles produced at extremely small angles and secondary particles resulting from interactions of the residual gas molecules inside the beam pipe (beam gas). The combination of the front absorber and the beam shield protects the tracking chambers and ensures the Muon Spectrometer's robustness against secondary particle production. However, an additional layer of absorbers is required to protect the trigger chambers. The muon filter is a 120cm thick iron wall positioned after the fifth tracking station and just before the first trigger station. It reduces the amount of low-energy background that would otherwise adversely affect the signal in the trigger stations. Together, the front absorber and muon filter only allows muons with momentum (p) higher than 4 GeV/c.[8][141][142]

The Tracking System

The tracking stations in the ALICE muon spectrometer are gas-based detectors, specifically Multi-Wire Proportional Chambers (MWPC) with Cathode Pad Chambers (CPC). These stations are strategically located at various distances from the interaction point: 5.4m, 6.9m, 9.8m, 12.9m, and 14.2m. The first two chambers are quadrant-type chambers, meaning that each chamber is divided into four distinct quadrants, which are essentially wedge-shaped sections that fit together to form a circular or semi-circular pattern around the beam pipe. The chambers are positioned in front of the dipole magnet, with the first station observing high particle densities up to 5×10^{-2} hits/cm^2. The third tracking sta-

tion, which sees a lower particle flux of less than 7×10^{-3} hits/cm^2, is inside the magnet at 9.8m from the interaction point. In contrast, stations 4 and 5, with their slat-type (rectangular) design, are situated immediately behind the magnet. Each tracking station, defined by a bending plane (zy-plane) and a non-bending plane (xz-plane), consists of two detection planes of CPCs. These are 5mm drift MWPCs equipped with bi-cathode pad readout. The chambers utilise a gas mixture of 80% Argon and 20% CO2 to ensure efficient ionisation and electron capture for accurate muon tracking. While the rectangular chambers in stations farther away offer excellent coverage over larger regions with fewer particles to detect, the quadrant-type chambers near the beamline provide complete angular coverage and efficiently control the high particle flux.

The sizes of the CPCs vary among the stations to account for the different particle flux densities (particularly at lower pseudorapidities). The pads are smallest near the beam pipe in station 1, measuring 5×6 mm^2, and increasing in size for stations 3, 4, and 5, up to 5×100 mm^2. The overall spatial resolution of these chambers is maintained at 80 - 85 μm, essential for precise particle tracking. The high-granularity readout structure in the first two stations is adapted to handle high particle densities, while the design in stations 3 to 5 addresses the challenges of maintaining large surface planarity (flatness) and rigidity under varying environmental conditions. The total detection area these five stations cover is approximately 100 m^2.

Regarding data processing, the tracking system collects raw data from the detectors and identifies clusters of hits indicative of muon interactions with the detector material. A specialised cluster-finder algorithm then correlates these clusters across different stations to reconstruct each muon's trajectory, enabling precise determination of the muons' momentum and path. The high granularity of the readout pads in the CPCs allows the tracking system to function effectively in environments with high particle multiplicities, a key capability for handling the dense particle fluxes typically encountered in collisions at the LHC. The tracking system's electronics are engineered to manage about 1.08 million channels. The signal from the CPC pads is captured by the front-end electronics (FEE) MANU (MAnas NUmerique) boards, integrating four 16-channel MANAS (Multiplexed ANAlogic Signal processor) chips for signal amplification and shaping. These boards also include two 12-bit ADCs (Analogue-to-Digital Converters) and a MARC (Muon Arm Readout Chip) for controlling the MANAS, handling zero suppression, buffering data, and interfacing with the DSP (Digital Signal Processor). DSPs then collect data processed by MANU cards and grouped into clusters by CROCUS (Cluster ReadOut Cluster Unit System) boards, located about 20 metres from the chambers, responsible for data aggregation and transmission to the data acquisition system through an optical Detector Data Link (DDL). The entire setup provides swift data transfer, completing within 240 microseconds post-trigger signal, thus underlining the system's design for operational

efficiency and accuracy in tracking muons.[139][8][143].

Trigger System

The Muon Spectrometer uses an absorption-based approach for detecting high (p_{T}) muons and is arranged in two gas detector trigger stations, each containing four planes. Inside each plane are 18 resistive plate chambers (RPC). Operating on the principle of gas ionisation, these RPCs use a precise mixture of Ar (49%), CH_2F_4 (7%), C_4H_{10} (40%), and SF_6 (4%), ensuring efficient operation and fast response, capable of handling high muon fluxes. The total active area these planes cover is substantial, extending over ($140m^2$).

The trigger system employs a multi-level processing scheme to analyse the detected muon tracks, involving three stages - local, regional, and global. Potential muon tracks are identified by their likelihood of originating from the primary vertex (which is determined at the local stage). The validation of a track only occurs if it is detected in at least three out of the four RPC planes, in both bending and non-bending planes. The bending plane is aligned with the direction of the dipole magnet's magnetic field, guiding charged particles, while the non-bending plane is perpendicular to this.

The RPCs' design features electrodes made from bakelite (a type of thermosetting plastic) with a resistivity range of 3-9 $\times 10^9$ Ω.cm, which is essential for their function. The electrodes are coated with linseed oil on the inside and graphite on the outside (with high voltage and ground connections on either side). Copper strips facilitate inductive signal reception in the detectors in both bending and non-bending plane directions. These readout strips are connected to front-end Amplitude-DUration LATency (ADULT) discriminators, which are tuned to the timing paramaters of the detector.

The local trigger electronics are tasked with producing a Level 0 single-muon trigger by applying a p_{T} threshold on the tracks. This involves processing the signals in the front-end electronics, where an analogue pulse is validated in the corresponding channel, and a corresponding logical signal is transmitted to the trigger electronics. The decision-making process at the local trigger level determines both the presence and charge (negative or positive) of a muon trigger. Subsequently, the regional and global trigger boards collect and analyse the data to select either dimuon or single-muon events based on the applied p_{T} threshold cuts, which are set at $0.5\,\mathrm{GeV}/c$ for low p_{T} and $4.2\,\mathrm{GeV}/c$ for high p_{T}. This precise selection is essential for minimising background noise in data analysis and isolating significant muon events.

Situated approximately 16 metres from the Interaction Point (IP), the MTR, comprising 72 RPC modules, is strategically placed to optimise muon detection. The operational design of the RPCs, including the two low-resistive electrodes separated by a $2mm$ gas-

filled gap, is tailored to meet the demanding conditions of the LHC. The aluminium pick-up strips outside the chamber are vital in signal capture. The complete setup of the MTR, from its physical design to its multi-level processing system, is fundamental in ALICE's study of high p_{T} muons.[132]

In the study of heavy-flavours (particularly in the semi-muonic decay channel), the interplay of various components of the ALICE detector system, including the V0 detector, plays a critical role in providing reliable minimum-bias triggers. Minimum Bias (MB) trigger employs a logical OR condition between signals from the V0A/T0A or V0C/T0C detector pairs and input from the Silicon Pixel Detector (SPD). The V0A and V0C play a crucial role in distinguishing genuine collision events from background noise, while the T0A and T0C provide rapid timing information, essential in activating other detectors in the system. The SPD's role is to pinpoint the collision vertex, adding another layer of precision to event selection. For analyses specifically targeting muons, the Muon Trigger stations introduce an additional level of filtering. These stations, building upon the MB trigger criteria, necessitate the presence of muon candidates surpassing certain momentum thresholds, set at 0.5 GeV/c for low-p_{T} triggers and 4.2 GeV/c for high-p_{T} triggers. This selective approach ensures that only muons relevant to ALICE's research objectives are included in the dataset.[8][127][144]

This chapter provided an in-depth exploration of the ALICE experiment, highlighting the critical components of the ALICE detector, particularly those essential for studying semi-muonic decays of heavy-flavours. These components include the central detectors, the muon spectrometer, and key forward detectors such as T0 and V0. The following chapter will focus on the offline ALICE system and outline the analysis methodology employed to obtain the results presented in this thesis.

2.3 The ALICE Offline Framework

2.3.1 AliRoot

The ALICE Offline Framework is an object-oriented software framework that is used for simulation, reconstruction, and analysis of data from the ALICE experiment. It is a framework specifically designed to handle the detailed simulation of physical collision events, track the passage (transport) of particles through various detectors, and reconstruct the events based on the interactions observed within the detectors. Detector response simulation is an essential function of AliRoot, which models how detectors react to passing particles and records these interactions in a way that mimics the actual detector outputs. AliRoot is based on CERN's ROOT software, and leverages its capabilities in Input/Output operations (I/O), geometry, Virtual Monte Carlo (VMC) methods, and visualisation.

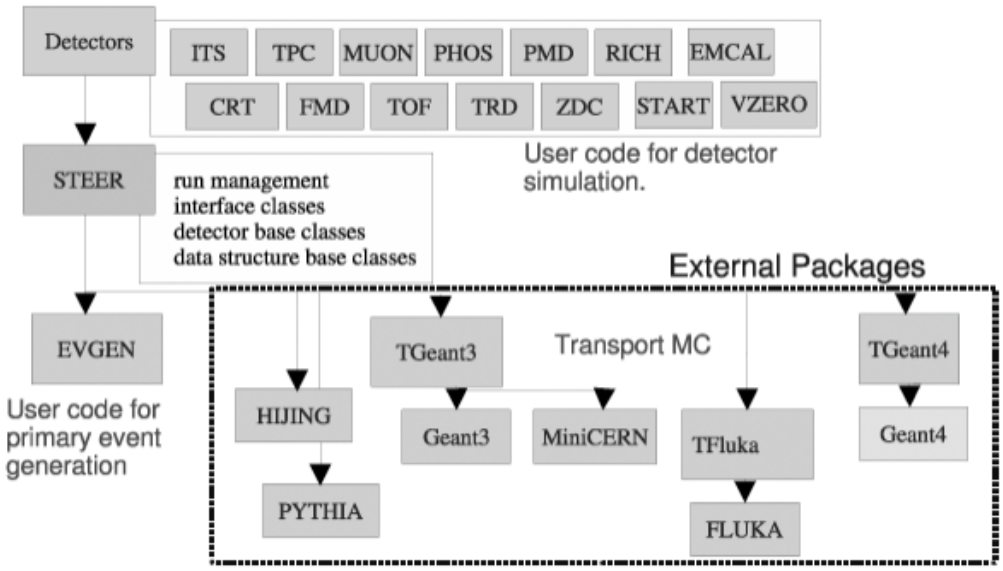


Figure 2.8: The organisation of AliRoot framework comprises of various base classes and interfaces for third-party external packages.[12]

ROOT's I/O system handles the efficient storage and retrieval of large volumes of data, which is essential when data sizes can be extremely large. The `TGeo` ROOT package is used by AliRoot for the description of the complex geometries of particle detectors. It helps in visualising and defining the spatial arrangement and material composition of the detectors. The Virtual Monte Carlo class, `TVirtualMC`, serves as a base for simulations, allowing for different Monte Carlo simulation packages to be used interchangeably.

AliRoot works in conjunction with AliPhysics, which is ALICE's software framework that contains the code necessary for actual physics analyses. This is where the detailed examination of data occurs, using the reconstructed information produced by AliRoot. AliPhysics contains the algorithms and tools uses to sift through the data, identify interesting events, and extract physical quantities. This can include measuring particle yields, momentum spectra, and other observables. AliPhysics contains Physics models that can predict how particles should behave, which can then be compared to how they behave in the experiment. Like AliRoot, AliPhysics is deeply integrated with the ROOT system, leveraging its statistical and data visualisation tools to perform the analysis tasks. AliRoot and AliPhysics are kept as separate modules to maintain a modular design. This means that while AliRoot deals with the general framework for simulations, AliPhysics is focused solely on physics analysis, making it easier to update and maintain the frameworks independently.[145][12][146]

At the heart of AliRoot's simulation capabilities are its base classes, which provide the

structure for primary particle simulation and fast simulation alternatives. These classes are extended by detector-specific modules written by the ALICE collaboration. The `STEER` module is at the core of the system and governs the execution (or steering) of processes and oversees particle stack implementations. These are essential for the VMC to function correctly. It offers the necessary interface classes for describing the detectors and organising their data structures. Furthermore, `STEER` forms the bridge between various other components, such as the event generator, specific detector modules, and links with the transport MC through `TVirtualMC`.

The user code is organised based on the different sub-detectors. Each detector is treated as an independent module, making sure there is no interdependency between them. Additionally, the system utilises data structures to record particle interactions within a detector, and to encapsulate this information into a format that would be used for event reconstruction and further analysis. The system also incorporates several external packages like PYTHIA and HIJING for event generation. For simulating particle transport through the detectors, there are `TVirtualMC` implementations of GEANT3, GEANT4 and FLUKA (`TGeant3`, `TGeant4`, and `TFluka` respectively). An important thing to note is that users can decide which packages to use during runtime, providing flexibility in the choice of tools.[12][145]

2.3.2 The Virtual Monte Carlo

The Virtual Monte Carlo (VMC) is a package that is part of the ROOT framework developed by CERN [147][148]. It provides a standard interface for different Monte Carlo generators and detector simulation tools, allowing them to be used consistently.

The VMC package provides abstract classes that define the standard interface for the different Monte Carlo generators and detector simulation tools. These classes define the methods needed to initialise, run and finalise the simulation and access the generated events and the detector response.

The specific implementation of these classes for a particular Monte Carlo generator or detector simulation tool is done in a plugin library. This plugin library implements the abstract classes for the specific generator or detector simulation tool. The VMC package also provides tools for steering the simulation, such as macros for generating events and running the simulation and a graphical user interface for visualising the generated events and the detector response.

2.3.3 Simulation

The AliRoot simulation framework uses a multi-stage process for generating and processing simulated data. Initially, the framework records hits, denoting points of interaction of a particle with a detector, capturing data such as position and energy deposition in detection elements. These hits are transformed into detector signals, termed summable digits, representing preliminary raw data.

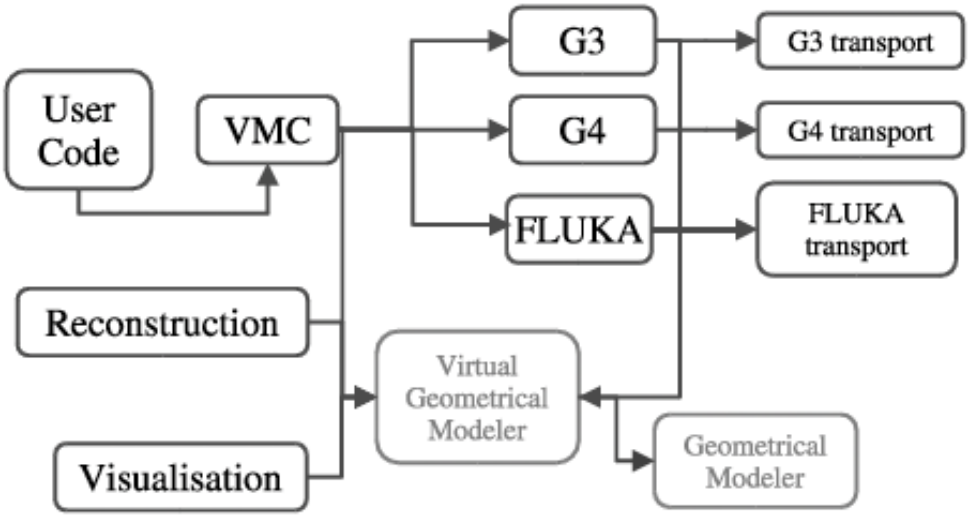


Figure 2.9: The organisation of AliRoot framework comprises of various base classes and interfaces for third-party external packages.[12]

To manage the complexity of these simulations, AliRoot implements the VMC as an insulation layer between to decouple user simulation code from a specific MC transport tool, providing flexibility and adaptability. This ensures that changes in transport MC packages do not require extensive rewrites of the user code, allowing for flexibility and future development.

The design of the ALICE detector consists of various distinct modules. A module is represented by a specialised class, inherited from the foundational `AliModule` class. The specific detectors are derived from the `AliDetector` subclass. These classes establish a consistent interface with the overarching simulation framework through a series of predetermined virtual methods. The `Config.C` configuration file is a key component of the setup process and orchestrates the setup of several critical elements before any simulation begins. These elements include the VMC, generator, objects, detectors, and the magnetic field map. The magnetic field map is a detailed representation of the L3 magnet's

magnetic field strength and direction throughout the central barrel volume. The VMC application initialises the geometries of the ALICE detector modules.

The VMC simulates the transport of particles step by step. Depending on the particle's position within a module, any hits within the detector are recorded and captures track references like location and momentum. These track references enable the comparison of reconstructed tracks against simulated particles. Hits are transformed into summable digits, and the summable digits are then transformed into a raw, digital format that resembles what the actual detector would produce during a real experiment.

2.3.4 Reconstruction

The `AliReconstruction` class is at the heart of the reconstruction process when dealing with raw data input, and oversees how raw data is transformed into meaningful information. This class initiates the reconstruction process by first reading the raw data generated by the simulation. The next crucial step is reconstruction for specific detectors, where each detector undergoes a specialised local reconstruction process for every event. The methods to determine the primary vertex and track particles can process data that is in raw format or from Monte Carlo simulation format. Each detector's initial local reconstruction process results in the formation of clusters. A cluster is a congregation of nearby digits (grouped by physical space or by time sequence) that likely originated from a single particle's interaction with a detector's sensitive component. Clusters, also referred to as reconstructed points, serve as a preliminary output in the reconstruction process. A vertex refers to a key interaction point, marking where particles have either interacted or originated. In the ALICE coordinate system, the primary-vertex reconstruction leverages data from the ITS.

The final output is captured in the Event Summary Data (ESD), which stores data on all the reconstructed particle trajectories and the fundamental attributes of the collision event. It serves to transform raw data into a format that is readily accessible and analyseable. The primary class governing this data structure is `AliESDEvent`, which aggregates essential identifiers such as the run and event numbers, the primary vertex, and an array of particle tracks, including a dedicated array for `MUON` tracks. The `MUON` tracks are a specialised subset of ESD tracks, representing the trajectories of muons in the muon spectrometer. A subsequent step in the data processing chain is to convert these ESDs into the more concise AOD format. This AOD format retains only the essential information needed for physics analyses, making the data more manageable and efficient to work with for researchers. For our purposes, the `AliAOD.Muons.root` file is used for studies focused on muons.

CHAPTER 3

Monte Carlo Simulations in PYTHIA

3.1 Monte Carlo Event Generators

Monte Carlo (MC) simulations are a fundamental tool in the study of heavy flavours in pp collisions at the ALICE experiment at the Large Hadron Collider (LHC). Understanding the production mechanisms and kinematic properties of heavy-flavour hadrons is crucial for advancing the understanding of Quantum Chromodynamics (QCD). Monte Carlo event generators, such as PYTHIA [149], simulate collision events based on theoretical models, allowing for a direct comparison between theoretical predictions and experimental data. These simulations play a central role in the validation of theoretical frameworks, the refinement of model parameters, and the extraction of detailed information on the production, propagation, and decay of heavy-flavour hadrons [150][8].

Monte Carlo event generators, such as PYTHIA [151] and HERWIG [152], play a crucial role in testing the predictions of pQCD. These generators use PDFs and fragmentation functions to simulate particle collisions based on Feynman diagrams of quark and gluon interactions. They allow for the computation of cross-sections and distributions of various physical observables in pp collisions [108].

Comparisons between experimental data and pQCD predictions are made using various methods, including measurements of inclusive cross-sections for different particle species and studies of azimuthal anisotropy. These comparisons not only test the validity of pQCD

but also help determine the values of the strong coupling constant and the distribution of partons at different energy scales [153].

Monte Carlo simulations are indispensable for studying various production mechanisms of heavy-flavour hadrons, such as gluon fragmentation, flavour excitation, and quark-antiquark pair production. By generating events representing different theoretical scenarios, simulations enable the quantification of the relative contributions of these processes, providing valuable insight into heavy-quark dynamics. For example, PYTHIA integrates perturbative QCD (pQCD) calculations for hard scattering processes while employing phenomenological models, such as the Lund string model [103], to simulate hadronisation. These simulations are critical for accounting for background contributions and detector effects [154][155], improving the accuracy of comparisons between experimental results and theoretical predictions [13]. An in-depth discussion of PYTHIA is presented in Chapter 3.

The simulation of pp collisions begins with initial conditions, including the energy, momentum, and parton distribution functions (PDFs) of colliding protons. The production of heavy-flavour hadrons is inherently complex due to the interplay of short-distance perturbative processes and long-distance non-perturbative effects. Monte Carlo simulations utilise the factorisation theorem to combine partonic cross-sections, calculated using pQCD, with non-perturbative elements such as PDFs and fragmentation functions. PDFs, such as NNPDF2.3 [101][156], provide information on the momentum distribution of partons inside protons, while fragmentation functions describe how heavy quarks hadronise into observable particles. These theoretical inputs enable predictions of kinematic properties such as transverse momentum, rapidity distributions, and multiplicities [149][26].

The ALICE experiment relies heavily on MC simulations to model particle interactions with the detector and reconstruct physics observables from raw data. Detector effects, such as geometric acceptance, resolution, and efficiency, are incorporated using tools such as GEANT3 [154][155]. These tools simulate how individual detector components respond to different particles, ensuring a realistic representation of experimental conditions. This is particularly important in heavy-flavour studies, where accurate modelling of charm and beauty production and their decay kinematics is essential for interpreting observed differential yields and cross-sections [123].

Monte Carlo methods enable systematic studies of theoretical and experimental uncertainties in heavy-flavour measurements. Varying the choice of PDF (e.g., NNPDF2.3 versus CTEQ6.6M [157]) and simulation parameters, such as the renormalisation and factorisation scales, provides insight into the robustness of the theoretical predictions. Additionally, PYTHIA simulations can be augmented with higher-order calculations, such as those from FONLL (Fixed Order Next-to-Leading Logarithms) [26], to improve prediction

accuracy for heavy-flavour production at LHC energies.

In the context of the ALICE experiment, the forward pseudorapidity region ($-4 \leq \eta \leq -2.5$) is of particular interest. This region is sensitive to asymmetries in heavy-flavour production and is uniquely probed by ALICE's forward muon spectrometer. By simulating muons from heavy-flavour hadron decays, MC event generators allow reconstruction and analysis of differential yields of these particles. These simulations provide a baseline for understanding production mechanisms and serve as an essential tool for interpreting experimental data collected at the LHC.

Monte Carlo simulations remain indispensable for heavy-flavour studies, enabling researchers to model pp collision outcomes, predict final-state particle properties, and validate theoretical frameworks. By bridging theoretical predictions and experimental data, they play a critical role in advancing our understanding of QCD and heavy-quark dynamics in high-energy collisions.

3.2 Overview of PYTHIA

PYTHIA is a Monte Carlo event generator software package developed and maintained by the PYTHIA group at Lund University in Sweden. It is primarily used to simulate high-energy physics collisions, using various models that simulate the interactions between particles using QCD and electroweak theories.[13] PYTHIA is an open-source software package currently written in C++, with the transition from FORTRAN occurring at version 8. The software is regularly updated to include the latest physics models and experimental data, ensuring it remains a robust and reliable tool for simulating high-energy physics interactions. One of PYTHIA's essential features is its ability to simulate various physical processes, including hard scattering, particle decays, and initial and final state radiation [150].

The PYTHIA framework relies on theoretical and phenomenological models grounded in experimental data. PYTHIA is used in many applications, including the simulation of particle collisions at the LHC, the study of cosmic rays, and providing input events for detector response simulations in experiments such as ALICE.

The concept of event generation is central to how PYTHIA simulates particle collisions. In this context, an event refers to one complete simulated collision process, from the initial colliding particles to the final set of all outgoing particles produced. An event begins with the collision of two incoming particles and encompasses all subsequent interactions, radiation, and particle production that result from that collision. Therefore, a single simulated event can be defined as a complete record containing the two incoming particles,

all intermediate processes, and all final outgoing particles along with their respective properties. Using conservation laws, the energy, momentum, and quantum numbers of the system's initial state (pre-collision) must equal the sums of the respective quantities of all the outgoing particles in the event [150].

The outcomes of events are different because of the probabilistic nature of quantum processes. As a result of the randomness of these processes, we can only obtain probability distributions of the properties we wish to study. Ultimately, the output of an event generated by PYTHIA is a list of particles with measurements of the probabilities of those events occurring, along with a history of the intermediate particles and processes of the event. Thus, PYTHIA acts as an event generator, producing event simulations in random sequences to predict all the properties that we can observe in high-energy particle collisions. However, PYTHIA cannot account for the full spectrum of physics phenomena and processes that occur and is limited to a finite set of parameters. The collection of parameters and their respective values used in PYTHIA is called a tune, and the values are determined using experimental data.[13]

3.2.1 PYTHIA 6 and PYTHIA 8

The current major version of PYTHIA is version 8.3. It is the culmination of decades of work that started in the 1970s at Lund University with the development of a programme called JETSET. JETSET modelled the hadronisation associated with jets form when "colour-anticolour" pairs are pulled apart. PYTHIA was subsequently built as an extension of JETSET, incorporating new processes related to pp collisions. Over time, PYTHIA was extended beyond QCD to include other processes from the Stand Model. PYTHIA 6 was written in the Fortran programming language, but during 2004-2008, PYTHIA underwent a significant overhaul. PYTHIA was rewritten in the C++ language as version 8 after the development of PYTHIA 7 was stalled.[13]

There exist several key differences between the two PYTHIA versions:

- PYTHIA 8 includes some physics models that are not available in PYTHIA 6. This update includes models for the simulation of collisions of heavy-ions such as lead (Pb) or gold (Au) nuclei. It also incorporates the ability to model multiparton interactions, which account for scenarios where multiple pairs of partons within hadrons interact simultaneously. Additionally, PYTHIA 8 can simulate parton showers, which are chains of events where partons emit additional partons, leading to a branching effect as they move apart after a collision.
- PYTHIA 8 is generally considered faster and more efficient than PYTHIA 6. The speed improvement is due to several improvements in the code, such as the use of

modern C++ features and the use of parallel processing.

- PYTHIA 8 has a new interface compared to PYTHIA 6, which makes it easier to use and more user-friendly. The new interface allows for more flexibility in the configuration of the event generation and makes it easier to switch between different physics models.
- PYTHIA 8 is actively maintained and developed, while PYTHIA 6 is no longer actively developed, but is still supported by the community.
- PYTHIA 8 can handle complex processes and physics models not implemented in PYTHIA 6. It also includes more recent physics models and experimental data, which may be necessary for some research.

3.2.2 Data Analysis

PYTHIA can simulate pp collisions in several ways in addition to as a standalone programme. PYTHIA 8 can be used as a library linked to other programmes, such as detector simulation or data analysis programs, allowing the user to generate events within a larger simulation framework or data analysis pipeline. PYTHIA 8 can also be used with other event generators to simulate pp collisions. It can be used with other generators, such as PYTHIA 6 or HERWIG, to simulate different aspects of the collision process. PYTHIA 8 can be used with other simulation frameworks, such as GEANT, which simulates the passage of particles through matter. PYTHIA can be used in high-performance computing (HPC) environments to generate large samples of events in parallel. This allows the user to quickly generate large samples of events, which is essential for certain types of data analysis. This allows the user to simulate a detector's interactions with the particles generated in collision events. Finally, PYTHIA can be used as a part of more complex simulation frameworks such as the AliROOT simulation framework.[149]

3.2.3 Limitations of PYTHIA

PYTHIA is a powerful tool for simulating pp collisions, but it does have some limitations. This can introduce uncertainties and biases in the generated events and may not accurately reflect the actual dynamics of the collision. PYTHIA 8 uses several approximations and simplifications to model the collision process. It is also based on the perturbative Quantum Chromodynamics (QCD) model, which serves as a generally reliable approximation for high-energy pp collisions, generally above 100 GeV. However, it may not be valid for lower energy (below 100 GeV) or other collisions. PYTHIA 8 primarily generates physics events. It does not simulate the detailed response of a detector to the generated events. The events generated by PYTHIA must be passed to another simulation framework (such

as GEANT[158][159][155]) to simulate the detector response. Its model parameters are not always well constrained by experimental data. This can lead to significant uncertainties in the predictions made by the generator. PYTHIA 8 is a complex programme with many settings and parameters that must be configured correctly to obtain accurate results. This can make it difficult for new users to set up and run the generator.

3.3 Programme Flow

PYTHIA generates events simulating the complex evolution of a high-energy collision through distinct stages, encompassing various aspects of particle physics. The primary stages of an event, along with their corresponding physical phenomena, can be elaborated as follows:

- Two initial particle beams converge, each defined by their respective parton distribution functions (PDFs).
- As the beams draw nearer, the partons within them undergo branching processes (e.g., $g \rightarrow qg$), giving rise to initial state parton showers. These showers represent the emission of gluons from quarks or other gluons as they lose energy and change direction.
- One parton from each beam engages in the hard scattering process, characterised by a high momentum transfer (≥ 2 GeV/c in QCD), producing outgoing partons.
- During the hard scattering process, gauge bosons may be created, which can subsequently decay into partons. Gauge bosons, such as W and Z bosons, are force carriers that mediate the electroweak interactions.
- The outgoing partons experience branching processes akin to the incoming partons, culminating in forming final-state parton showers. These final-state showers signify the additional emissions of gluons as the partons lose energy and change direction before hadronisation.
- Partons from the incoming hadrons may engage in multiple parton interactions. These interactions represent lower-energy exchanges between the partons of the colliding hadrons that contribute to the overall event structure.
- In hard scattering processes, where gluons and quarks are ejected, the principle of colour confinement necessitates that these partons cannot remain isolated. This phenomenon, known as hadronisation, involves the transformation of coloured partons into colourless hadrons, such as mesons (composed of a quark and an antiquark) and baryons (consisting of three quarks).

- Some of the produced hadrons are unstable and subsequently decay into other particles, further contributing to the event's final state.

By integrating these stages and their associated physics topics, PYTHIA 8 can effectively model the intricate dynamics of high-energy particle collisions, yielding valuable insights into the fundamental particle interactions and processes at play.

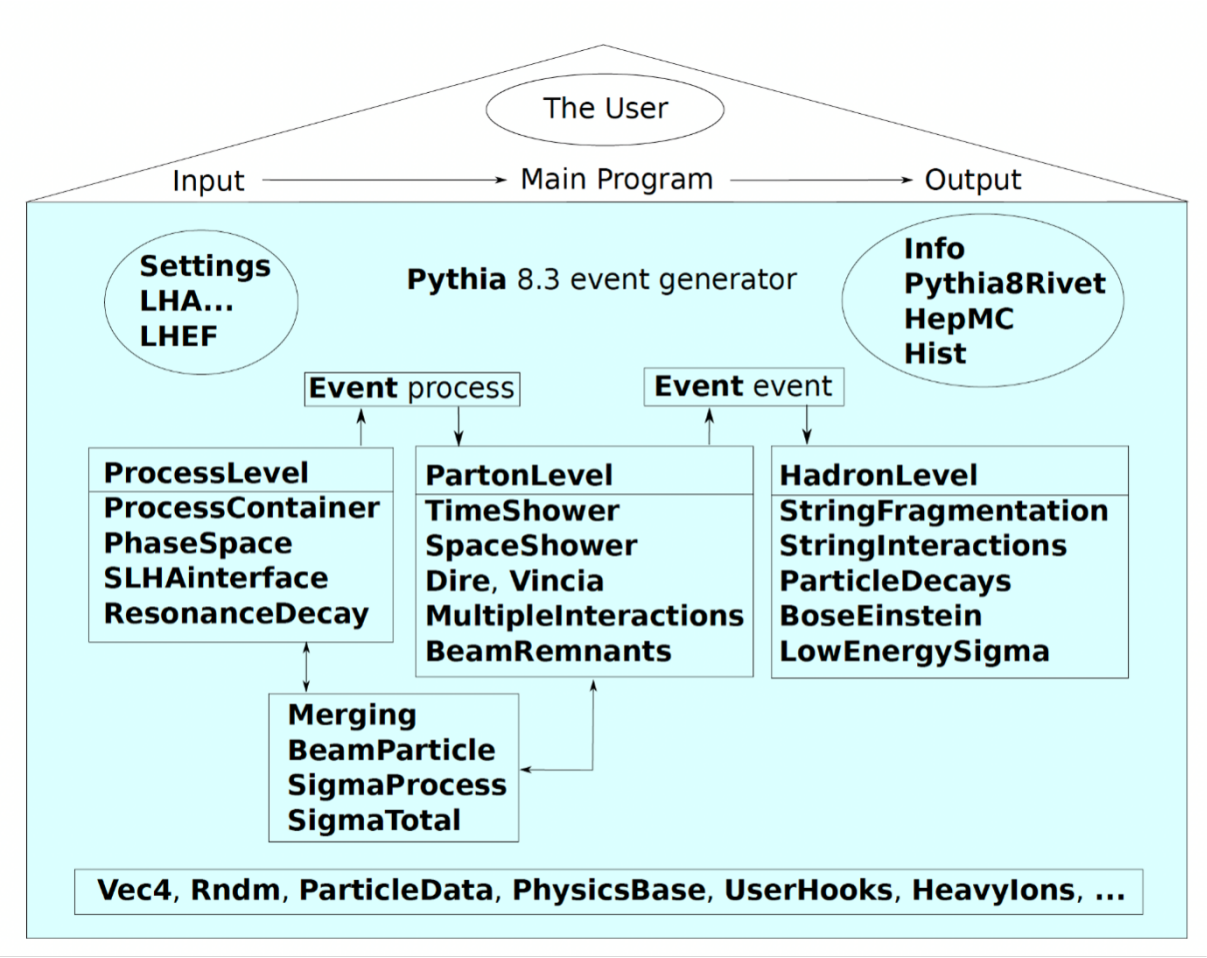


Figure 3.1: Pythia 8.3 programme structure with its main C++ classes.[13]

The **`Pythia8::Pythia`** class is the main class that manages the overall programme flow of the event generation. From a sequential perspective, the execution of a PYTHIA script consists of three phases: initialisation, generation, and finishing. During the initialisation phase, PYTHIA configures the requisite components for the simulation, such as the specific hard process to be simulated and the beam particles and their energies. This phase also involves configuring the parameters for the PDFs, settings and parameters for the event generation (such as the choice of the underlying physics models, showering algorithms, and hadronisation models).

PYTHIA 8 manages initialisation and programme flow using different classes, methods

and functions. When an instance of the **Pythia8::Pythia** class is created, it initialises the internal data structures and sets the default values for the simulation settings. The user can then set the desired values for the settings by calling the appropriate methods or reading them from an external file. The **Pythia** class also provides a method to initialise the event generation process. This method sets up the initial state of the event, such as the energy and momentum of the incoming protons. It configures the different sub-systems of the event generator, such as the parton shower and hadronisation.

Generation is the main phase of the simulation, where PYTHIA generates a series of events based on the specified hard process and input parameters. Once the initialisation process is complete, calling the **Pythia8::Pythia** class's **next()** method begins the event generation process. This process performs the main event generation steps, such as the parton shower, hadronisation, and decay of the produced particles. The **next()** method will generate one event at a time until the user decides to stop the event generation. The user can also use the **Pythia8::Pythia** class event method to access the generated events. PYTHIA simulates the hard scattering process for each event, followed by initial and final state radiation (ISR and FSR), multiple parton interactions (MPI), beam remnants, and colour reconnection. After the parton-level simulation, PYTHIA moves on to the hadronisation process, where partons are transformed into colour-neutral hadrons. Finally, the decays of unstable hadrons and any additional final-state interactions are simulated, producing a set of simulated events that can be analysed further or compared to experimental data .

The event generation phase comprises three steps (also called levels); the process level, parton level and hadron level. The first step is called the process level and handles hard-scattering processes, which are described using perturbative methods. These processes are the core high-energy interactions in a collision and usually involve a limited number of particles with very high energy.

The parton level handles initial state radiation (ISR) and final state radiation (FSR). This level describes the secondary interactions and processes before and after hard-scattering. This stage also includes simultaneous multiparton interactions and partons from the initial hadrons that were not directly involved in any processes or interactions (beam remnants).

The hadron level is the last stage of the particle collision and is focused on transforming coloured partons from the previous stage into colourless hadrons. This level also includes the decays of unstable hadrons, and its final output represents the outcome of a realistic and idealised collision [150].

In the finishing phase, PYTHIA terminates the simulation by calculating various event statistics, such as the total cross-section, the number of accepted and generated events,

and any pre-defined histograms or observables. This phase helps users summarise the simulation results and analyse the data to better understand the underlying physics processes.

3.4 The Event Record

The PYTHIA event record is a data structure that stores information about the particle content and properties of an event generated by PYTHIA. It stores the final state particles from a collision and information about the hard process, such as the matrix elements and parton showers. The event record is implemented as a container class that stores a list of particle objects, each representing a particle in the event. Each particle object contains information about the particle's properties, such as its 4-momentum, spin, and lifetime, as well as its origin, such as whether it is a final state particle or a parton in the parton shower. The event record also contains other information, such as the beam particles, and the scale and cross-section of the hard process.

The event record is used in different stages of PYTHIA's event generation process. First, the hard process is generated, and the event record stores information about the matrix element, the incoming and outgoing partons, and the scale of the process. Next, the parton shower is generated, and the event record stores information about the partons produced in the shower and their properties. Finally, the hadronisation process is performed, and the event record stores information about the final state hadrons, including their properties and the properties of their parents [13].

The Event class is a central component of the Pythia event generator framework, responsible for managing and storing the information related to a single event in a simulation. The Event class serves as a container for all the particles produced during the event, and it keeps track of their properties, interactions, and relationships. An instance of Pythia contains two members, process and event. The process member stores details of all the hard processes. The second member, event, stores the entire event history.

3.5 Particle Data

Particle data is represented by the class **`ParticleData`**. This class stores information about each particle, such as its mass, spin, charge, and decay properties. The particle database is initialised with default values based on PDG's data. This information is stored in a particle data table, a collection of **`ParticleData`** objects.

Pythia's event generation process relies heavily on this information to accurately simulate particle collisions, decays, and other phenomena. By leveraging the high-quality

data provided by PDG, Pythia ensures that its simulations are consistent with current experimental results and theoretical predictions in particle physics. Users can access and modify the particle properties in Pythia through the **`ParticleData`** class, tailoring the event generation to their specific research needs.

PYTHIA 8's particle data scheme stores various properties for each particle and uses this information to simulate the production and decay of particles at the multiple stages of high-energy collisions. The properties stored in **`ParticleData`** class allow PYTHIA 8 to generate events consistent with the experimental data and to extract information about the particles produced in the collisions. PYTHIA 8 uses the **`Event`** class to store the final state particles. The **`Particle`** class stores information about individual particles. These classes are used to access and manipulate the particle data in PYTHIA 8.[149]

3.6 Tunes

A tune is a set of parameters that adjust the simulation of high-energy physics processes to conform with experimental data. These parameters adjust the simulation of the underlying event, multiparton interactions, colour reconnection, and other processes. Tunes are designed to match experimental data from a specific experiment, allowing researchers to ensure that their simulations are consistent with experimental data and that their results are directly comparable to those of other researchers. Consistency with experimental data also helps ensure that the simulations are robust and not sensitive to small parameter changes. The tunes available in PYTHIA 8 are Perugia 2011, Perugia 2012, Monash 2013, and 4C tunes, each with its own set of parameters. By adjusting the simulation parameters to match experimental data, a tune can improve the precision of the simulation, which is critical for high-energy physics research.[149]

The Monash tune, which serves as the current default tune for Pythia 8, is an example of such a manual approach. In this method, the person responsible for the tuning must understand the underlying physics processes, including parton showers, hadronisation, multiparton interactions, initial state radiation, and other relevant aspects. In Pythia 6, the default tune does not have a specific name like the Perugia or Monash tunes. Instead, it is a set of default parameter values built into the Pythia 6 code. The Pythia developers determine these default parameter values based on a combination of theoretical calculations, empirical knowledge, and comparisons to experimental data available at the time. The default tune in Pythia 6 provides a reasonable starting point for simulating high-energy particle collisions. However, since it is not explicitly optimised for the best possible agreement with experimental data, it is often recommended to use a more refined tune, like one of the Perugia tunes, for more accurate predictions and a possibly new interpretations of the underlying physics processes.

The Monash 2013 tune is the default parameter set in PYTHIA 8. Developed through collaboration with Monash University, this tune employs data from the High Energy Physics Database (HEP-DATA) and the Particle Data Group (PDG) to optimise its parameters and better describe experimental observations. The Monash 2013 tune focuses on non-diffractive, high momentum-transfer collisions involving the exchange of significant amounts of energy and momentum between interacting particles. It is primarily constrained using electron-positron (e^+e^-) collision data from the SLAC Large Detector (SLD) and the Large Electron-Positron Collider (LEP) [160][161]. These facilities provided precise measurements of various observables, which serve as a foundation for the tune. Initial state parameters such as ISR, MPIs and beam remnants are determined using data from the LHC [162]. MPI parameter-scaling uses data from the Tevatron, a former proton-antiproton collider [163]. Notably, the Monash 2013 tuning approach does not involve minimising the chi-squared (χ^2) value, a common method for quantifying the difference between experimental and simulated data.

To avoid overfitting, an uncertainty of five percent is added to each histogram bin, ensuring that the tune does not rely too heavily on specific experimental data points. Although the Monash 2013 tune is mainly designed for e^+e^- collisions, it incorporates the NNPDF2.3 LO QCD+QED PDF set to optimise the remaining parameters for hadronic collisions, which involve interactions between protons and other strongly interacting particles. By altering the PDF used for the hard-scattering matrix elements and leaving the same PDF for MPIs and the shower evolution, the Monash 2013 tune in Pythia 8 maintains the majority of shower features and underlying-event tuning.

Despite its many strengths, the Monash 2013 tune has limitations. For instance, while the tune provides a good overall description of various observables, it may struggle with certain aspects, such as the description of heavy quark production or the top quark pair (t-tbar) production process. In this case, the tune may not precisely reproduce the top quark transverse momentum distribution, leading to differences between the simulated and experimental data. Moreover, the Monash 2013 tune may not fully account for some of the latest theoretical developments, including higher-order perturbative QCD corrections or the interplay between colour reconnection and multiparton interactions.

3.7 Hard Processes and Parton Showers

Hard processes are the main focus of high-energy physics experiments such as those at the LHC. PYTHIA 8 handles hard processes in pp collisions through matrix elements. A matrix element is a mathematical expression that determines the probability of a specific hard process occurring in a collision. PYTHIA 8 uses matrix elements to calculate the probabilities of different hard processes occurring and then generates events accordingly.

PYTHIA 8 has a built-in library of matrix elements for a wide range of hard processes, including those mentioned previously. Once the matrix elements have been calculated, PYTHIA 8 uses them to generate events for the hard process. It also simulates the subsequent parton showering, fragmentation, and hadronisation of the produced partons, underlying events and multiple parton interactions, which are other important aspects of pp collisions.[150]

Parton showers refer to the sequential emissions of additional partons from the initial partons that participate in the hard scattering process. These emissions can occur both before and after the hard scatter process. Parton showers are a vital aspect of high-energy physics simulations and model the effects of the strong force on the final state of the collision. They can be considered a cascade of emissions, where each emission produces a new parton with lower energy than the previous one. The parton shower algorithm starts with the initial partons participating in the hard scatter process. It then simulates the emissions of additional partons, accounting for the probability of each emission occurring. The algorithm also considers the coherence effects of the parton shower, which means that the emissions of the partons tend to be collinear and follow a specific direction [13].

There are different models and algorithms available for simulating parton showers in pp collisions, such as the leading-logarithmic approximation (LLA), the next-to-leading-logarithmic approximation (NLA), and the matrix-element + parton-shower (ME + PS) approach. PYTHIA 8 handles parton showers in pp collisions using a leading-logarithmic approximation (LLA) algorithm. The LLA algorithm is a probabilistic approach that computes how additional partons are emitted from the initial partons that participate in the hard scatter process.

The parton shower algorithm in PYTHIA 8 starts with the initial partons that participate in the hard scatter process. It then simulates the emissions of additional partons, considering the probability of each emission occurring. PYTHIA 8 uses the transverse momentum of the emitted parton, the virtuality of the emitting parton and the process' evolution scale to generate each emission. The evolution scale is the energy scale at which the parton shower is performed, defined as the virtuality of the emitted parton.

In addition to the LLA algorithm, PYTHIA 8 also includes the next-to-leading logarithmic approximation (NLA) algorithm, which includes additional terms in the calculation of the probability of emissions, providing a more accurate description of the shower evolution [164].

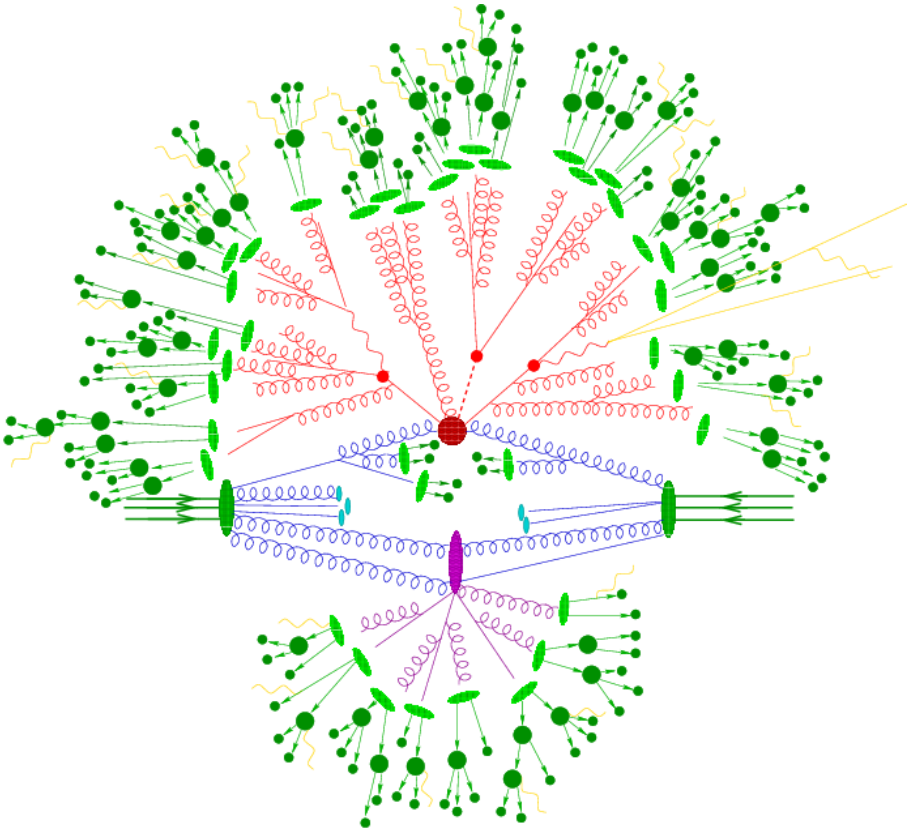


Figure 3.2: A visual representation of a particle collision event, as predicted by a Monte Carlo simulation. At the core of the interaction, indicated by a central red node, is the primary hard collision. Radiating from this point is a branching structure of lines and nodes, illustrating the process of Bremsstrahlung, where secondary particles are emitted, modeled here by parton showers. A secondary hard collision is highlighted by a purple node, indicating another point of significant interaction. The transformation from partons into hadrons is marked by transitions shown with light green nodes. The decays of these hadrons are denoted by dark green nodes. Additionally, the graphic includes yellow lines which denote the emission of soft photon radiation, a low-energy byproduct of the collision and decay processes.[14]

3.8 Hadronisation

Hadronisation is the process that defines how quarks and gluons produced in collisions form hadrons. The hadronisation process is considered a non-perturbative process, and several models have been proposed to describe the hadronisation process. Accurate modelling of the hadronisation process allows us to extract meaningful information from the detector measurements and compare them to theoretical predictions.

PYTHIA 8 includes a comprehensive model for hadronisation through the Lund String Model (used in the JETSET package) [103][13]. This model is a framework for studying

the confinement of quarks and gluons and their subsequent transformation into hadrons. Hadronisation starts with partons with a colour charge produced in a collision, forming colour strings between them. These colour strings represent the strong interaction, and the strings can be described as flux tubes with constant potential energy. Energy is transferred from the pair of partons (or a charge and anti-charge pair) to the strings when the charge and an anti-charge pair are pulled apart. With increasing distance between the partons, the potential energy in these strings increases linearly until the string breaks.

The breaking of strings occurs through the production of new quark-antiquark pairs. These new pairs form from the energy contained in the string, and subsequently, the quarks and antiquarks combine to create hadrons, and continues iteratively, leading to the production of multiple hadrons from a single string.[103]

3.8.1 Fragmentation

When colour strings are broken, the resulting quark and antiquark pairs form hadrons through fragmentation. The fragmentation process is based on the Lund symmetric fragmentation function which defines the probability distribution of the momentum fraction of each hadron produced during the string-breaking process.

In PYTHIA 8, the Lund String Model has been extended and modified to account for various scenarios, such as different quark flavours, endpoint quarks with large masses, and strings that contain gluons. The Lund symmetric fragmentation function depends on the parameters a and b, which can be tuned to match experimental data. This allows for predicting the properties and distribution of the final hadrons, such as their momenta, masses, and flavours.

3.8.2 Colour reconnection

Colour reconnection (CR) is a phenomenon that occurs during the hadronisation process, where colour strings rearrange their connections to minimise the overall potential energy of the system. In high-energy collisions, particularly in events with multiple parton interactions, several colour strings in close proximity increase the likelihood of colour reconnection. The concept of colour reconnection was motivated by the need to explain specific experimental observations that the original Lund String Model could not fully describe.

Colour reconnection significantly impacts the hadronisation process, as it can alter the properties of the final hadrons, such as their momenta, masses, and flavour compositions. Furthermore, colour reconnection can lead to the production of more massive hadrons and affect the overall multiplicity of the final-state particles. Including colour reconnection in

PYTHIA 8 allows for a more accurate description of experimental data, particularly in events involving multiple parton interactions, where several colour strings make reconnection more likely. The default CR mechanism is an MPI-based model, which is based on a two-step procedure that attempts to reduce the overall potential energy of the system by reorganising partons from separate MPI systems.

By default, CR is computed before resonance decays, but early decays are also an option. In addition to the default CR model, PYTHIA 8 offers several other CR models that can be selected and tuned according to the specific needs of the simulation or experimental data. Each of these alternative models approaches colour reconnection in different ways, and the choice of the model depends on the scenario being studied and the level of accuracy required.

Correctly choosing and tuning colour reconnection models in PYTHIA 8 can significantly impact the simulation results, particularly in describing event properties such as multiplicity, transverse momentum distributions, and event shapes. One must carefully consider the implications of the selected CR model and ensure that it provides a sufficient description of the data being analysed.

The QCD-based CR model is based on perturbative QCD and focuses on minimising the colour charge of the system. It considers the possibility of colour reconnection between final state partons by calculating the change in the strong coupling constant, α_s, resulting from a reconnection. This approach allows for a more dynamical treatment of colour reconnection, as it is based on the fundamental QCD interactions.

3.9 Particle Decays

PYTHIA 8 handles particle decays through a built-in library of decay modes for a wide range of unstable particles. Each decay mode is represented by a branching ratio. Branching ratios represent the probabilities of different decay channels for an unstable particle. They are essentially the fractions of a particle's decays resulting in a specific decay product set. The specific branching ratios in PYTHIA are primarily derived from the PDG. [13][150]

When PYTHIA 8 generates an event, it checks for unstable particles in the final state. PYTHIA 8 randomly selects a decay mode for each unstable particle based on the branching ratios of the available decay modes. The decay products are then added to the event record, and their properties, such as 4-momentum, are calculated based on the properties of the parent particle and the decay kinematics. The decay process also includes the decay of the unstable resonances inside the hadrons formed in the hadronisation process.

PYTHIA 8 also consists of various parameters that can be adjusted to fine-tune the decay process, such as the particle's lifetime, polarisation, or the mixing angles.[149]

3.9.1 Complications in Particle Decays

Although particle decays in PYTHIA may seem straightforward at first glance, numerous complexities necessitate adjustments to the basic methodology [13].

To ensure the correct kinematic distributions are generated, a matrix-element weight is applied after the phase space is created. This is done to account for the nature of the decay and is particularly important for non-zero spin particles or when there are correlations between decay products.

In the case of inclusive decays involving charm and bottom hadrons, the decay process is more complex since the number and type of decay products are not fixed. In an inclusive decay, the particle under consideration decays into one or more specified particles and any other accompanying particles. The inclusive decay is characterised by the presence of the specified particles, regardless of the other particles produced in the decay process. An inclusive decay for a B meson could be defined as $B \to D + X$, where X represents any number and combination of other particles. This inclusive decay focuses on the presence of a D meson in the final state without concern for the specifics of the accompanying particles. Dedicated decay models are used to handle these inclusive decays.[149][13]

Chapter 3 offered an overview of Heavy-Flavour physics in pp collisions, the ALICE detector, and a comprehensive analysis of PYTHIA, comparing and contrasting the functionalities of PYTHIA 6 and PYTHIA 8. The discussion centred on how PYTHIA is utilised in modelling pp collisions, and served to describe some of the theoretical underpinnings and the practical applications of PYTHIA in the simulation complex particle interactions. Building on this foundation, Chapter 4 will delve into the specifics of our analytical methodology, detailing how single muon yield distributions are computed in PYTHIA simulations and their significance in the broader scope of the ALICE experiment's research objectives.

CHAPTER 4

Analysis Details

4.1 Overview

Our objective was to determine the differential yield of muons from heavy-flavour decays as a function of transverse momentum (dN/dp_{T}) at forward rapidity ($-4 \leq \eta \leq -2.5$). The differential yield dN/dp_{T} encapsulates the change in yield (N) per unit of transverse momentum (p_{T}). The normalised yield, represented as $1/N_{\mathrm{evt}} \times \mathrm{d}N/\mathrm{d}p_{\mathrm{T}}$, allows for a comparative measurement across different event size scales by factoring in the total yield (N). For this investigation, we manipulate key parameters across multiple simulations, facilitating a comparative study of their impact on the resulting yields. These parameters include the centre-of-mass energy (5.02 TeV and 13 TeV) and the PDFs such as NNPDF2.3 and CTEQ6.6. These variations will enable us to discern the effects of different energy scales, PDFs and the version of PYTHIA on the outcomes of the simulations.

Our data extraction process involves identifying all primary muons in each collision event and tracing their lineage by iterating through the chain of "mother particles". We classify each muon's ancestor's flavour (pion, kaon, other light hadrons, charm, or beauty, including bare quarks and open hadrons). For every identified muon, we register crucial parameters such as momentum (p), transverse momentum (p_{T}), pseudorapidity (η), polar angle (θ), azimuthal angle (ϕ), rapidity (η), its production vertex and the corresponding ancestor's flavour. Subsequently, we will compare the histogram plots for the yield (dN/dp_{T}) and the normalised yield ($1/N_{\mathrm{evt}} \times \mathrm{d}N/\mathrm{d}p_{\mathrm{T}}$) for each identified ancestor flavour

or muon source. This approach will allow us to delineate the contribution of each flavour to the overall yield and its variability with p_{T}. Similarly, we analyse the normalised yields of muons from secondary decays of pions and kaons. A crucial aspect of our analysis is the comparison of normalised yields across different simulation environments. We will juxtapose results from standalone Pythia simulations with those obtained from integrated AliROOT with PYTHIA simulations (incorporating GEANT detector simulations). Additionally, we will scrutinise differences in outcomes between Pythia 6 and Pythia 8. The analysis will also compare the effects of different PDFs' on the normalised yields. The total yield from all primary muon sources will be compared to the experimentally measured inclusive single muon yield from official Run 2 data from ALICE from 2015 to 2018.

4.2 Standalone PYTHIA 8 Monte Carlo Simulations

4.2.1 Simulation Strategy

Parallel Event Generation

We simulate 80 million events per production on 8 CPU cores (10 million per core). The choice of this large number is guided by the need to achieve lower statistical errors and sufficient statistical significance in our analyses. Additionally, it improves our chances of capturing rarer processes in the high p_{T} region. This approach also facilitates far more efficient utilisation of computational resources and provides a substantial speed advantage, leading to much shorter running times. We also take advantage of storing data separately for each parallel simulation. Large amounts of data also have implications for the performance of input/output (I/O) operations, mainly if the storage medium is not particularly fast, and could add a significant overhead to our simulations.

4.2.2 Muon Selection

During the event processing, specific selection criteria are enforced within the inner loop to selectively focus on muons of interest (from the decays of the particles in table 4.1, thereby approximating the ALICE detector's acceptance characteristics. We aim to achieve this by implementing control flows to align with the actual ALICE detector's pseudorapidity, rapidity, azimuth, momentum, transverse momentum, and primary decay vertices. In essence, only muons originating from primary decays are considered. We introduce a series of specific kinematic, geometric, vertex, and decay cuts on the generated events to emulate the ALICE detector's capabilities without resorting to detailed detector simulation.

Setting	Description
`Beams:idA = 2212`	Beam 1 is a proton (code: 2212)
`Beams:idB = 2212`	Beam 2 is a proton (code: 2212)
`Beams:eCM = 13000`	Centre of mass energy is 13000 GeV
`Tune:pp = 14`	The Monash 2013 tune[165]
`PDF:pSet = 7`	Uses CTEQ6.6 PDF
`HardQCD:hardccbar = on`	Enables hard charm-anticharm production
`HardQCD:hardbbbar = on`	Enables hard bottom-antibottom production
`4:mayDecay = true`	Allows charm quarks to decay
`-4:mayDecay = true`	Allows anti-charm quarks to decay
`5:mayDecay = true`	Allows bottom quarks to decay
`-5:mayDecay = true`	Allows anti-bottom quarks to decay
`321:mayDecay = true`	Allows kaons to decay
`-321:mayDecay = true`	Allows anti-kaons to decay
`211:mayDecay = true`	Allows pions to decay
`-211:mayDecay = true`	Allows anti-pions to decay
`SoftQCD:nonDiffractive = on`	Enables non-diffractive processes

Table 4.1: Key configuration settings in Pythia 8

These selection criteria cater to ALICE's muon spectrometer's specific characteristics and functionalities and are applied as follows:

- **Kinematic Cuts**: These apply restrictions to the transverse momentum (p_{T}), momentum (p), rapidity (y) and/or pseudorapidity (η) of the muons.
- **Geometric Cuts**: Cuts based on the muon spectrometer's geometric acceptance are applied to the azimuthal angle (ϕ) and the polar angle (θ) of the particles.
- **Vertex Cuts**: These cuts are applied based on the position of particle production or decay vertices. The primary objective of these cuts is to ensure data quality. They focus on interactions near the interaction point, specifically within a 10 cm radius. Heavy quarks are produced in the early stages of a collision and have decay lengths ($c\tau$), typically in the range of 100-500 micrometres. These vertex cuts are essential in confirming that muons and other particles originate from the appropriate primary or secondary vertices.
- **Decay Cuts**: When interested in specific decay channels of a particle, particles can be filtered based on their parent and daughter particles. We apply such cuts to identify specific sources of muons to populate histograms. However, this procedure can also be performed in a separate analysis macro.

Cut Category	Selection Criteria	Value
Particle Type	PDG ID	13 (muon)
Kinematic	Pseudorapidity (η) range	-4.0 to -2.5
	Transverse momentum (p_{T}) range	0.5 GeV/c to 20.0 GeV/c
	Momentum (p) range	4.0 GeV/c to 10^8 GeV/c
Geometric	Polar angle (θ) range	2.985 rad to 3.107 rad
	Azimuthal angle (ϕ) range	0.0 rad to 2π rad
Vertex	Distance from primary vertex	Less than 100 mm
Decay	Mother particle PDG ID range	400 to 599 (heavy quarks)

Table 4.2: Selection criteria for muons of interest categorised by cut types.

4.2.3 Differential Single Muon Yield Determination

This section describes the methodology used to extract the yield of primary single muon sources, specifically through the computation of their dN/p_{T} distributions. The extraction approach varies based on the simulation environment. In standalone PYTHIA simulations, the process involves a straightforward extraction of histograms by filling the p_{T} value of each accepted muon. However, when integrating with the AliROOT framework—where the detector's effects are simulated—the established processes and tools of the ALICE offline framework are utilised. This requires running analysis tasks on the CERN Computing Grid and using specialised classes and functions of the AliROOT and AliPhysics libraries.

Several ROOT histograms were initialised for different cases: the energies 5.02 TeV and 13 TeV, and for each energy, we have different PDFs (CTEQ6.6, NNPDF23, NNPDF30). We compute the "total" dN/dp_{T} histogram (for all muons), and dN/dp_{T} histograms for multiple primary decay sources - namely pions, kaons, charm, and beauty. Each histogram is initialised with 200 bins spanning a p_{T} range from 0 to 100 GeV/c. In total, we fill 36 histograms with the p_{T} values from the data stored in each `TTree` from each one of the eight ROOT files per simulation.

To analyse the muon momentum spectra, we examined the differential cross-section dN/dp_{T} across different collision energies (5.02 TeV and 13 TeV) and PDF sets (CTEQ6.6 and NNPDF23). The analysis framework captured both the total muon spectrum and the contributions from different primary decay sources - pions, kaons, charm, and beauty quarks. This approach allowed systematic comparison of how the muon spectra are influenced by different theoretical inputs (PDFs) and experimental conditions (collision energies).

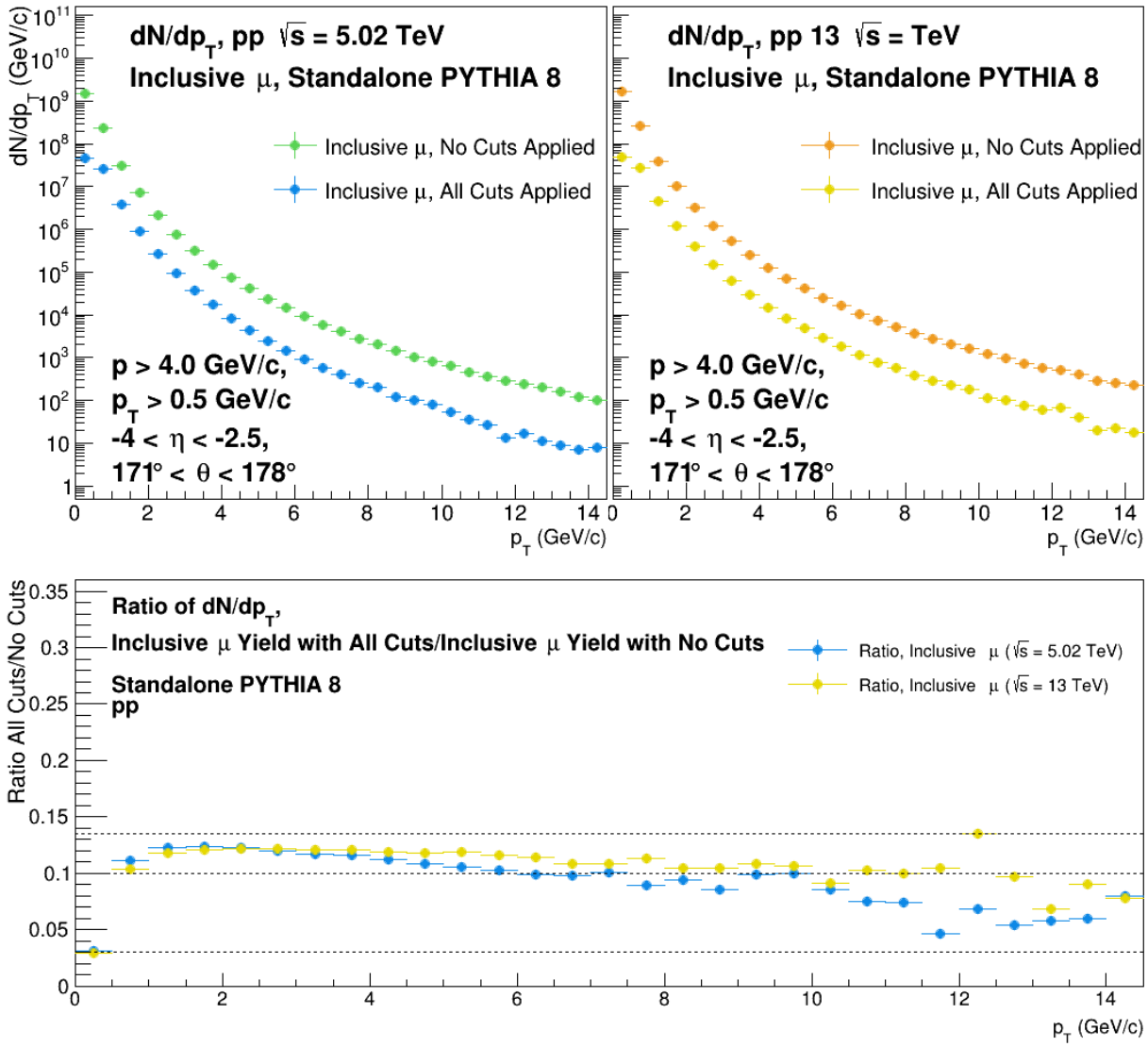


Figure 4.1: The computed transverse momentum distributions of all muons (inclusive) before and after kinematic cuts were applied (5.02 TeV left, 13 TeV right). Kinematically, muons with pseudorapidities (η) ranging from -4.0 to -2.5, transverse momenta (p_{T}) from 0.5 GeV/c to 20.0 GeV/c, and momenta (p) from 4.0 GeV/c up to 100 million GeV/c were selected. Geometrically, they had polar angles (θ) from 2.98451 rad to 3.10669 rad, and azimuthal angles (ϕ) between 0 and 2π rad. Additionally, muons originating within 100mm of the primary vertex and having mother particles with PDG IDs between 400 and 599 (indicating heavy quarks) were considered.

At $\sqrt{s} = 5.02$ TeV (in Figure 4.1), the application of acceptance cuts leads to a significant decrease in the inclusive muon yields, particularly at lower p_{T}. For muons with $p_{\mathrm{T}} \leq 0.5$ GeV/c, the yield is reduced by approximately 97%. In the p_{T} range from 0.5 to 1 GeV/c, the yield reduction is around 89%, corresponding to a yield ratio of roughly 0.1. The yield ratio reaches its maximum value of approximately 0.13 at 1 GeV/c (87% reduction),

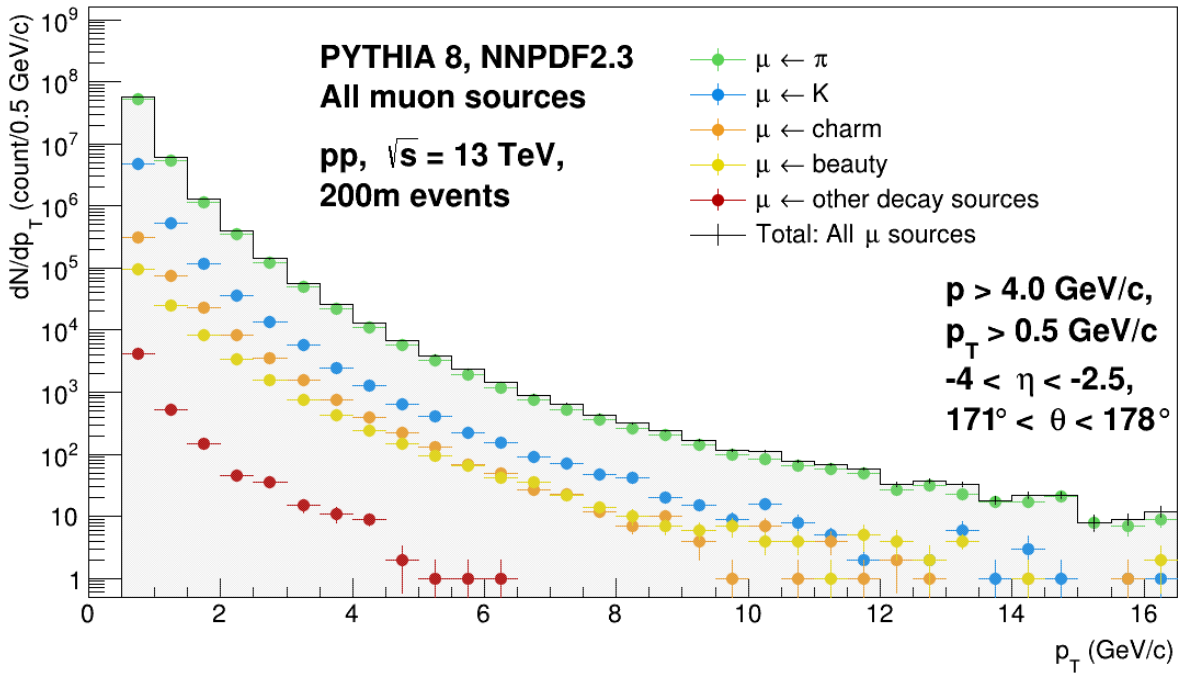


Figure 4.2: The transverse momentum yield distributions of muons from all primary decay sources at $\sqrt{s} = 13$ TeV, after kinematic cuts were applied (standalone PYTHIA 8). This figure delineates the contributions from distinct primary sources: pions (green circles), primary kaons (blue circles), charm (orange circles), beauty (yellow circles), and the sum of all other primary muon sources (red circles). The black line represents the total inclusive muon yield (sum) of the individual sources.

before declining at higher p_{T}. Between 1–2 GeV/c, the yield reduction remains at 87–88%. Beyond this range, the yield suppression increases with higher p_{T}, with reductions ranging from 88% to 93% as p_{T} extends from 2 to 8 GeV/c.

At $\sqrt{s} = 13$ TeV (in Figures 4.1 and 4.2), a similar reduction of 97% is observed for muons with $p_{\mathrm{T}} \leq 0.5$ GeV/c. However, the range in which the yield reduction maintains at 88-89% is broader, extending from p_{T} of 1 to 6 GeV/c, compared to the 1 to 4 GeV/c range at $\sqrt{s} = 5.02$ TeV. Therefore, the suppression of yield for $p_{\mathrm{T}} \geq 2$ GeV/c is less pronounced at $\sqrt{s} = 13$ TeV.

For all PDF types at $\sqrt{s} = 13$ TeV, yield reduction trends within the 0-10 GeV/c p_{T} range do not show a significant variation, marking no clear separation between NNPDF 3.0 and other PDFs. Additionally, the gradient of the yield ratio decline at $\sqrt{s} = 13$ TeV is lower, indicating a less steep increase in suppression with rising p_{T} compared to the data at $\sqrt{s} = 5.02$ TeV.

4.3 ALICE Monte Carlo Productions with AliROOT

4.3.1 ALICE MC Productions Using AliROOT & PYTHIA

Parameter	PYTHIA 6	PYTHIA 8
Number of Events	70,066,200	69,854,000
Event Generator	PYTHIA 6.425	PYTHIA 8.210
PDF	CTEQ5L	NNPDF2.3 QCD+QED LO
Tune	Perugia2011	Monash 2013
GEANT Version	3.21/11	3.21/11
Collision System	p-p	p-p
Low-p_{T} Muon Trigger	CMSL7-B-NOPF-MUFAST	CMSL7-B-NOPF-MUFAST
High-p_{T} Muon Trigger	CMSH7-B-NOPF-MUFAST	CMSH7-B-NOPF-MUFAST

Table 4.3: Simulation parameters for 5.02 TeV ALICE MC productions

Parameter	PYTHIA 8
Number of Events	67,760,800
Event Generator	PYTHIA 8.xxx
PDF	NNPDF2.3 QCD+QED LO
Tune	Monash 2013
GEANT Version	3.21/11
Collision System	p-p
Muon Trigger	CMSL7-B-NOPF-MUFAST

Table 4.4: Simulation parameters for 13 TeV ALICE MC production

The simulation of detector responses to particle collisions is crucial and requires specialised software beyond the scope of event generators like PYTHIA 8. AliROOT (ALICE's offline framework) fills this role by providing detailed simulation of particle interactions with detector materials and the digitisation of physical signals. This enables us to reconstruct and analyse events as they would occur in the actual detector setup.

Monte Carlo productions were performed for pp collisions at centre-of-mass energies of $\sqrt{s} = 5.02$ TeV and $\sqrt{s} = 13$ TeV. For each energy, simulations were conducted using both PYTHIA 6 and PYTHIA 8 event generators. The key simulation parameters are summarised in Tables 4.3 and 4.4.

The analysis employs two triggers to select muons for inclusive single muon production: **CMSL7-B-NOPF-MUFAST** and **CMSH7-B-NOPF-MUFAST**. The **CMSL7-B-NOPF-MUFAST** trigger serves as the low p_{T} single muon trigger with a threshold of $p_{\mathrm{T}} \geq 2$ GeV/c. This selection addresses the significant contribution of muons with $p_{\mathrm{T}} \leq 2$ GeV/c from the decays of primary charged pions and kaons. The **CMSH7-B-NOPF-MUFAST** trigger applies a high p_{T} threshold of 4.2 GeV/c. Both triggers require coincident signals in the V0A and V0C detectors [166].

The trigger naming scheme is called a "Trigger Class" and has the following components:

- **B**: This signifies that the trigger is set to respond to events where bunches from both beams are present at the collision point, as specified by the LHC's bunch crossing mask settings. The bunch crossing mask is a control mechanism that dictates which instances of beam intersection are considered for triggering and data collection.
- **NOPF**: This acronym stands for "No Past-Future Protection",' meaning that there is no mechanism active to prevent or correct erroneous trigger decisions influenced by events from the immediate past or near future. This is used in the trigger systems to ensure that the collected data is relevant to the current event being analysed.
- **MUFAST**: This refers to a cluster of ALICE sub-detectors. Within this cluster, MTR (Muon Trigger) is crucial for triggering data collection when muons are detected. The SPD (Silicon Pixel Detector), MCH (Muon Chamber), and AD (Alice Diffractive detector) aid in tracking and analysing events, while T0 and V0 have distinct functions in event timing and selection, respectively. The MUFAST cluster works in coordination to effectively capture and analyse events of interest.

4.3.2 Differential Single Muon Yield Determination

Analysing ALICE MC data sets involves a different approach. It uses AliPhysics and AliROOT to run physics analysis tasks on the Grid. Our main goal is to create a file, "AnalysisResults.root", which contains histograms for each muon source. Running an analysis task on the ALICE Grid (MonaLISA) is a multi-step process. The first step is to write the analysis code and configuration settings and launch the job. MC productions are accessed by referring to the AOD file in MonaLISA. Each collision event in the `AOD.Muons.root` file is processed sequentially by the analysis task. The `UserExec()` method defines the event-by-event analysis code and is executed for every event. The `aliroot runAnalysis.C` command launches the task on the Grid, and this task consists of a master job with multiple sub-jobs, each running the same analysis tasks on different data sets within the MC production. The output files are generated on independent grid nodes and merged into one output file, and downloaded locally.

Analysis Task Configuration

The `AliUtilityMuonAncestor` class is a crucial part of our analysis task and involves classifying muons based on their sources (referred to as 'ancestors'). Its detailed design and numerous muon identification and classification methods make it a powerful tool. Each method takes a muon track and an MC event as input and returns a Boolean value indicating whether the muon matches the specified lineage.

The core of the utility is the `BuildAncestor()` method. It takes a particle track and an MC event as inputs and reconstructs the ancestry of the muon. The method retraces the decays that produced the muon through the event record, classifying it according to the kind of particle from which it originated. This is performed by checking particle IDs (PDG codes) against the predefined categories such as light quarks, charm quarks, beauty quarks, tau, and more. Several checks are performed to ensure that the track is a valid Monte Carlo track, matches a Monte Carlo particle, and is indeed a muon. The lineage of the muon is then built by iterating over its mothers or progenitor particles. For each ancestor, the method checks if it is primary or secondary, whether it is a quark, and if it falls into one of the predefined categories. If the ancestor is a primary particle, further checks classify it according to its flavour (light, charm, beauty, quarkonium, tau).

The specific methods of `AliUtilityMuonAncestor` provide detailed classifications:

- `IsMuon()`: Checks if the track is a muon.
- `IsBeautyMu()` and `IsBeautyChainMu()`: Classify muons originating from beauty quark decays.
- `IsCharmMu()` and `IsCharmChainMu()`: Classify muons originating from charm quark decays.
- `IsDecayMu()`: Classify muons from primary light hadron decays.
- `IsHadron`: Identify whether the particle is a hadron and not a muon.
- `IsSecondaryMu()`: Classify muons arising from the absorber's secondary decays.
- `IsUnidentified()`: Identify muons that could not be classified.
- `IsWBosonMu()` and `IsZBosonMu()`: Classify muons originating from W and Z boson decays.
- `IsBJpsiMu()`: Classify muons from J/Psi decays in beauty hadrons.

The `IsDecayMu()` method is designed to identify muons originating from the decays of primary light hadrons such as pions and kaons. It checks that the particle in question

is indeed a muon with a light hadron as a parent while also verifying that it is not a secondary particle. On the other hand, the `IsHadron()` method verifies whether a given track corresponds to a hadron (ensuring that is not a muon track, to avoid analysing hadron tracks that may have been misclassified as muons. Lastly, the `IsSecondaryMu()` method identifies muons that emerge from secondary decays within the absorber material when hadrons such as pions and kaons interact with it. These interactions can produce additional muons, which can then be classified using the `IsSecondaryMu()` method.

Initially, tracks are filtered based on their position within the muon spectrometer's acceptance, ensuring they align with the detector's geometry. These tracks' p_{T} are then captured in histograms, with a dedicated histogram specifically for muon tracks. Subsequent checks ensure that the muon tracks align with specific trigger conditions. Finally, the pDCA of each track is computed and assessed, and tracks that fail to meet the specified pDCA requirement are excluded.

4.4 Normalised Differential Yields

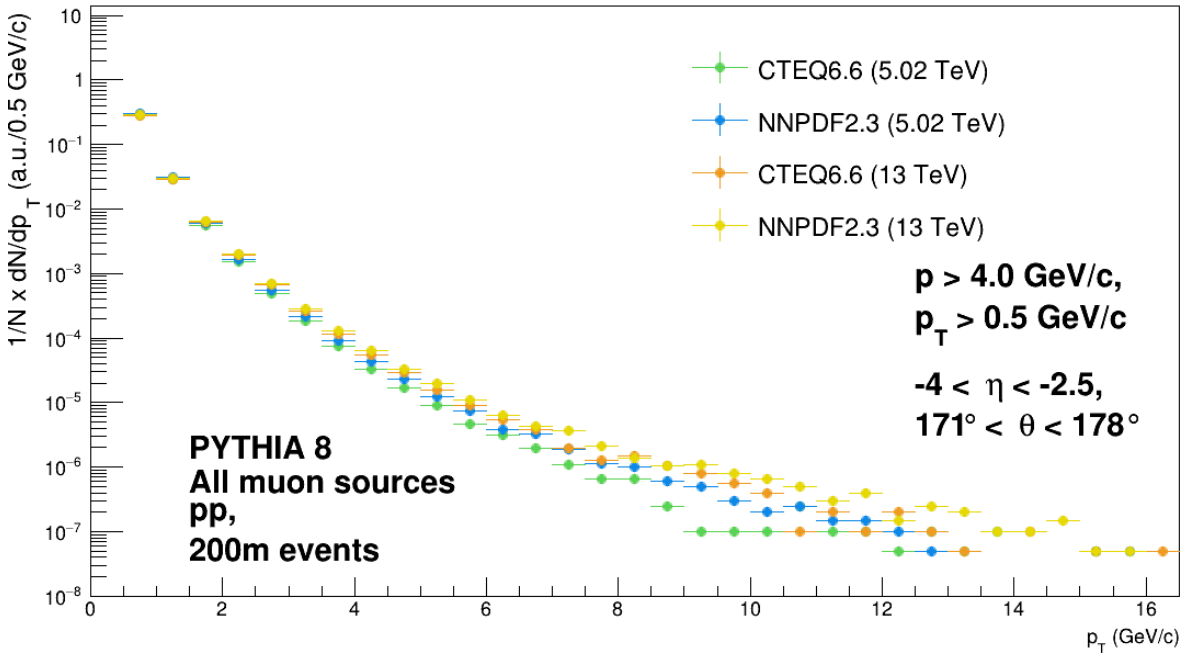


Figure 4.3: Normalised transverse momentum distribution of all muons (inclusive) for all PDFs in the standalone PYTHIA 8 MC productions, covering centre-of-mass energies of $\sqrt{s} = 5.02$ TeV and $\sqrt{s} = 13$ TeV. In this case, $N = 80$ million.

In this section, we compute $\frac{1}{N}\frac{dN}{dp_{\mathrm{T}}}$, the normalised yield distribution as a function of p_{T}. Here, N is the total number of events observed. For the standalone PYTHIA productions, $N = 80$ million, and the details for the AliROOT productions are provided in tables 4.3 and 4.4. dN/dp_{T} is the differential yield as a function of transverse momentum. Dividing the differential yield by the total number of events normalises the distribution. The normalised yield is a way to represent data so that it can be compared regardless of the total number of events or particles observed. It is particularly useful for comparing results from different MC productions. It is important to note that all normalised yield distributions in this section and subsequent sections were computed with their respective acceptance cuts applied. Statistical errors have been computed for all figures in this section, but are too small to see for $p_{\mathrm{T}} \leq 10 GeV/c$ in most cases. The normalised muon yield distributions from standalone PYTHIA 8 and ALICE AliROOT Monte Carlo productions exhibit the same steep decline with increasing p_{T}, consistent with expected particle production mechanisms in pp collisions. The standalone PYTHIA 8 simulations (Figure 4.3, showing the normalised p_{T} distributions for different PDF sets) demonstrate robust statistics up to $p_{\mathrm{T}} \approx 12$ GeV/c, with the NNPDF2.3 PDF set showing marginally higher normalised yields compared to CTEQ6.6 beyond $p_{\mathrm{T}} > 6$ GeV/c.

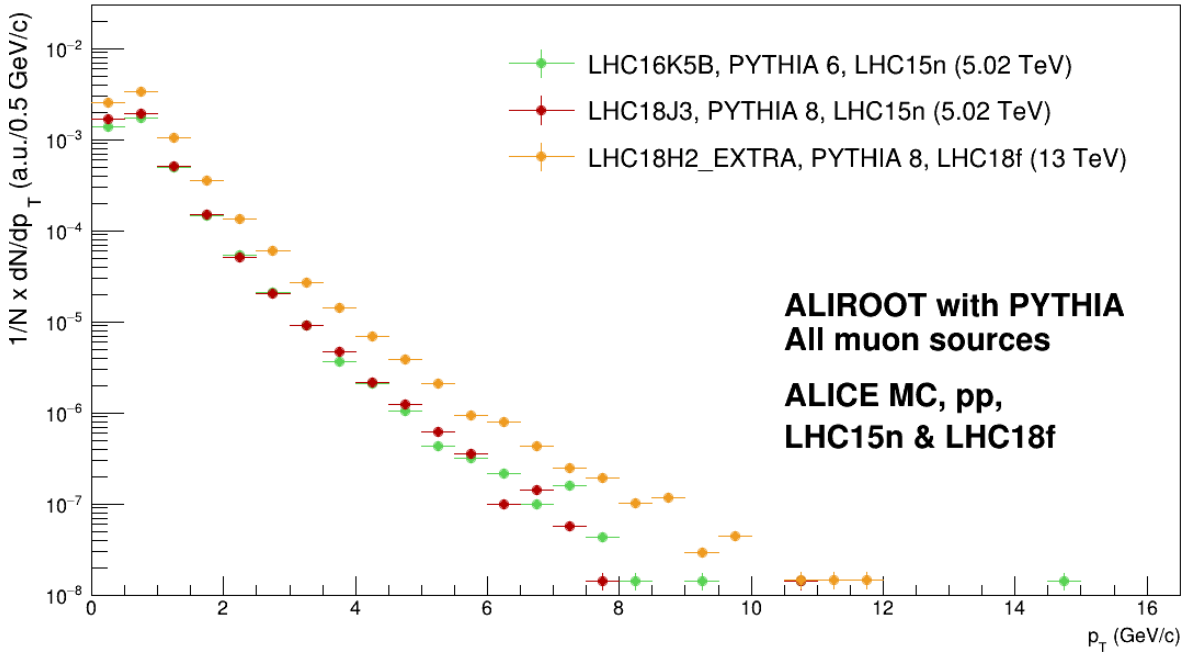


Figure 4.4: Normalised transverse momentum distribution of all muons (inclusive) for all PDFs in ALICE AliROOT MC productions, covering centre-of-mass energy levels of $\sqrt{s} = 5.02$ TeV and $\sqrt{s} = 13$ TeV. The values of N for the ALICE AliROOT MC productions are stated in Tables 4.3 and 4.4. Note that for $p_{\mathrm{T}} > 8.0$ GeV/c, there are limited statistics for AliROOT with PYTHIA (ALICE MC productions), unlike the case of standalone PYTHIA 8 shown in Figure 4.3.

In contrast, the ALICE AliROOT implementations (Figure 4.4, displaying normalised yields with full muon acceptance cuts) exhibit limited statistics beyond $p_{\mathrm{T}} > 8$ GeV/c, particularly pronounced in the LHC18H2_EXTRA configuration at $\sqrt{s} = 13$ TeV. Both simulation frameworks demonstrate the expected enhancement in normalised yields at $\sqrt{s} = 13$ TeV compared to $\sqrt{s} = 5.02$ TeV, consistent with increased particle production at higher centre-of-mass energies. The statistical uncertainties remain well-controlled in the low and intermediate p_{T} regions ($p_{\mathrm{T}} < 8$ GeV/c) across all configurations in both frameworks, providing confidence in the reliability of the simulations in these kinematic regions.

4.4.1 Analysis of the Centre-of-Mass Energy Dependence

This section presents a comparative analysis of how single muon production scales with collision energy, examining both inclusive muon yields and specific contributions from charm and beauty hadron decays. We compare normalised yields at centre-of-mass energies of $\sqrt{s} = 5.02$ TeV and $\sqrt{s} = 13$ TeV using both standalone PYTHIA 8 Monte Carlo simulations and AliROOT. The analysis considers muons from all parent particles listed

in Table 4.1, studying their distributions as a function of transverse momentum (p_{T}). To isolate the effect of collision energy, we maintain consistent conditions by using identical PDF sets and PYTHIA versions while varying only the centre-of-mass energy.

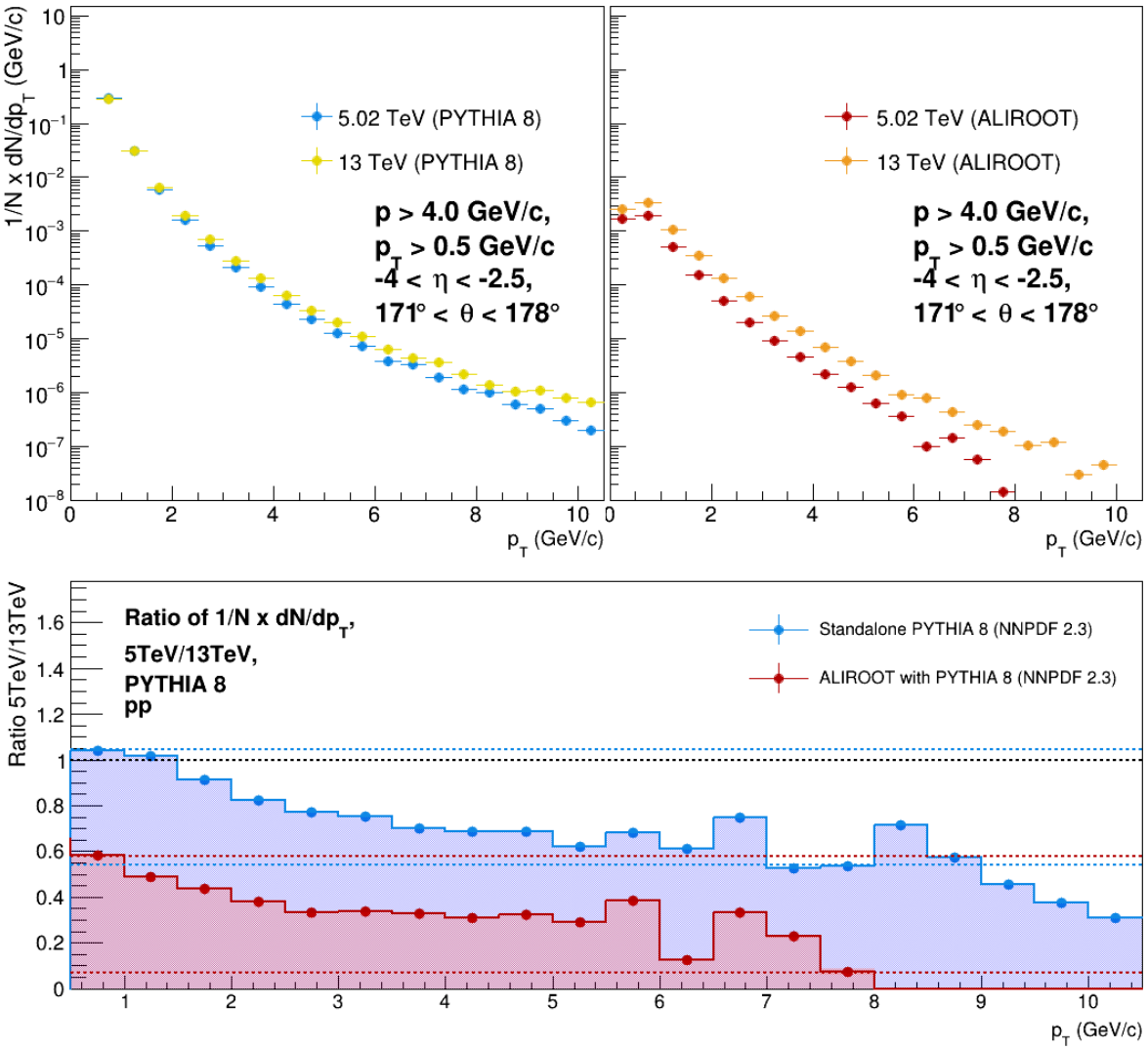


Figure 4.5: Comparison of the normalised transverse momentum distributions of all muons from decays of primary particles (total), comparing yields at two centre-of-mass energy, $\sqrt{s} = 5.02$ TeV and $\sqrt{s} = 13$ TeV. The left plot illustrates yields from standalone PYTHIA 8 MC productions using the NNPDF2.3 PDF. The right plot depicts results from ALICE PYTHIA 8 MC productions using AliROOT, using the NNPDF2.3 PDF. The bottom pane contains ratio histograms of the normalised yields at $\sqrt{s} = 5.02$ TeV (numerator) and $\sqrt{s} = 13$ TeV (denominator). The dotted blue and red lines represent the respective maximum values of the ratios for standalone PYTHIA 8 and ALIROOT. The dotted black line is a reference line to aid with visually comparing the ratios to unity.

The ratio histograms for each configuration are computed by dividing the normalised yields at $\sqrt{s} = 5.02$ TeV by those at $\sqrt{s} = 13$ TeV (see Figure 4.5). These ratios provide visual and quantitative insights into how muon production scales with increasing collision energy. The analysis separately investigates inclusive muon yields and those specifically from charm and beauty decays, allowing us to identify distinct energy-dependent patterns in heavy-flavour production. The results are supported by AliROOT simulations incorporating realistic detector effects through GEANT 3 modelling, providing a detailed framework for predicting how muon yields scale with collision energy in future studies.

The normalised single muon yield distributions in Figure 4.5 demonstrate the expected distinct characteristics at different p_{T} scales. In standalone PYTHIA 8 simulations, the normalised yields between $\sqrt{s} = 5.02$ TeV and $\sqrt{s} = 13$ TeV are comparable at $p_{\mathrm{T}} < 1$ GeV/c (low p_{T}. We expected and confirmed a clear energy-dependent divergence as p_{T} increases beyond 1 GeV/c, with $\sqrt{s} = 13$ TeV exhibiting progressively higher yields until statistical limitations arise at $p_{\mathrm{T}} > 12$ GeV/c. ALICE MC (AliROOT) productions exhibited a similar trend but showed more pronounced statistical limitations, with data constrained beyond $p_{\mathrm{T}} = 5.5$ GeV/c and $p_{\mathrm{T}} = 8$ GeV/c for $\sqrt{s} = 5.02$ TeV and $\sqrt{s} = 13$ TeV respectively. The energy dependence was captured in the ratio plots ($\sqrt{s} = 5.02$ TeV to $\sqrt{s} = 13$ TeV). The ratio behaviours differ between the two simulation frameworks - while standalone PYTHIA 8 showed a smooth decrease with p_{T}, AliROOT simulations exhibited ratios exceeding unity at low p_{T} (maximum 1.25 at $p_{\mathrm{T}} = 0.5$ GeV/c) before decreasing. This divergence in ratio behaviour was particularly pronounced in the p_{T} range of 0.5-2.0 GeV/c.

The normalised p_{T} yield distributions of muons from heavy-flavour decays, shown in Figures 4.6 and 4.7, demonstrate distinct characteristics between standalone PYTHIA 8 and AliROOT with PYTHIA 8. For muons from charm decays muons in standalone PYTHIA 8, the ratio ($\sqrt{s} = 5.02$ TeV to $\sqrt{s} = 13$ TeV) exhibits a pronounced energy dependence, decreasing from 0.9 at $p_{\mathrm{T}} = 0.5$ GeV/c to approximately 0.4 at $p_{\mathrm{T}} = 4$ GeV/c. In contrast, the AliROOT simulations have a more moderate energy dependence, with ratios ranging from 0.5 at $p_{\mathrm{T}} = 0.5$ GeV/c to 0.3 at $p_{\mathrm{T}} = 4$ GeV/c, suggesting that the addition of accurate detector simulation leads to limited energy-dependent divergence in the production of muons from primary hadron decays.

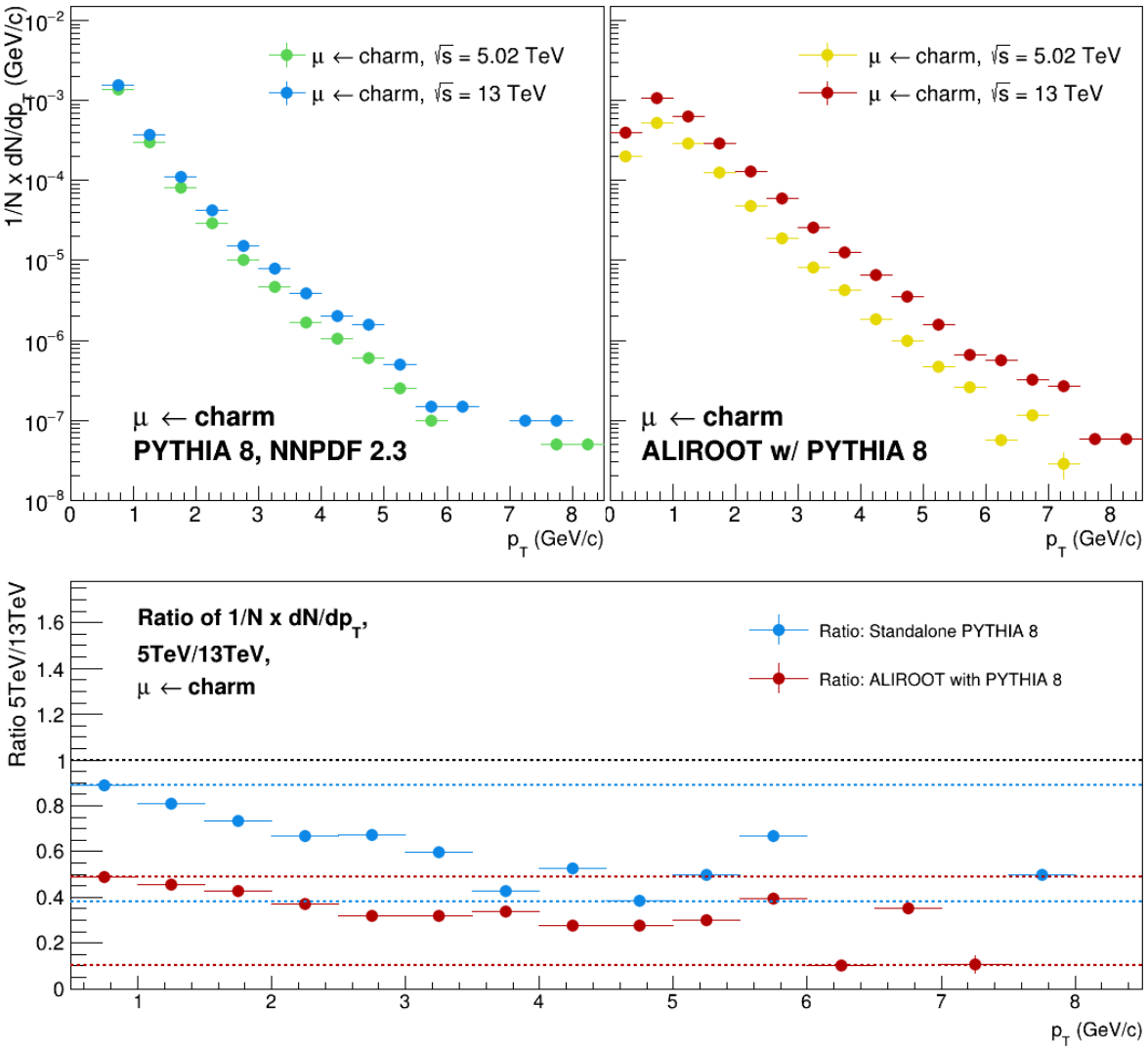


Figure 4.6: Comparison of the normalised transverse momentum distributions of muons from charm, at centre-of-mass energies $\sqrt{s} = 5.02$ TeV and $\sqrt{s} = 13$ TeV. The left plot illustrates the normalised yield distributions were computed from standalone PYTHIA 8 Monte Carlo simulations using the NNPDF2.3 PDF. The right plot illustrates the normalised yield distributions were computed from AliROOT with PYTHIA 8, using the NNPDF2.3 PDF. The bottom plot comprises ratios of the normalised yield distributions at $\sqrt{s} = 5.02$ TeV (numerator) and $\sqrt{s} = 13$ TeV (denominator). The respective maximum values of the ratios for standalone PYTHIA 8 and ALIROOT are represented by the dotted blue and red lines. The dotted black line indicates unity.

Beauty-decay muons exhibit systematically lower ratios than charm, reflecting the more significant mass threshold for beauty production. In standalone PYTHIA 8, the ratio decreases from 0.5 at $p_{\mathrm{T}} = 0.5$ GeV/c to 0.4 at $p_{\mathrm{T}} = 2.5$ GeV/c, while AliROOT maintains a nearly constant ratio of approximately 0.3 across the measurable p_{T} range. This reduced energy dependence for beauty production aligns with theoretical expectations, as the

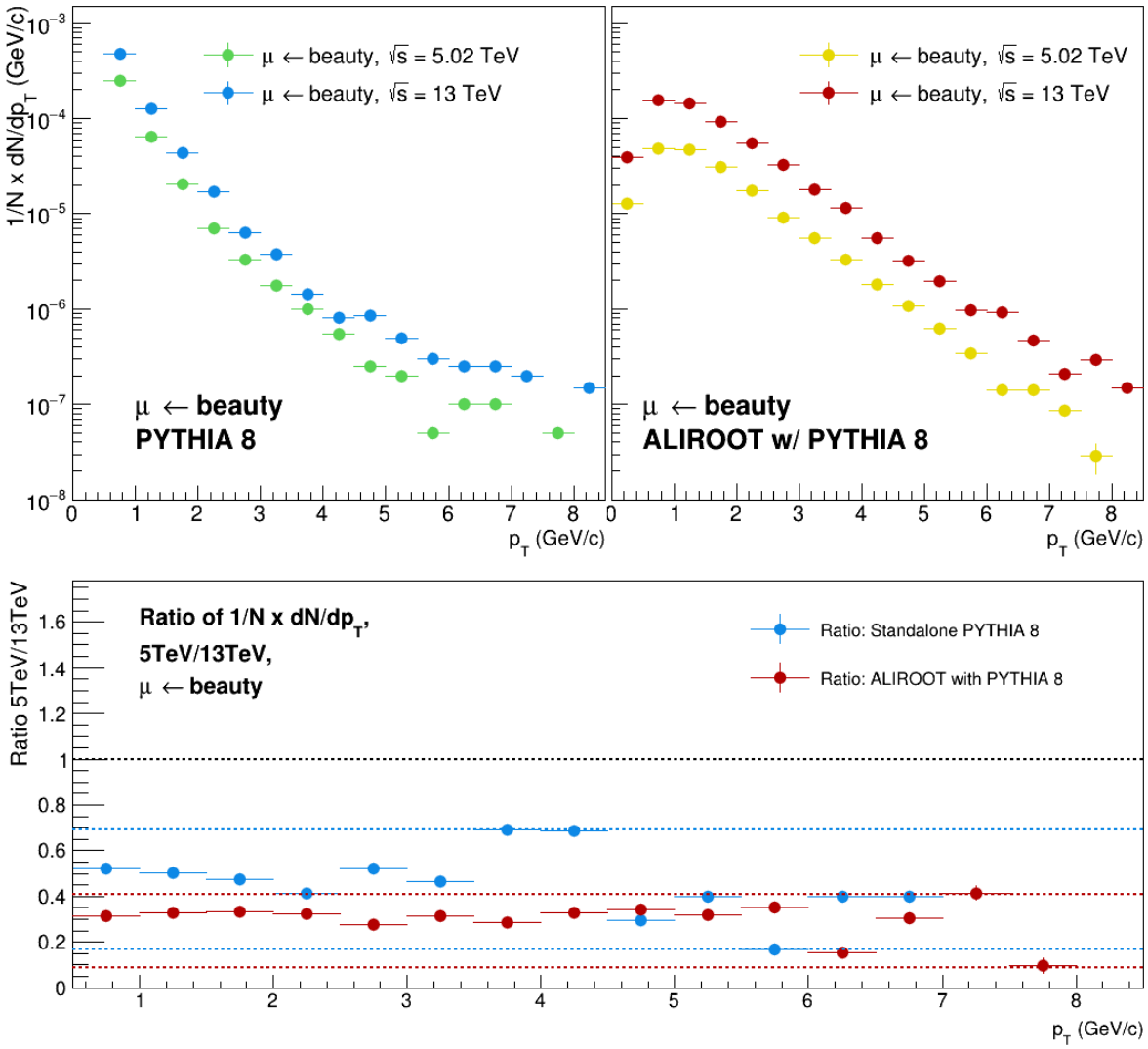


Figure 4.7: Comparison of the normalised transverse momentum distributions of muons beauty decays, at centre-of-mass energies $\sqrt{s} = 5.02$ TeV and $\sqrt{s} = 13$ TeV. The left plot illustrates the normalised yield distributions were computed from standalone PYTHIA 8 Monte Carlo simulations using the NNPDF2.3 PDF. The right plot illustrates the normalised yield distributions were computed from AliROOT with PYTHIA 8, using the NNPDF2.3 PDF.

higher mass of beauty quarks makes their production less sensitive to moderate increases in centre-of-mass energy. The available statistics for beauty measurements become limited at notably lower transverse momentum ($p_{\mathrm{T}} = 3$ GeV/c) compared to charm ($p_{\mathrm{T}} = 6$ GeV/c), particularly in AliROOT, reflecting the lower production cross-section for the heavier beauty quarks.

Comparing these heavy-flavour results to inclusive single muon yields (Figure 4.5) reveals the dominance of light hadron decays at low p_{T}. The inclusive ratios in standalone

PYTHIA 8 start notably higher at 0.95 for $p_{\mathrm{T}} = 0.5$ GeV/c, decreasing to 0.25 at $p_{\mathrm{T}} = 12$ GeV/c, indicating that muons from pion and kaon decay, which are less sensitive to the centre-of-mass energy difference, dominate the low-p_{T} region. The consistent pattern of lower ratios progressing from inclusive to charm to beauty muons reflects the increasing mass of the parent particles and their corresponding production thresholds.

There are systematic differences between simulation frameworks, with AliROOT exhibiting more stable ratios across categories whilst standalone PYTHIA shows stronger p_{T} dependence. These differences arise from the detector effects, trigger requirements, and event selection modelled in AliROOT but absent in standalone PYTHIA. This underscores the necessity of accounting for detector response when comparing theoretical predictions to experimental measurements, either through unfolding experimental data or through full detector simulation of theoretical predictions.

4.4.2 Analysis of PDF Dependence

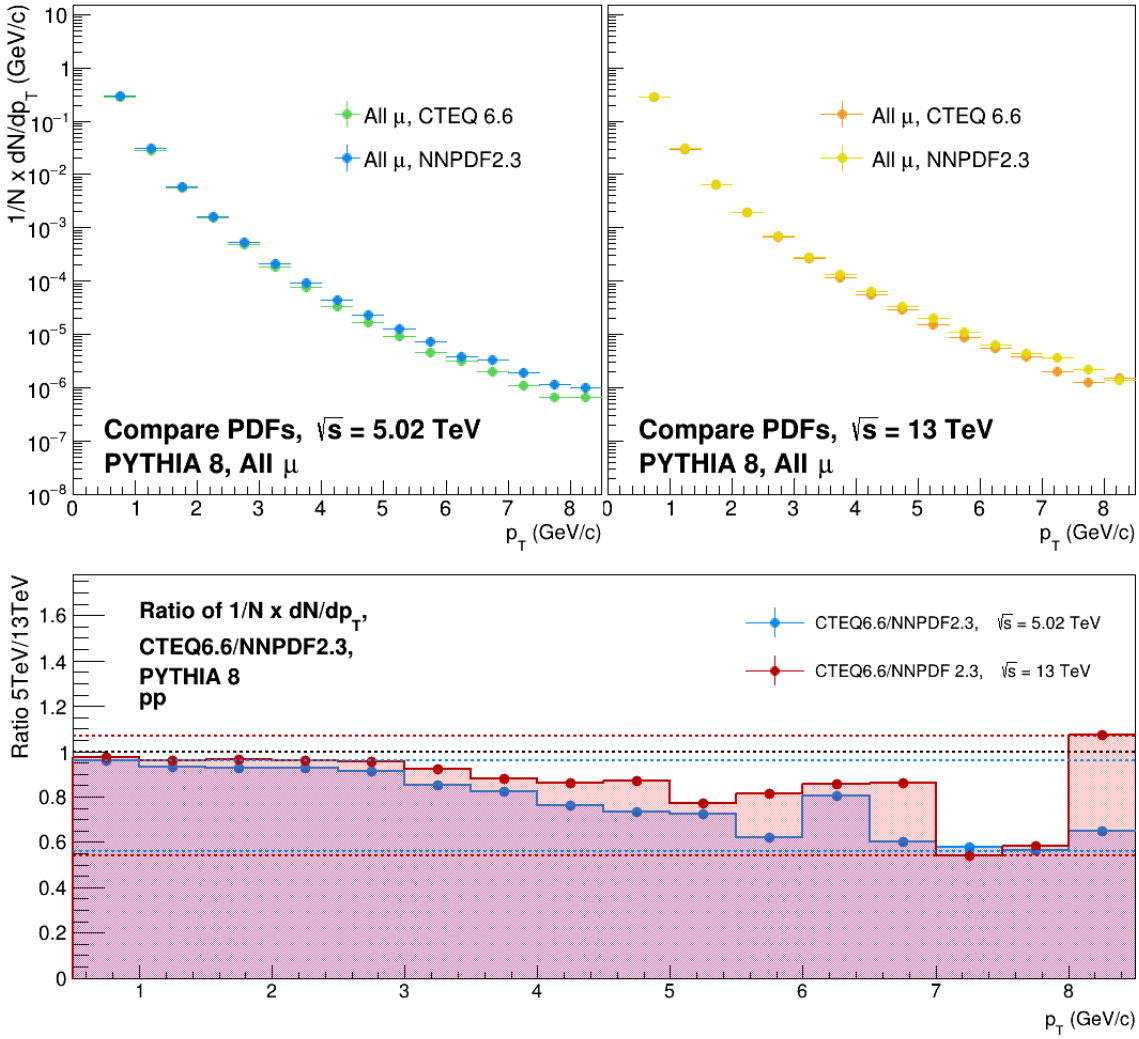


Figure 4.8: Comparison of the normalised transverse momentum distributions of all muons from decays of primary particles (total) between PDFs ($\sqrt{s}$ = 13 TeV). The left plot compares normalised yields from standalone PYTHIA 8 MC productions using the CTEQ6.6 and NNPDF2.3 PDFs. The right plot compares normalised yields from standalone PYTHIA 8 MC productions using the NNPDF2.3 and NNPDF3.0 PDFs.

This section presents a comparative analysis of the normalised inclusive yields of muons as a function of p_{T}, using different parton distribution functions (PDFs). The comparison involves muons originating from the decays of various particles listed in Table 4.1, focusing on muons from heavy-flavour decays. The analysis is based on only standalone PYTHIA 8 Monte Carlo simulations and aims to analyse the impact of PDF choices on the inclusive single muon production spectrum (see Figure 4.8). For this study, we structured the comparison to match datasets by centre-of-mass energy, and PYTHIA version while varying the PDFs to directly assess their influence on the yields. To quantify these differences, we

computed the ratios of CTEQ6.6 (numerator) to NNPDF2.3 (denominator). The ratio histograms offer visual and quantitative insights into how the choice of PDF affects the normalised yield distribution of inclusive single muons.

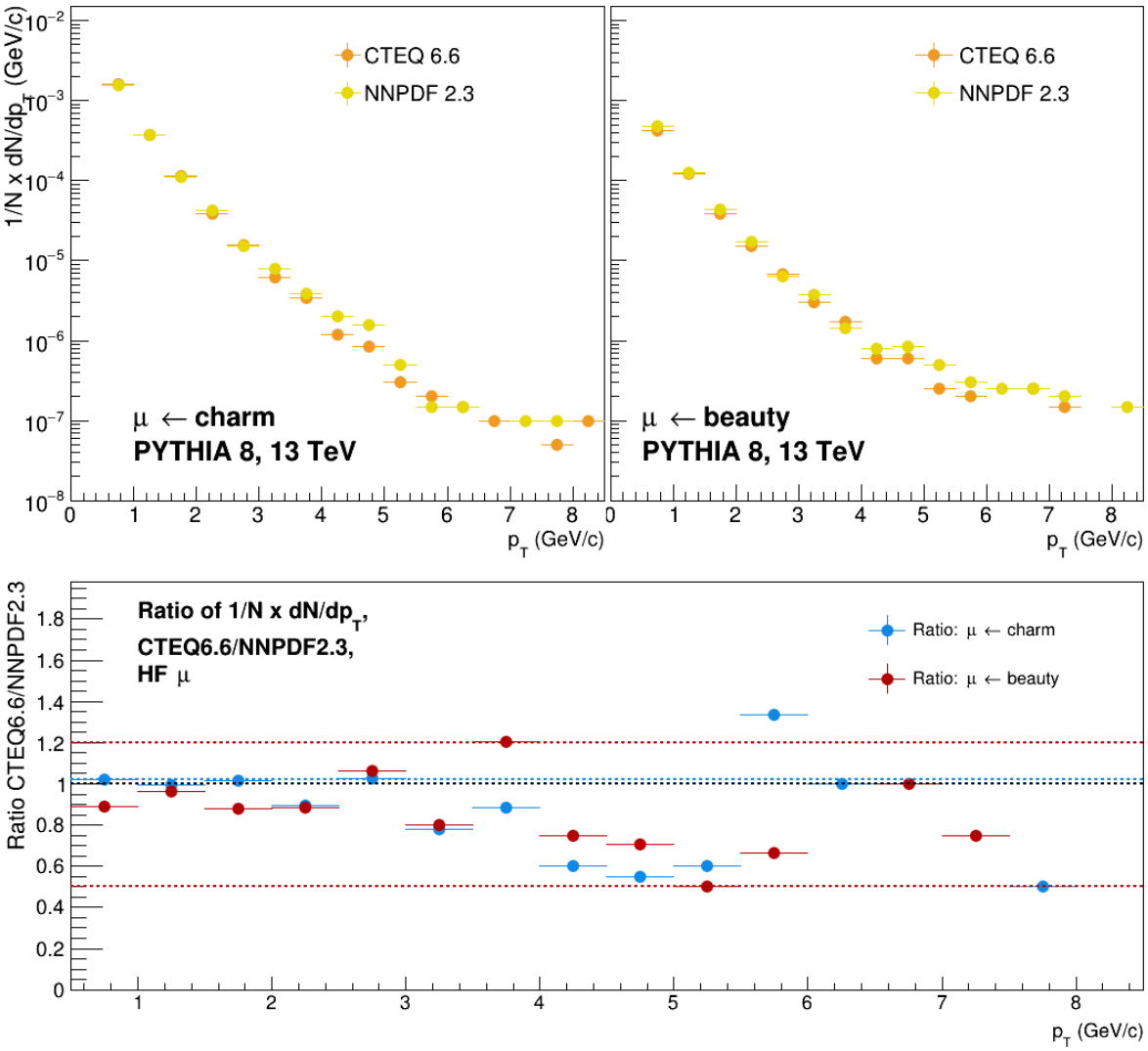


Figure 4.9: Comparison of the normalised transverse momentum distributions muons from decays of heavy flavours (at centre-of-mass energy $\sqrt{s} = 5.02$ TeV and $\sqrt{s} = 13$ TeV). The left plot compares normalised yield distributions from charm decays using standalone PYTHIA 8 with the CTEQ6.6 and NNPDF2.3 PDFs for $\sqrt{s} = 5.02$. The right plot compares normalised yield distributions from charm decays using standalone PYTHIA 8 with the CTEQ6.6 and NNPDF2.3 PDFs for $\sqrt{s} = 13$

In Figure 4.9, at low transverse momenta ($p_{\mathrm{T}} \approx 0.5$ GeV/c), the normalised yield distributions predicted by CTEQ6.6 and NNPDF2.3 are nearly indistinguishable across both centre-of-mass energies ($\sqrt{s} = 5.02$ TeV and $\sqrt{s} = 13$ TeV). This agreement persists to $p_{\mathrm{T}} = 3$ GeV/c, where both PDFs yield similar distributions. However, beyond $p_{\mathrm{T}} = 3$

GeV/c, divergence becomes apparent, with NNPDF2.3 consistently predicting higher normalised yields compared to CTEQ6.6 as p_{T} increases. This pattern is observed across the charm, beauty, and inclusive datasets, suggesting a shared behaviour for all sources of muons at higher p_{T}. The ratio of normalised yields between the two PDFs (CTEQ6.6 to NNPDF2.3) is close to 1.0 at $p_{\mathrm{T}} = 0.5$ GeV/c for both centre-of-mass energies, fluctuating between 0.9 and 0.97 until $p_{\mathrm{T}} = 3$ GeV/c. A more pronounced divergence in the ratio occurs at $\sqrt{s} = 5.02$ TeV, with the ratio decreasing from approximately 0.85 at $p_{\mathrm{T}} = 4$ GeV/c to 0.7 at $p_{\mathrm{T}} = 6$ GeV/c. The ratio decreases gradually for $\sqrt{s} = 13$ TeV, from approximately 0.9 at $p_{\mathrm{T}} = 4$ GeV/c to 0.8 at $p_{\mathrm{T}} = 6$ GeV/c. This indicates that the impact of PDF choice on the yields is more pronounced at lower centre-of-mass energies.

In Figure 4.9, when analysing the normalised p_{T} yield distributions of muons from charm and beauty decays, CTEQ6.6 tends to predict higher yields at lower p_{T}, particularly for charm decays where the maximum ratio reaches ≈1.1 at $p_{\mathrm{T}} = 2.5$ GeV/c, and for beauty decays where it reaches ≈1.2 at $p_{\mathrm{T}} = 3.5$ GeV/c. This result illustrates the PDF-dependent systematic uncertainty in the lower transverse momentum range, with variations of approximately 10% for charm decays and 20% for beauty decays. This model-dependent uncertainty must be included in the systematic uncertainty budget for low-p_{T} heavy-flavour measurements. The higher yields predicted by CTEQ6.6 at these low p_{T} values represent the systematic uncertainty arising from differences in gluon PDF parameterisations at small-x, which dominate heavy-quark production in the soft p_{T} spectrum. Only comparison with experimental data can validate which PDF more accurately describes this kinematic regime..

As p_{T} increases, a distinct crossover occurs at around $p_{\mathrm{T}} = 3.5$ GeV/c, where NNPDF 2.3 begins to predict higher yields for both charm and beauty decays. This crossover point is consistent across decay channels and centre-of-mass energies, indicating systematic PDF-dependent uncertainty in higher-p_{T} predictions. The increased yields predicted by NNPDF 2.3 at higher p_{T} demonstrate that PDF-dependent systematic uncertainties exhibit strong kinematic dependence. The fact that this crossover is similar for both charm and beauty decays suggests that above this momentum range, the production mechanisms are less influenced by quark mass and more by the dynamics captured by NNPDF 2.3. This demonstrates that PDF choice can introduce significant model-dependent uncertainty in higher-momentum regions.

While the inclusive muon yields (in Figure 4.8) show a similar pattern of divergence between PDFs as seen in the heavy-flavour decays, they are slightly less sensitive to the crossover point around $p_{\mathrm{T}} = 4$ GeV/c. The inclusive yields show a more gradual transition, which is likely due to the contributions from lighter hadrons, such as pions and kaons, which dilute the direct effects seen in charm and beauty decays. The lighter

hadrons, contributing to the overall inclusive yield, smooth out the sharp transition observed in the heavy-flavour decays. This indicates that inclusive muon yields exhibit reduced sensitivity to PDF variations compared to charm- or beauty-specific channels, though PDF-dependent systematic uncertainties must still be quantified for both measurement types.

At $p_{\mathrm{T}} > 7$ GeV/c, the statistical uncertainties increase significantly, limiting our ability to draw definitive conclusions. However, the general trend shows NNPDF2.3 continuing to predict higher normalised yield predictions at higher p_{T}, indicating continued PDF-dependent systematic uncertainty in hard-scattering processes at high p_{T}. The distinct crossover behaviour at $p_{\mathrm{T}} \approx 4$ GeV/c indicates that production mechanisms in this region are susceptible to PDF choice, highlighting the kinematic dependence of PDF-induced systematic uncertainties and the need for experimental data to constrain PDF parameterisations across different momentum regimes.

4.4.3 Analysis of the Effects of PYTHIA Versions

This section compares normalised transverse momentum distributions of muons from charm and beauty decays between PYTHIA 6 and PYTHIA 8 within ALICE AliROOT Monte Carlo productions. Given the fundamental architectural differences between these versions discussed in Chapter 2, our comparison focuses on their emergent behaviours rather than individual features. The analysis is conducted at fixed $\sqrt{s}$, excluding standalone PYTHIA Monte Carlo productions, to characterise the generators' predictions of heavy-flavour decay muons. Normalised yield ratios are examined across the available p_{T} spectrum, focusing on statistically significant regions to ensure robust characterisation of the model-dependent differences between of each PYTHIA version.

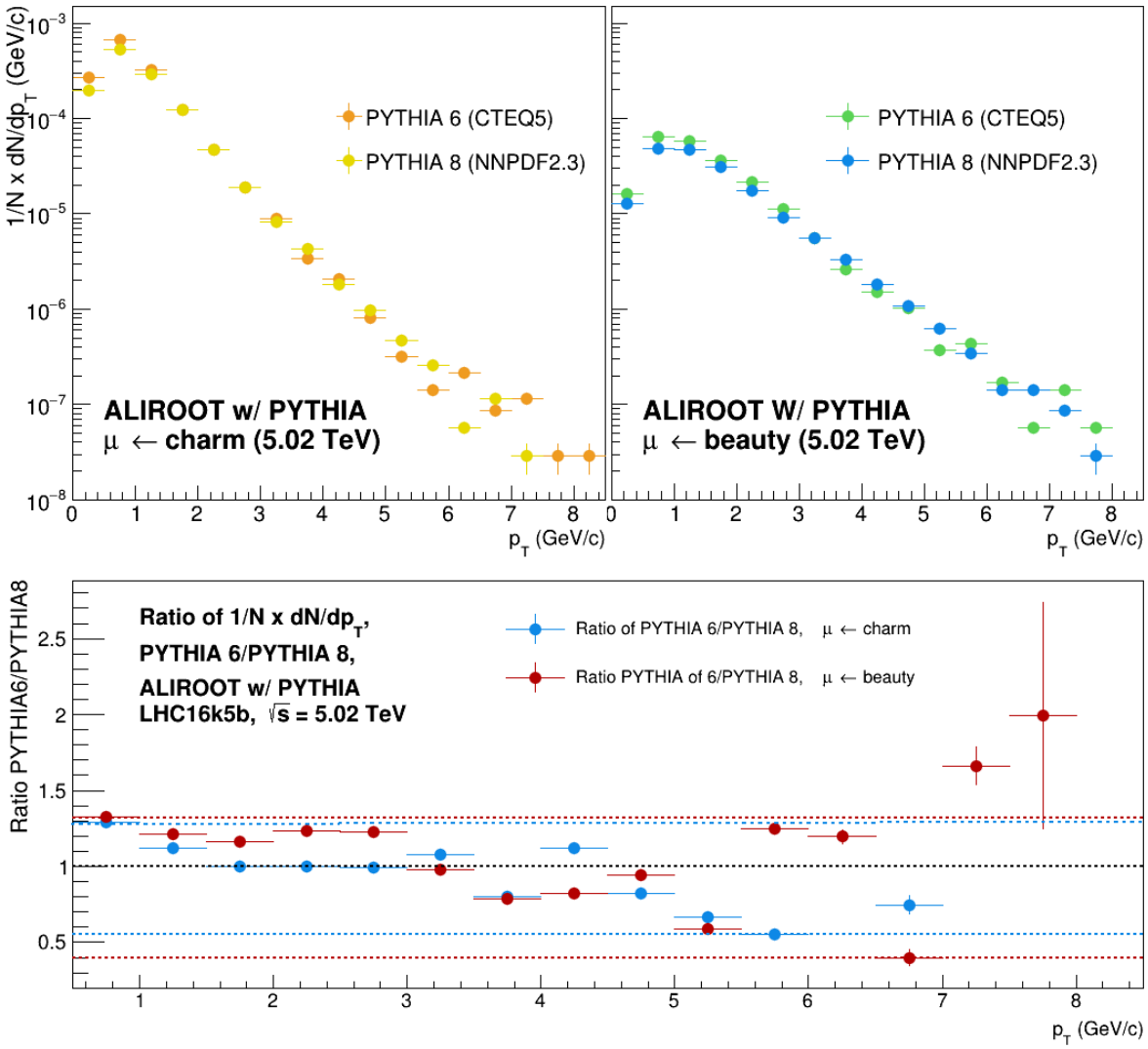


Figure 4.10: Normalised transverse momentum distributions of muons from charm (left) and beauty (right) decays, comparing the differences between PYTHIA 6 (CTEQ5) and PYTHIA 8 (NNPDF2.3) at centre-of-mass energy $\sqrt{s} = 5.02$ TeV, using AliROOT.

In Figure 4.10, distinct patterns emerge for both charm and beauty decay channels, reflecting essential insights into the behaviour of heavy-flavour muon production under different PYTHIA versions. For charm decays, while the overall shape of the normalised yield distribution remains similar between PYTHIA 6 (CTEQ5) and PYTHIA 8 (NNPDF 2.3), the enhanced production seen at low p_{T} in PYTHIA 6, where the ratio peaks at 1.3 at 0.5 GeV/c, demonstrates that PYTHIA 6 predicts higher charm quark production in this p_{T} range. This enhancement reduces to unity by $p_{\mathrm{T}} = 1.5$ GeV/c, indicating that the difference between the versions becomes negligible at slightly higher momenta. The exact match between the two versions in the p_{T} range of 1.5-3.0 GeV/c suggests that, in this range, the models provide consistent predictions, indicating reduced model-dependent systematic uncertainty in this specific momentum window where both versions converge.

The crossover observed at $p_{\mathrm{T}} \approx 3.5$ GeV/c, where PYTHIA 8 begins to predict higher yields, is particularly significant as it signals a transition in the relative production dynamics at slightly higher transverse momenta. We observe that PYTHIA 8 has enhanced yields of charm production as p_{T} increases, representing a systematic uncertainty that must be quantified for higher-p_{T} measurements.. The decrease in the PYTHIA 6 to PYTHIA 8 ratio to approximately 0.8 in the 3.5-4.5 GeV/c range highlights the growing dominance of PYTHIA 8 in this regime, representing a 20% model-dependent systematic uncertainty at higher p_{T} that must be evaluated through comparison with experimental data.

For beauty decays, there is a similar general pattern in the normalised yield distribution, but with more pronounced differences at low p_{T}. This further illustrates the difference in the characteristics of PYTHIA 6 and PYTHIA 8 at low p_{T}. The higher ratios, reaching a maximum of 1.3 at 0.5 GeV/c and staying relatively stable within the 1.1 to 1.3 range in the p_{T} interval of 1-4 GeV/c, suggest that PYTHIA 6 enhances beauty quark production more consistently in a more comprehensive p_{T} range compared to charm. This represents a systematic uncertainty of 10–30% in beauty production at low to mid p_{T}, arising from differences in generator modelling, which must be quantified in beauty decay analyses at these transverse momenta.. We observe that a crossover occurs again around 3.5 GeV/c, with a more gradual transition compared to charm, illustrating that PYTHIA 8 eventually overtakes PYTHIA 6 in predicting beauty yields at higher p_{T}. This gradual shift could indicate a more nuanced behaviour in beauty production sensitive to transverse momentum, indicating continued generator-dependent systematic uncertainty in higher-momentum beauty quark production.

The broader implications of these observations point to an apparent p_{T}-dependent variation in heavy-flavour muon production between PYTHIA 6 and PYTHIA 8. PYTHIA 6's higher predicted beauty yields, sustained across a broader p_{T} range, represent significant model-dependent systematic uncertainties in the low-p_{T} regime. Comparison with experimental data is necessary to validate generator predictions, and using both PYTHIA versions provides an estimate of the systematic uncertainty envelope. However, as p_{T} increases, the consistent enhancement of PYTHIA 8 in normalised yields (compared to PYTHIA 6) demonstrates generator-dependent systematic uncertainty at higher energy and transverse momenta. This p_{T}-dependent transition indicates that neither version is universally superior, and the specific momentum range of interest might dictate the choice of generator.

The cumulative effect of these differences between PYTHIA 6 and PYTHIA 8 stems from distinct PDF sets, MPI models, and tunes results in these observable variations. The enhanced beauty production in PYTHIA 6 may support a scenario in which beauty quarks

play a more significant role at low p_{T}. At the same time, PYTHIA 8's uniformity across the entire spectrum suggests it may offer better predictions for inclusive studies. These findings suggest that, for a comprehensive understanding of heavy-flavour production, it may be helpful to incorporate both versions of PYTHIA in comparative analyses, particularly when analysing production across varying energy scales. Crossover points may also serve as markers for understanding when one version outperforms the other, and future studies should take these transitions into account when selecting the appropriate PYTHIA version for their analyses.

4.4.4 Effects of Accurate Detector Simulation

This section compares the normalised single muon yield distributions between simulations, including realistic detector effects (AliROOT with PYTHIA) and standalone PYTHIA Monte Carlo productions. By keeping the centre-of-mass energy ($\sqrt{s} = 13$ TeV), PYTHIA version, and PDF (NNPDF2.3) constant, the analysis aims to isolate the impact of accurate detector simulation on the yield distributions. Normalised yield ratios are computed to assess relative muon production between the two setups, with trends and variations scrutinised throughout the available transverse momentum (p_{T}) spectrum, with a focus on statistically robust regions to ensure that the analysis is based on reliable data.

Both simulations implement similar kinematic, geometric, vertex, and decay cuts to filter events and select muons of interest. The standalone PYTHIA configuration attempted to replicate the acceptance of the ALICE detector through criteria including pseudorapidity, p_{T}, polar angle, and vertex distance constraints. However, despite these stringent cuts, significant yield distribution differences persist, particularly in the low-p_{T} region.

Although the number of generated events normalised both simulations, this method overlooks the complex detector efficiencies in AliROOT, where many events are rejected due to trigger requirements, energy thresholds, and detector interactions. In contrast, standalone PYTHIA processes all events equally, lacking the selective trigger mechanisms that make AaliROOT's event selection process more representative of actual experimental conditions. A further complication arises due to the lack of realistic energy loss simulations in standalone PYTHIA. This leads to a significant difference in the single muon yields of heavy-flavour decays after normalisation of standalone PYTHIA simulations and AliROOT simulations with accurate detector simulation (using GEANT3).

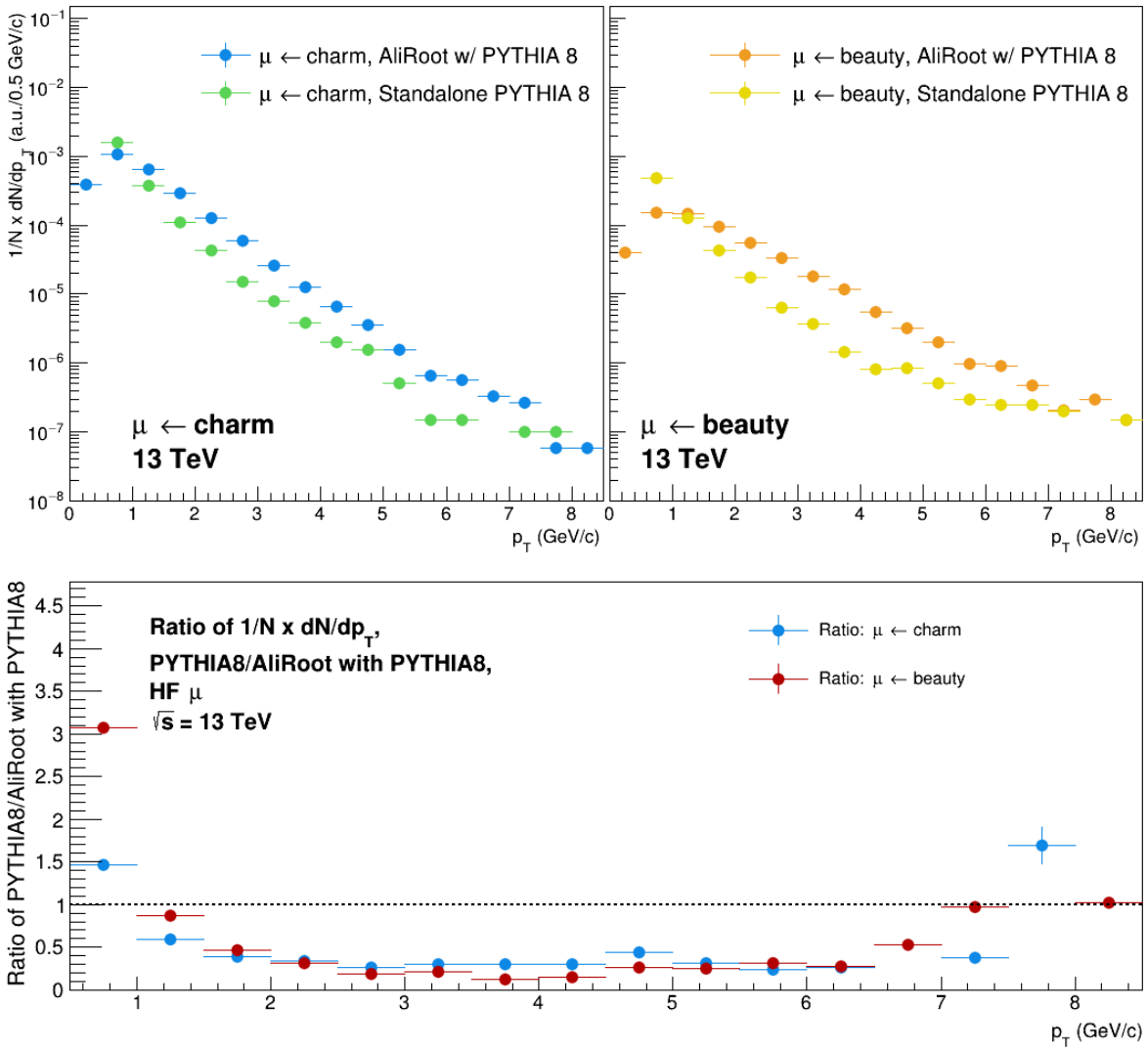


Figure 4.11: Normalised transverse momentum distributions of muons from charm (left) and beauty (right) decays, comparing the effects of accurate detector simulation (AliROOT with PYTHIA 8 and NNPDF2.3) and standalone PYTHIA 8 with NNPDF2.3 ($\sqrt{s} = 5.02$ TeV).

Figure 4.11 reveals interesting differences in the normalised transverse momentum (p_{T}) distributions of muons from charm and beauty decays, between standalone PYTHIA 8 and AliROOT with PYTHIA 8 predictions at $\sqrt{s} = 13$ TeV. For decays of charm, the normalised yield in AliROOT with PYTHIA 8 is higher in most of the p_{T} range compared to standalone PYTHIA, except in the low-p_{T} region (0.5–1.0 GeV/c), where standalone PYTHIA produces approximately 1.5 times more muons. A similar but more pronounced trend is seen for beauty decays, with standalone PYTHIA yielding about 3.1 times more muons in the low-p_{T} range. These discrepancies highlight the fact that standalone PYTHIA does not account for key detector suppression effects such as the front absorber and muon filter.

In the p_{T} range of 1.5 to 6 GeV / c, the ratio of standalone PYTHIA to AliROOT with PYTHIA drops below 0.5. The ratio remains relatively flat for charm decays, while for beauty decays, it decreases before levelling off at around 4 GeV/c. In the statistically reliable region of p_{T} = 2.0–5.5 GeV/c, charm decays exhibit higher ratios than beauty, indicating a more consistent relative suppression in AliROOT. In contrast, below p_{T} = 2.0 GeV/c, the beauty ratios surpass those of charm. In AliROOT, the **CMSL7-B-NOPF-MUFAST** trigger for low-p_{T} muons (with a threshold of $p_{\mathrm{T}} \geq 2$ GeV/c) and the **CMSH7-B-NOPF-MUFAST** trigger for higher-p_{T} muons (with a threshold of $p_{\mathrm{T}} \geq$ 4.2 GeV/c) are designed to select specific muon events that meet the detector's physics objectives. These triggers are sensitive to energy thresholds and ensure that events with sufficient muon energy are selected for further analysis. In standalone PYTHIA, we lack this real-world trigger system, meaning that more low-energy events are considered, skewing the distribution towards lowerp_{T} yields. In AliROOT, triggers ultimately impact the normalised yield. Events in AliROOT are filtered through these triggers, making the selection process more selective and reducing the number of low-energy muons passed to the analysis stage. Standalone PYTHIA lacks this selective trigger mechanism, meaning that all events, including those with low-p_{T} muons, are processed equally, resulting in an inflated yield of low-energy muons and suppression of the overall normalised yield spectrum.

For charm decays, the overall shape of the p_{T} distributions is similar between the two simulation approaches, differing mainly in yield. In contrast, beauty decays display more distinct shapes, with AliROOT showing a more gradual decline at higher p_{T}, while standalone PYTHIA exhibits a steeper drop. This behaviour is due to the larger mass of beauty quarks, which typically results in higher-energy muons interacting more significantly with the detector materials. The results suggest a relatively stable and consistent behaviour across smaller p_{T} intervals, implying that a constant factor or multiplier could potentially describe the differences between standalone PYTHIA and AliROOT with PYTHIA within these intervals. This constancy likely arises because charm quark decays, involving lighter quarks, are less sensitive to energy-dependent processes and the specific details of detector response. The effects of filtering, energy loss, and multiple scattering are still present. However, their impact on the overall shape of the p_{T} distribution appears to be more uniform and less dependent on energy.

In contrast, we observe a more pronounced energy-dependent divergence for beauty decays in the shape of the p_{T} distributions between the two simulations. This divergence, particularly at higher p_{T}, suggests that beauty quarks, which are heavier and typically involve higher-energy decays, are more sensitive to the detailed detector effects modelled in AliROOT, such as bremsstrahlung, energy loss, and absorption in the front absorbers and muon filters. Unlike charm decays, the results for beauty decays show that a simple

constant or multiplier is insufficient to describe the discrepancies between the simulations. The beauty decay distribution requires further analysis, particularly at higher p_{T}, to fully capture the energy-dependent effects.

This is evidence that charm quark decays are less sensitive to the effects details of detector simulation, particularly at higher p_{T}. However, the higher yield in AliROOT is probably due to the accurate simulation of the detector response, including absorbers and trigger matching, which results in better background suppression and event selection efficiency.

The discrepancies observed with standalone PYTHIA, particularly the overestimation of low-p_{T} muons, illustrate the limitations of using theoretical generators without accounting for the detector response. The results show that even without the need for explicit background subtraction,standalone PYTHIA overestimates low-p_{T} muons, especially from beauty decays. This discrepancy highlights that detector effects, such as triggering systems (CMSL and CMSH), energy loss, and multiple scattering in absorbers, play an important role in accurately selecting muons from heavy-flavour decays. In AliROOT, these effects are carefully simulated, leading to a more realistic reconstruction of muon yields. For HF studies in the semi-muonic channel at ALICE, it becomes clear that standalone PYTHIA, while applicable for theoretical modelling, does not accurately reflect what would be seen in the ALICE detector, especially for low-p_{T} beauty and charm muons.

For charm decays, the consistent normalised yields suggest that charm quark studies in the semi-muonic channel can rely more heavily on standalone simulations, but only up to a point. At low p_{T}, the detailed modelling of AliROOT remains essential to obtain precise results. However, for beauty decays, the more pronounced differences in shape between the two simulations, particularly at higher p_{T}, imply that detector effects must be carefully considered. The higher mass of beauty quarks results in more energetic decay products, and these muons interact significantly with the simulated ALICE detector environment in ways that standalone PYTHIA cannot capture. This makes AliROOT and GEANT crucial for accurate beauty decay analysis, especially at higher p_{T}.

4.5 Differential Cross-Sections

Chapter 5 will focus on comparing the differential cross-sections of heavy-flavour decay muons from PYTHIA 8 simulations and FONLL pQCD calculations with experimental data from ALICE, assessing their agreement and the implications for understanding QCD and heavy-flavour production.

The internal calculation of the total cross-section σ_{gen} (accessed via the `Info::sigmaGen()` function) is utilised to convert PYTHIA 8 normalised yields to differential cross-sections,

which are output in millibarns (mb). The normalised single muon yields ($1/N_{\mathrm{evt}} \times \mathrm{d}N/\mathrm{d}p_{\mathrm{T}}$) are then multiplied by the estimated cross-section (σ_{gen}), to obtain the differential cross-section $\mathrm{d}\sigma/\mathrm{d}p_{\mathrm{T}}$. The conversion can be expressed as:

$$\frac{d\sigma}{dp_{\mathrm{T}}}\ [\mathrm{pb}/(\mathrm{GeV}/c)] = \frac{1}{N}\frac{dN}{dp_{\mathrm{T}}} \times \sigma_{\mathrm{gen}}[\mathrm{mb}] \times 1000. \tag{4.1}$$

The uncertainty in σ_{gen} can be obtained using the `Info::sigmaErr()` function.

CHAPTER 5

Discussion of Results and Conclusion

5.1 Results

This section presents the results of this study and is structured as a comparative analysis of heavy-flavour production in pp collisions, examining the relationship between standalone PYTHIA 8 simulations, FONLL pQCD calculations, and experimental data from the ALICE experiment. The primary objective is to validate PYTHIA 8's ability to predict heavy-flavour production, and evaluating its potential as a reliable simulation framework for heavy-flavour production studies at ALICE.

The present study focuses on the differential cross-sections of single inclusive heavy-flavour decay muons measured in pp collisions, as a function of transverse momentum (p_{T}) at centre-of-mass energies of $\sqrt{s} = 5.02$ TeV and $\sqrt{s} = 13$ TeV. In this study, heavy-flavour particles are identified through their semi-muonic decays using PYTHIA 8 simulations. The analysis includes open charm mesons (D^0, D^+, and D_s^+), charm baryons (Λ_c^+), open beauty mesons (B^0, B^+, and B_s^0), and beauty baryons (Λ_b^0). Quarkonia states such as J/ψ and Υ are explicitly excluded to focus solely on open heavy-flavour production. The experimental data are derived from the results published by ALICE for the LHC15n run period at $\sqrt{s} = 5.02$ TeV [15] and the ongoing analysis of the 2018 data from the LHC18d, LHC18e, LHC18f, LHC18l and LHC18m run periods at $\sqrt{s} = 13$ TeV [16], along with additional data collection periods. The focus is on the transverse momentum range $p_{\mathrm{T}} > 2\,\mathrm{GeV}/c$. This threshold also aligns with the ALICE muon spectrometer

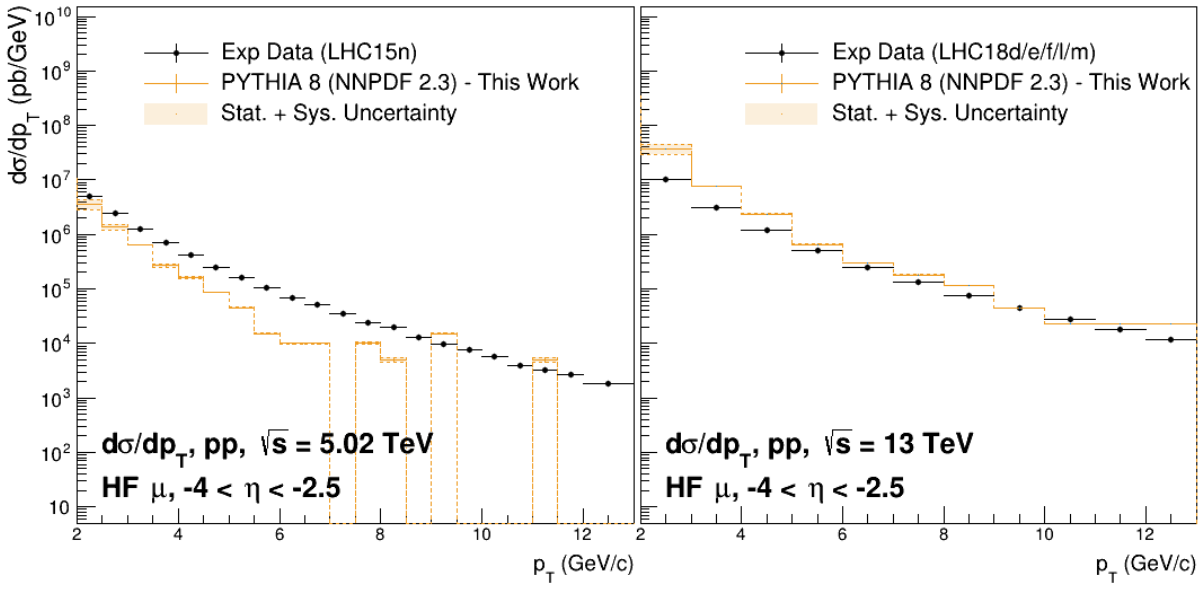


Figure 5.1: Differential cross-section distributions of heavy-flavour muons as a function of transverse momentum at $\sqrt{s} = 5.02$ TeV (left) and $\sqrt{s} = 13$ TeV (right). The black points represent Run 2 experimental data from ALICE from LHC15n [15], and ongoing studies from LHC18d, LHC18e, LHC18f, LHC18l and LHC18m run periods. The data from 2018 only includes statistical uncertainties [16].

triggers and established analysis frameworks to suppress the large background from light-hadron decays (primarily pions and kaons) that dominate at lower momenta, ensuring a cleaner extraction of heavy-flavour muons and a robust comparison to perturbative QCD-based predictions. Hence, the main physics conclusions of this work are drawn in the p_{T} domain of 2-13 GeV/c, where charm and beauty decays dominate the inclusive muon yield. These measurements are compared with standalone PYTHIA 8 simulations, which are configured to match the ALICE detector acceptance and utilise the NNPDF2.3 PDF set. Furthermore, FONLL pQCD calculations, performed with the CTEQ6.6 PDF set, serve as an additional theoretical benchmark for Monte Carlo simulations. The study is limited to FONLL predictions with the CTEQ6.6 PDF set to remain consistent with previous ALICE and LHC heavy-flavour studies. Although FONLL can also be computed using NNPDF30nlo_as0118, CTEQ6.6 is retained to ensure direct comparability with published reference calculations and maintain consistency throughout the analysis. A full exploration of alternative PDFs lies beyond the scope of this work.

Figure 5.1 presents the differential cross-section distributions of inclusive heavy-flavour single muons measured in pp collisions at $\sqrt{s} = 5.02$ TeV (LHC15n) and $\sqrt{s} = 13$ TeV (LHC18d, LHC18e, LHC18f, LHC18l, and LHC18m), compared with standalone PYTHIA 8 simulations (NNPDF2.3). These results provide a general overview of how

well PYTHIA 8 reproduces the measured spectra at the two energies and align with existing studies using PYTHIA 8 for heavy-flavour production [167][168].

The heavy-flavour production cross-section is significantly lower at $\sqrt{s} = 5.02$ TeV than at 13 TeV, despite both simulations being performed with the same configuration and an equal number of events (200 million). The sharp fall-off in high-p_{T} statistics at $\sqrt{s} = 5.02$ TeV can be explained by the combined effects of phase space limitations and the steeply falling p_{T} spectrum in QCD, consistent with previous studies on QCD-driven processes [169][123]. At the lower collision energy, $\sqrt{s} = 5.02$ TeV, the available phase space for hard scatterings is reduced, leading to a lower probability of producing high-p_{T} partons and consequently fewer high-p_{T} heavy-flavour hadrons. This effect is amplified by the gluon parton distribution function (PDF), which is responsible for heavy-quark yields via gluon-gluon fusion. At $\sqrt{s} = 13$ TeV, there is a higher gluon density at small x, which leads to a much higher probability of producing high-p_{T} heavy-flavour hadrons. Additionally, the acceptance of the ALICE muon spectrometer ($-4.0 < \eta < -2.5$) and the kinematic cuts requirements further limit the statistics at high p_{T}, as only a fraction of heavy-flavour hadrons decay into muons that satisfy these selection criteria. The combination of these factors leads to a rapid drop in high-p_{T} statistics at $\sqrt{s} = 5.02$ TeV, whereas the effect is much less pronounced at $\sqrt{s} = 13$ TeV.

At $\sqrt{s} = 5.02$ TeV, PYTHIA 8 underestimates the experimental cross-sections throughout the accessible p_{T} range, showing a steeper decline with increasing p_{T} than observed in the data. In contrast, at $\sqrt{s} = 13$ TeV, PYTHIA 8 overestimates the measured cross-sections in the low- and mid-p_{T} region (2–9 GeV/c). The shapes of the simulated and experimental spectra at 13 TeV become more similar in the higher-p_{T} range (5–9 GeV/c), although the PYTHIA calculations lie above the data. These differences suggest that the standalone PYTHIA 8 configuration, while capturing the overall shape at higher p_{T}, requires additional refinements or tuning to achieve better agreement at both energies (particularly at lower p_{T}). As noted in earlier studies, while FONLL calculations generally align with experimental data within uncertainties, the data often lie at the upper limit of the FONLL predictions, highlighting limitations in capturing the complexity of heavy-flavour production processes, particularly at high transverse momentum and across different energy scales [170].

Despite these discrepancies, Figure 5.1 demonstrates that the heavy-flavour muon spectra exhibit the expected dependence on collision energy, with significantly higher cross-sections observed at $\sqrt{s} = 13$ TeV compared to $\sqrt{s} = 5.02$ TeV. Additionally, the overall shape of the spectra follows the expected trend, reflecting the increase in parton luminosity at higher collision energies. This figure thus serves as a baseline for understanding PYTHIA's default performance before more detailed comparisons are made.

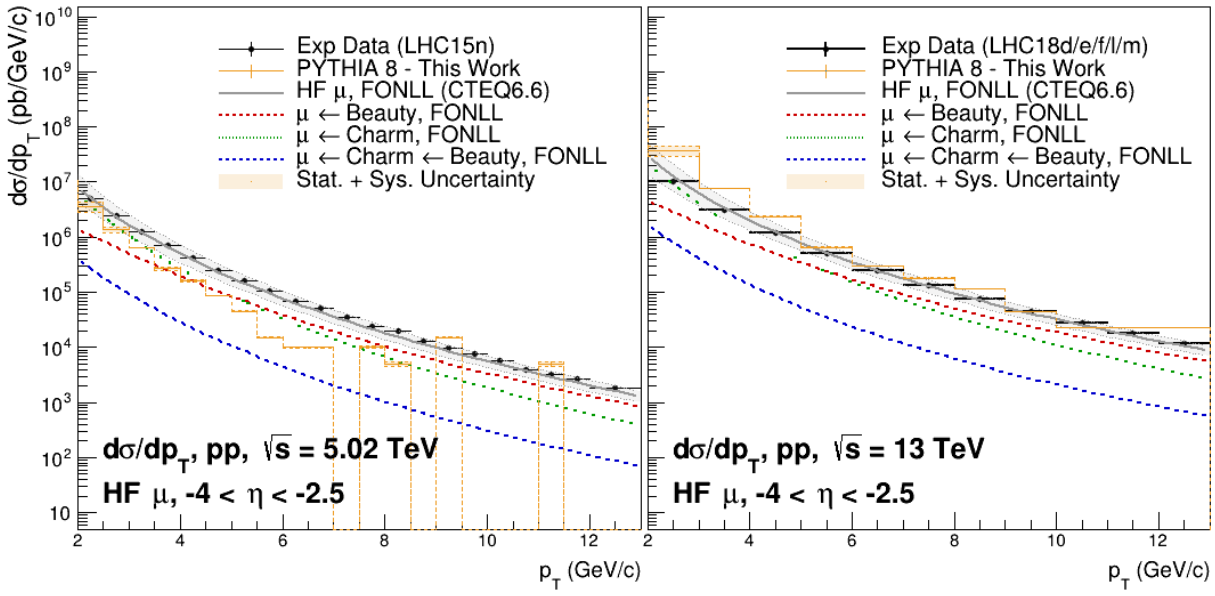


Figure 5.2: The black points and lines represent experimental data from ALICE Run 2, including LHC15n [15], LHC18d, LHC18e, LHC18f, LHC18l and LHC18m run periods (with statistical uncertainties only) [16]. Theoretical predictions from FONLL pQCD calculations using the CTEQ6.6 PDF are shown for various contributions: total heavy-flavour muon production (grey solid line), beauty-to-muon decays (red dashed line), charm-to-muon decays (green dashed line), and beauty-to-charm-to-muon cascade decays (blue dashed line). The figure compares experimental data with FONLL calculations and PYTHIA 8 standalone simulations using NNPDF2.3 (orange histogram). The measurements were performed in the pseudorapidity range $-4 < \eta < -2.5$.

As shown in Figure 5.1, standalone PYTHIA 8 fails to fully capture the differential cross-sections measured at both $\sqrt{s} = 5.02$ TeV and $\sqrt{s} = 13$ TeV, notably underestimating the data at lower energy and overestimating it at higher energy. To gain a deeper understanding of these discrepancies, the standalone PYTHIA 8 simulation predictions were compared with FONLL predictions. Figures 5.2 and 5.3 present the differential heavy-flavour cross-sections, with individual charm and beauty contributions from FONLL (CTEQ6.6), alongside PYTHIA 8's corresponding breakdowns, where the differential cross-sections are summed over the measured kinematic range. By examining the charm and beauty components in both models, it can be determined whether the mismatch arises from specific quark-flavour production or from general theoretical assumptions. This comparison also enables the assessment of how the choice of PDF and other theoretical models could resolve or exacerbate the underestimations and overestimations observed with PYTHIA 8 alone.

In Figures 5.2 and 5.3, both theoretical approaches (PYTHIA 8 standalone simulations and FONLL pQCD calculations) exhibit limitations in accurately predicting the differential cross-sections for the experimental inclusive heavy-flavour single muon productions. Although the FONLL predictions consistently underestimate the experimental cross-sections across different energies, PYTHIA 8's predictions show significant energy dependence: at $\sqrt{s} = 5.02$ TeV, it aligns better with the FONLL predictions in the range $2.0 \leq p_{\mathrm{T}} \leq 3.0$ GeV/c, while at $\sqrt{s} = 13$ TeV, it slightly overestimates the cross-sections in the range $2.0 \leq p_{\mathrm{T}} \leq 5.0$. However, PYTHIA 8 and FONLL are in closer agreement $5.0 \leq p_{\mathrm{T}} \leq 7.0$ (within uncertainties).

In examining the individual contributions of FONLL to the production of muons of heavy flavour in Figure 5.2, expected patterns emerge at both collision energies. At $\sqrt{s} = 5.02$ TeV, the charm-to-muon decay channel dominates the differential cross-section up to $p_{\mathrm{T}} \approx 5$ GeV/c, beyond which the beauty-to-muon contribution becomes dominant, contributing up to 60% of the total cross-section in the high p_{T} region. The beauty-to-charm-to-muon feed-down decay channel maintains the lowest contribution throughout the p_{T} range, contributing less than 10%. Both charm-to-muon and beauty-to-charm-to-muon channels exhibit steeper exponential declines compared to the beauty-to-muon channel, resulting in the increasing relative contribution of beauty-to the total heavy-flavour cross-section at higher p_{T}. At $\sqrt{s} = 13$ TeV, while the overall behaviour of the heavy-flavour contributions remains similar, the crossover point between the charm and beauty contributions shifts to a higher p_{T} by approximately 0.5 GeV/c. This behaviour reflects the underlying QCD processes, where the softer p_{T} spectrum of charm production dominates at lower momenta due to the smaller charm quark mass, whereas the harder spectrum of beauty production, resulting from the higher beauty quark mass, becomes more significant at higher p_{T}. This trend is consistent with results from ALICE in 2012 and 2021 [169][123].

The dominance of charm-to-muon decays at lower transverse momenta (p_{T}), transitioning to beauty-to-muon dominance at higher p_{T}, aligns with theoretical expectations from perturbative Quantum Chromodynamics (pQCD), as heavier beauty quarks produce a harder p_{T} spectrum compared to charm quarks [123]. This transition is quantitatively supported by the observed crossover at $p_{\mathrm{T}} \approx 5$ GeV/c at 5.02 TeV and 5.5 GeV/c at 13 TeV, showing a 10% shift consistent with the predictions of FONLL [170]. Additionally, the slight shift in the crossover point between charm and beauty contributions at different collision energies reflects the energy dependence of parton distribution functions and the increased phase space available at higher energies, confirming trends noted in previous studies [15][167].

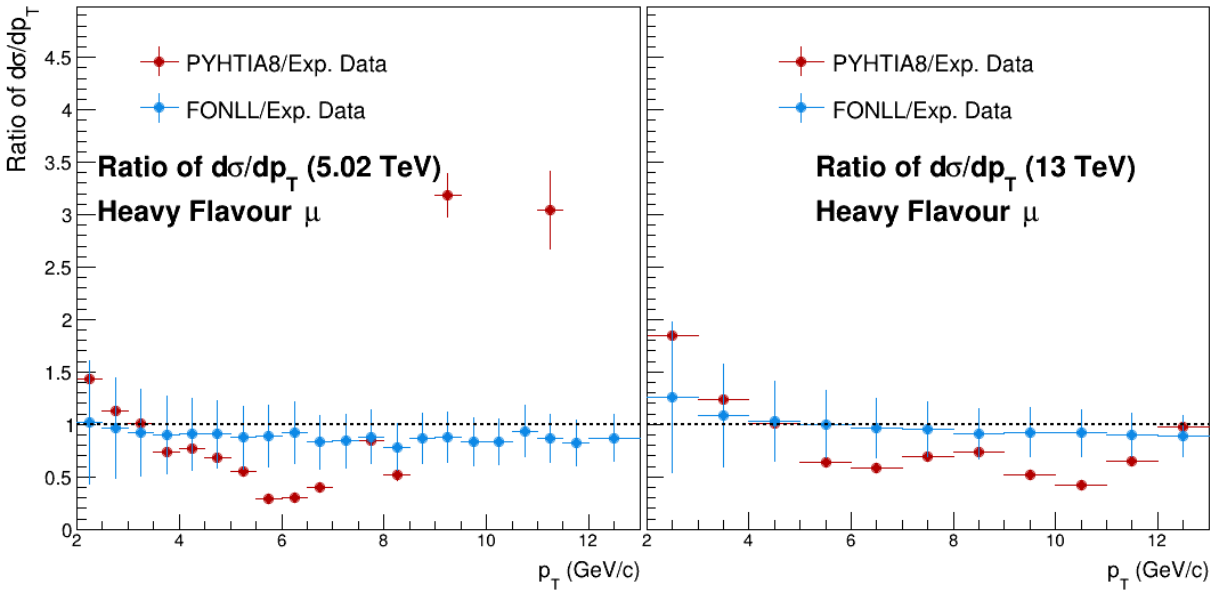


Figure 5.3: Ratios of the differential cross-section $d\sigma/dp_T$ for standalone PYTHIA 8 (NNPDF2.3) to experimental data, and FONLL (CTEQ6.6) to experimental data. The measurements were performed in the pseudorapidity range $-4 < \eta < -2.5$ at $\sqrt{s} = 5.02$ TeV and $\sqrt{s} = 13$ TeV.

At $\sqrt{s} = 5.02$ TeV, the transverse momentum (p_{T}) distributions from standalone PYTHIA 8, FONLL pQCD calculations, and experimental data show broadly consistent shapes, maintaining an exponential decline characteristic of QCD-based processes [26]. It is critical to note that both statistical and systematic uncertainties were considered at $\sqrt{s} = 5.02$ TeV, while only statistical uncertainties were included at $\sqrt{s} = 13$ TeV, potentially contributing to the increase in discrepancies observed at higher energy. As illustrated in Figures 5.1 and 5.2, all distributions exhibit an exponential decline in the inclusive heavy-flavour single muon cross-section with increasing p_{T}. This behaviour is expected from perturbative QCD (pQCD) processes, where the probability of finding high-momentum partons within the proton decreases sharply due to the steeply falling parton distribution functions (PDFs) [157][171]. Additionally, at high p_{T}, kinematic constraints and phase space limitations further suppress particle production, contributing to the overall reduction in the cross-section.

Despite differences in normalisation due to varying treatment of uncertainties, the overall agreement in spectral shape indicates a consistent theoretical description across models and energy scales. Despite the similarity in shape, both PYTHIA 8 and FONLL underestimate the cross-sections relative to the experimental data throughout the p_{T} range. In the region $2.0 \leq p_{\mathrm{T}} \leq 3.0$ GeV/c, PYTHIA 8 and FONLL align within their uncertainties. However, the two models diverge significantly, and standalone PYTHIA 8 underestimates

the cross-section relative to FONLL as p_{T} increases beyond this range. Beyond $p_{\mathrm{T}} = 6.5$ GeV/c, the Monte Carlo simulation predictions (at $\sqrt{s} = 5.02$ TeV) become less statistically reliable, limiting the precision of the conclusions drawn at higher p_{T}. The trend of PYTHIA 8 underestimating FONLL persists in this region. These large discrepancies between the standalone PYTHIA 8 and FONLL predictions suggest the inherent challenges of high theoretical modelling at high p_{T}, and the need for more precise data to better constrain predictions.

At $\sqrt{s} = 13$ TeV, the inclusive heavy-flavour single muon cross-sections from PYTHIA 8, FONLL, and experimental data retain a similar overall shape, characterised by a broad decline with increasing p_{T}. However, compared to the $\sqrt{s} = 5.02$ TeV case, PYTHIA 8 and FONLL show much closer agreement with the experimental data at this higher energy. FONLL predictions are in agreement with experimental data within statistical and systematic uncertainties. Standalone PYTHIA 8 consistently overestimates the cross-sections in the range $2.0 \leq p_{\mathrm{T}} \leq 9.0$ GeV/c, with a relatively significant overestimation around $p_{\mathrm{T}} = 2.0$ GeV/c. At this low p_{T}, PYTHIA 8 predicts approximately 1.9 times the experimental cross-section, highlighting a substantial difference. This suggests that PYTHIA 8's underlying mechanisms for low-p_{T} heavy-flavour production may not fully capture the complexity of the processes involved at these higher energies, possibly overestimating contributions from initial-state effects or the hadronisation process. An extension of this work could involve testing additional PDFs, not considered in this study, to investigate their impact on the predicted cross-sections and assess whether the observed discrepancies persist across different parameterisations of the parton distributions.

PYTHIA 8 exhibits energy-dependent performance variations, underestimating cross-sections at $\sqrt{s} = 5.02$ TeV while overestimating them at $\sqrt{s} = 13$ TeV, indicating limitations in its underlying model assumptions or parameter choices. This distinct behaviour across collision energies also highlights the significant influence of parton distribution function choices (NNPDF2.3 versus CTEQ6.6) on the models' predictions. Although the PYTHIA 8 predictions show closer agreement with the experimental data at higher energy, its contrasting behaviour suggests the need for refinement to achieve consistent performance across different collision energies. These results underscore the challenges in accurately modelling heavy-flavour production, particularly the sensitivity of parton-level processes and hadronisation to both collision energy and PDF choice.

5.2 Conclusion

This study used standalone PYTHIA 8 Monte Carlo simulations to model heavy-flavour production in pp collisions corresponding to LHC Run 2 conditions at ALICE. The primary analysis compared inclusive heavy-flavour single muon cross-sections as a function of

transverse momentum (p_{T}) using standalone PYTHIA 8 Monte Carlo simulations, FONLL pQCD calculations, and the experimental data from the ALICE experiment. The results of the standalone PYTHIA 8 simulation were compared to ALICE experimental data at $\sqrt{s} = 5.02$ TeV (LHC15n) and $\sqrt{s} = 13$ TeV (LHC18d, LHC18e, LHC18f, LHC18l, and LHC18m, merged), to assess the effectiveness of the standalone PYTHIA 8 simulations and determine if standalone PYTHIA 8 can be a reliable tool for predicting heavy-flavour production in future ALICE studies.

To aid the interpretation of the results obtained in the analysis of heavy-flavour muon differential cross-sections, the impact of varying simulation parameters was investigated: centre-of-mass energies, Parton Distribution Functions (PDFs), PYTHIA versions, and accurate detector simulation on the single muon spectra of heavy flavours.

- The comparison of heavy-flavour production cross-sections from PYTHIA, FONLL, and the experimental data highlight the limitations in accurately predicting absolute cross-sections. However, the nature of the deviations varies with collision energy.

- At $\sqrt{s} = 5.02$ TeV, PYTHIA 8 underestimates the experimental cross-sections in the intermediate transverse momentum region ($2.0\mathrm{GeV}/c < p_{\mathrm{T}} < 5.5\mathrm{GeV}/c$), with better agreement at lower and higher p_{T} values. In contrast, at $\sqrt{s} = 13$ TeV, PYTHIA 8 shows significant discrepancies in the regions $2.0\mathrm{GeV}/c < p_{\mathrm{T}} <\sim 4.5\mathrm{GeV}/c$ and above $11\mathrm{GeV}/c$. The agreement in the intermediate region is largely within statistical uncertainties.

- The role of parton distribution functions (PDFs) is also crucial in understanding these discrepancies. Comparisons between NNPDF2.3 used in PYTHIA 8 and CTEQ6.6 used in FONLL reveal systematic differences in cross-section predictions. A crossover occurs around $p_{\mathrm{T}} = 4.0$ GeV/c, where the behaviour of the models diverges, with PYTHIA 8 predicting higher cross-sections at low p_{T} and FONLL producing larger values in the mid-p_{T} range. This highlights the impact of PDF selection on heavy-flavour production, especially at higher energies, where the models become more sensitive to parton-level uncertainties.

- The differences in PYTHIA 8's predictions between $\sqrt{s} = 5.02$ TeV and $\sqrt{s} = 13$ TeV reflect changes in the production patterns of charm and beauty quarks. The observed shift in charm-to-beauty dominance points to higher p_{T} at 13 TeV suggests that production kinematics vary with collision energy. Charm production, due to the lower mass of the charm quark, is more sensitive to these conditions, leading to greater variations at lower p_{T}. Beauty production, characterised by a harder p_{T} spectrum, shows smaller changes in the mid-p_{T} region, but still displays moderate discrepancies at higher p_{T}.

- Detector effects, including trigger efficiency and material interaction variations, are rigourously taken into account in the analysis of the experimental data through AliROOT with GEANT3 simulations. While these effects do not directly influence standalone Monte Carlo simulations like PYTHIA 8 and FONLL, they play a critical role in aligning experimental measurements with theoretical predictions. In particular, at higher p_{T}, accurate detector simulations are essential to properly interpret discrepancies in beauty decay products and ensure robust comparisons between simulations and experimental data.

- In general, PYTHIA 8 faces challenges in accurately predicting heavy-flavour cross-sections, particularly at higher energies and p_{T}. The increasing divergence between PYTHIA and FONLL models at $\sqrt{s} = 13$ TeV suggests that PYTHIA 8 may require further tuning of its hadronisation and initial and final state radiation parameters. The interplay of PDF effects and detector simulations underlines the complexity of modelling heavy-flavour production in high-energy pp collisions. Future work should focus on refining theoretical models, such as PYTHIA 8 and FONLL, and enhancing their integration with detailed detector simulations to improve the predictive accuracy of heavy-flavour cross-sections across the entire p_{T} spectrum.

5.3 Outlook

The modularity and flexibility of PYTHIA make it a powerful tool for simulating various aspects of high-energy pp collisions, especially for heavy-flavour studies. Despite substantial updates between PYTHIA 6 and PYTHIA 8, general agreement is observed for heavy-flavour production, with some discrepancies at low and high p_{T}. This stability is mainly due to the robustness of perturbative QCD (pQCD) models that underpin both versions. However, the differences in the underlying event tunes between PYTHIA 6 and PYTHIA 8, especially due to PYTHIA 8 adding the modelling of multiparton interactions (MPI) and colour reconnection, lead to observable variations in the p_{T} spectra. PYTHIA 8 includes more advanced models, offering a more realistic depiction of the complex environment in high-energy collisions, which is particularly beneficial in improving the accuracy of p_{T} distributions at higher momenta.

The configurability of PYTHIA 8 provides the ability to fine-tune and customise each component of the simulation, from hard scattering to final-state decays. This modular approach, similar to that used in ALICE AliROOT Monte Carlo simulations, can enhance simulation fidelity by allowing researchers to focus on individual stages of the collision. By independently configuring event generation, parton showers, MPI, hadronisation, and decay processes, it is possible to reduce discrepancies with experimental data and improve the overall accuracy of the simulations.

Achieving reliable results from standalone PYTHIA 8 simulations requires careful tuning of each component, particularly in heavy-flavour studies. The flexibility of PYTHIA 8 in terms of parameter tuning is crucial, as it allows researchers to explore various physics scenarios and adjust the simulation to match experimental conditions. It has been noted that the Monte Carlo results depend significantly on the specific tune, both in shape and normalisation. This tunability is vital for systematic studies, enabling the estimation of uncertainties associated with model assumptions, such as factorisation and renormalisation scale variations, heavy quark mass, and uncertainties related to Parton Distribution Functions (PDFs).

Each stage of the simulation impacts the final results in unique ways.

- **Hard Scattering and PDFs:** The initial hard scattering processes are sensitive to the choice of PDFs and the models used to describe hard processes. Variations in these components affect the initial parton kinematics and the overall characteristics of the event.
- **Parton Showers:** Both initial-state radiation (ISR) and final-state radiation (FSR) play a critical role in the evolution of partons prior to hadronisation. Differences in parton shower models can significantly affect the final particle distributions and their agreement with experimental data.
- **Multiple Parton Interactions (MPI):** MPI settings determine the frequency and effects of additional scatterings between partons, contributing to the activity of the underlying event. Variations in MPI configurations can lead to differences in particle multiplicities and overall event structure.
- **Hadronisation and Fragmentation:** The transition from partons to hadrons is modelled through string fragmentation or other mechanisms. The details of this process, including colour reconnection and advanced hadronisation models, significantly impact the yields and kinematics of the final-state particles.
- **Decay Processes:** Accurate modelling of decay processes, including branching ratios and lifetimes, is essential to predict particle spectra, such as those of muons from heavy-flavour decays. Discrepancies in decay modelling can contribute to differences between simulation and experiment.

Future research should focus on further refining PYTHIA 8 calibration techniques, particularly for parameters affecting soft QCD processes and MPI. There is already a precedent for modular configurations in ALICE simulations, where different modules handle fragmentation, hadronisation, and decays. This approach can be adapted to standalone PYTHIA 8 simulations, allowing detailed tuning of each stage of the collision evolution

to improve simulation fidelity. Different event generation modules, such as those for fragmentation or decay, allow for targeted improvements in specific areas of the simulation.

Additionally, the configuration of tunes (like Monash 2013) and MPI settings can significantly influence simulation outcomes. By carefully selecting and tuning these parameters, researchers can reduce discrepancies between PYTHIA 8 and experimental data. Comparing specific processes, such as hard scatterings or parton showers, between PYTHIA 6 and PYTHIA 8 suggests that further tuning could improve agreement with data.

Combining PYTHIA 8 with other frameworks, such as POWHEG, is also valuable for enhancing certain aspects of simulation. By leveraging the strengths of PYTHIA's parton shower with higher-order matrix element calculations provided by POWHEG or MC@NLO, hybrid approaches can improve the accuracy of predictions. This is particularly relevant for processes involving heavy-flavour production, where resummed calculations can better describe the low-p_{T} and forward rapidity regions.

Finally, detector simulations play an essential role, particularly in background estimation and the production of lighter hadron spectra. In the p_{T} range of 1.5-6 GeV/c, standalone PYTHIA 8 spectra show consistent behaviour, suggesting that a constant factor can be applied to account for detector effects and obtain results that closely match those with detailed detector simulations. Accurate trigger simulations, such as those involving Event selection (e.g., low- and high-p_{T}T muons), are essential for reducing discrepancies at low p_{T}, and future work should address inefficiencies in this area.

This study has broad implications for the understanding of QCD in high-energy collisions, particularly in the non-perturbative regime. It validates PYTHIA 8 simulations against ALICE data and compares them with FONLL predictions, highlighting vital areas where Monte Carlo generators need refinement. Heavy-flavour production remains crucial in testing QCD, especially as LHC experiments push to higher energies. The insights gained here contribute directly to improving the precision of theoretical models.

Heavy-flavour studies are essential for constraining Standard Model parameters, such as the strong coupling constant and heavy-quark masses. The results of this study contribute to advances in particle physics and related fields, including heavy-ion collisions and astroparticle physics. The methodologies developed—particularly for simulating and analysing differential cross-sections—can be applied to a wide range of other areas that require precise modelling of complex particle interactions.

The main contributions of this thesis lie in its comprehensive analysis of heavy-flavour production using PYTHIA 8 and FONLL and its exploration of crucial discrepancies in the low-p_{T} region. This work provides a valuable framework for improving simulation

fidelity and advancing the understanding of QCD.

Looking ahead, the upgraded ALICE detector and the forthcoming LHC Run 3 data will provide unprecedented opportunities for more precise studies of heavy flavours. Advances in machine learning and computational techniques will further enhance the accuracy of simulations. This work sets the stage for future investigations that will continue to test QCD and refine fundamental physics models at the highest energy scales.

Bibliography

[1] Wikipedia contributors. Standard model of elementary particles. https://en.wikipedia.org/wiki/File:Standard_Model_of_Elementary_Particles.svg, 2024. Accessed: 14 June 2024.

[2] R. D. Ball, V. Bertone, S. Carrazza, and et al. Parton distributions from high-precision collider data. *European Physical Journal C*, 77(663), October 2017. doi: 10.1140/epjc/s10052-017-5199-5. URL https://doi.org/10.1140/epjc/s10052-017-5199-5.

[3] CERN. CERN's accelerator complex. https://www.home.cern/science/accelerators/accelerator-complex, 2023. Accessed: 2023-12-01.

[4] Ewa Lopienska. The cern accelerator complex, layout in 2022. https://cds.cern.ch/record/2800984, 2022. Accessed on 2023-12-01.

[5] CERN. Experiments. https://press.cern/science/experiments, 2023. Accessed on 2023-12-01.

[6] L. Valencia Palomo. The alice experiment upgrades for lhc run 3 and beyond: contributions from mexican groups. In *Journal of Physics: Conference Series*, volume 912, page 012023, 2017.

[7] Piotr Nowakowski, Przemysław Rokita, and Łukasz Graczykowski. Distributed simulation and visualization of the alice detector magnetic field. *Computer Physics Communications*, 271:108206, February 2022. doi: 10.1016/j.cpc.2021.108206.

[8] ALICE Collaboration. The ALICE experiment at the CERN LHC. *Journal of Instrumentation*, 3, 2008.

[9] P. Riedler, G. Anelli, F. Antinori, A. Boccardi, M. Burns, I.A. Cali, M. Campbell, M. Caselle, P. Chochula, M. Cinausero, A. Dalessandro, R. Dima, R. Dinapoli, D. Elia, D. Fabris, R.A. Fini, E. Fioretto, F. Formenti, S. Kapusta, A. Kluge, and T. Virgili. Recent test results of the alice silicon pixel detector. *Nuclear Instruments and Methods in Physics Research Section A: Accelerators, Spectrometers, Detectors and Associated Equipment*, 549(1-3):65–69, September 2005. doi: 10.1016/j.nima.2005.04.027. URL https://doi.org/10.1016/j.nima.2005.04.027.

[10] V. V. Ivanov, V. N. Nikulin, E. V. Roshchin, V. M. Samsonov, and A. V. Khanzadeev. The Front-End electronics for the tracking system of the ALICE muon spectrometer. *Instruments and Experimental Techniques*, 62(6):750–763, November 2019. ISSN 1608-3180. doi: 10.1134/S0020441219060071.

[11] Livia Terlizzi. Upgrade and commissioning of the alice muon spectrometer, 2022. URL https://arxiv.org/abs/2210.12431.

[12] F. Carminati and A. Morsch. Simulation in alice. In *Proceedings of Computing in High Energy and Nuclear Physics*, page 1, La Jolla, California, March 2003. ALICE Offline Project. CERN, 1211 Geneva 23, Switzerland.

[13] C. Bierlich, S. Chakraborty, N. Desai, L. Gellersen, I. Helenius, P. Ilten, L. Lönnblad, S. Mrenna, S. Prestel, C. T. Preuss, T. Sjöstrand, P. Skands, M. Utheim, and R. Verheyen. A comprehensive guide to the physics and usage of pythia 8.3. *SciPost Physics Codebases*, 2022. doi: 10.48550/arXiv.2203.11601.

[14] Stefan Höche. Introduction to parton-shower event generators. In *Theoretical Advanced Study Institute in Elementary Particle Physics: Journeys Through the Precision Frontier: Amplitudes for Colliders*, pages 235–295. World Scientific, 2015. doi: 10.1142/9789814678766_0005.

[15] S. Acharya, D. Adamová, et al. Production of muons from heavy-flavour hadron decays in pp collisions at $\sqrt{s} = 5.02$ tev. *Journal of High Energy Physics*, 2019: 8, 09 2019. doi: 10.1007/JHEP09(2019)008. URL https://doi.org/10.1007/JHEP09(2019)008. Received: 24 May 2019, Accepted: 15 August 2019, Published: 02 September 2019.

[16] B. Naik, M.S. Islam, and T.J. Shaba. Inclusive and multiplicity-dependent production of muons from heavy-flavour hadron decays in pp and p-pb collisions at $\sqrt{s} = 13$ tev. ALICE Muon Week 2023, Private Communication, 6 2023. Presentation at ALICE Muon Week, June 5-9, 2023, Cala Serena Village, Maracalagonis (Cagliari), Italy. URL: https://indico.cern.ch/event/1264730/.

[17] ALICE Collaboration. System-size dependence of the charged-particle pseudorapidity density at $\sqrt{s_{\mathrm{NN}}} = 5.02$ tev for pp, p–pb, and pb–pb collisions. *Physics Letters B*, 845:137730, 2023. doi: 10.1016/j.physletb.2023.137730. URL https://www.sciencedirect.com/science/article/pii/S0370269323000643. Under a Creative Commons license.

[18] ALICE Collaboration. A ten-year journey through the quark–gluon plasma and beyond. CERN feature article, 2022. URL https://home.cern/news/series/feature/ten-year-journey-through-quark-gluon-plasma-and-beyond.

[19] M. Harrison, T. Ludlam, and S. Ozaki. Rhic project overview. *Nuclear Instruments and Methods in Physics Research Section A: Accelerators, Spectrometers, Detectors and Associated Equipment*, 499(2–3):235–244, March 2003. doi: 10.1016/S0168-9002(02)01937-X. URL https://doi.org/10.1016/S0168-9002(02)01937-X.

[20] Brookhaven National Laboratory. Rhic accelerators. https://www.bnl.gov/rhic/complex.php, 2024. Accessed: 2024-11-27.

[21] Robert P. Crease. Recombinant science: The birth of the relativistic heavy ion collider (rhic). *Historical Studies in the Natural Sciences*, 38(4):535–568, November 2008. doi: 10.1525/hsns.2008.38.4.535. URL https://doi.org/10.1525/hsns.2008.38.4.535.

[22] Ulrich Heinz. The quark-gluon plasma at rhic. *Nuclear Physics A*, 721:C30–C39, June 2003. doi: 10.1016/S0375-9474(03)01014-5. URL https://doi.org/10.1016/S0375-9474(03)01014-5.

[23] Ulrich Heinz and Raimond Snellings. Collective flow and viscosity in relativistic heavy-ion collisions. *Annual Review of Nuclear and Particle Science*, 63:123–151, 2013. doi: 10.1146/annurev-nucl-102212-170540.

[24] Richard P. Feynman. Very high-energy collisions of hadrons. *Physical Review Letters*, 23(24):1415–1417, 1969. doi: 10.1103/PhysRevLett.23.1415.

[25] Taesoo Song and Gabriele Coci. Prerequisites for heavy quark coalescence in heavy-ion collisions. *Nuclear Physics A*, 1028:122539, 2022. doi: 10.1016/j.nuclphysa.2022.122539. URL https://www.sciencedirect.com/science/article/abs/pii/S0375947422001592.

[26] Matteo Cacciari, Mario Greco, and Paolo Nason. The pt spectrum in heavy-flavour hadroproduction. *Journal of High Energy Physics*, 1998(05):007, jun 1998. doi: 10.1088/1126-6708/1998/05/007. URL https://dx.doi.org/10.1088/1126-6708/1998/05/007.

[27] ALICE Collaboration, S. Acharya, D. Adamová, et al. The alice experiment: a journey through qcd. *European Physical Journal C*, 84:813, 2024. doi: 10.1140/epjc/s10052-024-12935-y. URL https://doi.org/10.1140/epjc/s10052-024-12935-y. Published 14 August 2024, Received 20 January 2023, Accepted 20 May 2024.

[28] Matteo Cacciari et al. Theoretical predictions for charm and bottom production at the lhc. *Journal of High Energy Physics*, 2012(10):137, 2012.

[29] Steven Weinberg. *The Quantum Theory of Fields*. Cambridge University Press, Cambridge, 1995. ISBN 978-0-521-55001-7.

[30] S. L. Glashow. Partial-symmetries of weak interactions. *Nuclear Physics*, 22:579–588, 1961. doi: 10.1016/0029-5582(61)90469-2.

[31] Herbert M. Reese. The zeeman effect. *Science*, 12(295):293–297, August 1900. URL https://www.jstor.org/stable/1628310.

[32] A J Kox. The discovery of the electron: Ii. the zeeman effect. *European Journal of Physics*, 18(3):139, may 1997. doi: 10.1088/0143-0807/18/3/003. URL https://dx.doi.org/10.1088/0143-0807/18/3/003.

[33] David J. Griffiths. *Introduction to Elementary Particles*. Wiley-VCH, Weinheim, 2008. ISBN 978-3-527-40601-2.

[34] J.J. Sakurai and Jim Napolitano. *Modern Quantum Mechanics*. Cambridge University Press, Cambridge, 2017. ISBN 978-1-107-15252-5.

[35] P.A.M. Dirac. The quantum theory of the electron. *Proceedings of the Royal Society A*, 117(778):610–624, 1928. doi: 10.1098/rspa.1928.0023.

[36] Satyendra Nath Bose. Planck's law and the hypothesis of light quanta. *Zeitschrift für Physik*, 26:178–181, 1924. doi: 10.1007/BF01327326.

[37] Michael E. Peskin and Daniel V. Schroeder. *An Introduction to Quantum Field Theory*. Addison-Wesley, Reading, Massachusetts, 1995. ISBN 978-0-201-50397-5.

[38] Murray Gell-Mann. A schematic model of baryons and mesons. *Physics Letters*, 8 (3):214–215, 1964. doi: 10.1016/S0031-9163(64)92001-3.

[39] Y. Nambu and G. Jona-Lasinio. Dynamical model of elementary particles based on an analogy with superconductivity. i. *Physical Review*, 122:345–358, 1961. doi: 10.1103/PhysRev.122.345.

[40] K.G. Wilson. The renormalization group and strong interactions. *Physical Review D*, 3(8):1818–1846, 1970. doi: 10.1103/PhysRevD.3.1818.

[41] P.W. Higgs. Broken symmetries and the masses of gauge bosons. *Physical Review Letters*, 13(16):508–509, 1964. doi: 10.1103/PhysRevLett.13.508.

[42] Abdus Salam. Weak and electromagnetic interactions. *Conf. Proc. C*, 680519:367–377, 1968.

[43] Steven Weinberg. *Gravitation and Cosmology: Principles and Applications of the General Theory of Relativity*. John Wiley & Sons, New York, 1972. ISBN 978-0-471-92567-5.

[44] John D. Jackson. *Classical Electrodynamics*. Wiley, New York, 1999. ISBN 978-0-471-30932-1.

[45] P.A.M. Dirac. Quantised singularities in the electromagnetic field. *Proceedings of the Royal Society A*, 133(821):60–72, 1931. doi: 10.1098/rspa.1931.0130.

[46] J.C. Maxwell. A dynamical theory of the electromagnetic field. *Philosophical Transactions of the Royal Society of London*, 155:459–512, 1865. doi: 10.1098/rstl.1865.0008.

[47] J. Chadwick. Possible existence of a neutron. *Nature*, 129(3252):312, 1932. doi: 10.1038/129312a0.

[48] C.D. Anderson and S.H. Neddermeyer. Cloud chamber observations of cosmic rays at 4300 meters elevation and near sea-level. *Physical Review*, 50(4):263–271, 1936. doi: 10.1103/PhysRev.50.263.

[49] K. Winter. *Neutrino Physics*. Cambridge University Press, Cambridge, 2000. ISBN 978-0-521-65337-4.

[50] Enrico Fermi. Tentativo di una teoria dei raggi β. *Nuovo Cimento*, 11:1–19, 1934. doi: 10.1007/BF02959820.

[51] Kan Chang Wang. A suggestion on the detection of the neutrino. *Phys. Rev.*, 61: 97–97, Jan 1942. doi: 10.1103/PhysRev.61.97. URL https://link.aps.org/doi/10.1103/PhysRev.61.97.

[52] Carl D. Anderson. The positive electron. *Physical Review*, 43:491–494, 1933. doi: 10.1103/PhysRev.43.491.

[53] Erwin Schrödinger. An undulatory theory of the mechanics of atoms and molecules. *Physical Review*, 28(6):1049–1070, 1926. doi: 10.1103/PhysRev.28.1049.

[54] Clyde L. Cowan, Frederick Reines, F. B. Harrison, H. W. Kruse, and A. D. McGuire. Detection of the free neutrino: A confirmation. *Science*, 124(3212):103–104, 1956. doi: 10.1126/science.124.3212.103.

[55] Nobel Prize Committee. The nobel prize in physics 1995. *NobelPrize.org*, 1995. URL: https://www.nobelprize.org/prizes/physics/1995/summary/.

[56] Frederick Reines, M. F. Crouch, T. L. Jenkins, W. R. Kropp, J. S. Mulholland, M. H. Wyman, C. B. Bratton, L. D. Foster, W. Gajewski, W. K. Hensley, and K. A. Rielage. Evidence for high-energy cosmic-ray neutrino interactions. *Physical Review Letters*, 15(9):429–433, 1965. doi: 10.1103/PhysRevLett.15.429.

[57] G. Aad et al. Observation of a new particle in the search for the standard model higgs boson with the atlas detector at the lhc. *Physics Letters B*, 716:1–29, 2012.

[58] Emilio Segrè, Owen Chamberlain, Clyde Wiegand, and Thomas Ypsilantis. Observation of antiprotons. *Physical Review*, 100(3):947, 1955. doi: 10.1103/PhysRev.100.947.

[59] Bruce Cork, Glen Lambertson, Orest Piccioni, and William A. Wenzel. Antineutrons produced from antiprotons in charge-exchange collisions. *Physical Review*, 104(5):1193, 1956. doi: 10.1103/PhysRev.104.1193.

[60] Frederick Reines and Clyde L. Cowan. Detection of the free neutrino. *Physical Review*, 92(3):830, 1953. doi: 10.1103/PhysRev.92.830.

[61] Andrei D. Sakharov. Violation of cp invariance, c asymmetry, and baryon asymmetry of the universe. *JETP Letters*, 5(24):24–27, 1967. URL http://www.jetpletters.ac.ru/ps/1643/article_25089.shtml.

[62] George Zweig. An su(3) model for strong interaction symmetry and its breaking. *CERN Report No. 8419/TH.412*, 1964.

[63] H. Yukawa. On the interaction of elementary particles i. *Proceedings of the Physico-Mathematical Society of Japan*, 17:48–57, 1935.

[64] S.-K. Choi, S. L. Olsen, I. Adachi, H. Aihara, V. Aulchenko, T. Aushev, T. Aziz, A. M. Bakich, V. Balagura, I. Bedny, U. Bitenc, A. Bondar, A. Bozek, M. Bračko, J. Brodzicka, T. E. Browder, P. Chang, Y. Chao, A. Chen, K.-F. Chen, W. T. Chen, B. G. Cheon, R. Chistov, Y. Choi, J. Dalseno, M. Danilov, M. Dash, S. Eidelman, N. Gabyshev, B. Golob, J. Haba, T. Hara, K. Hayasaka, H. Hayashii, M. Hazumi, D. Heffernan, Y. Hoshi, W.-S. Hou, H. J. Hyun, T. Iijima, K. Inami, A. Ishikawa, H. Ishino, R. Itoh, M. Iwasaki, Y. Iwasaki, D. H. Kah, J. H. Kang, N. Katayama,

H. Kawai, T. Kawasaki, H. Kichimi, H. O. Kim, S. K. Kim, Y. J. Kim, K. Kinoshita, P. Križan, P. Krokovny, R. Kumar, C. C. Kuo, A. Kuzmin, Y.-J. Kwon, J. S. Lange, J. S. Lee, M. J. Lee, S. E. Lee, T. Lesiak, A. Limosani, S.-W. Lin, Y. Liu, D. Liventsev, F. Mandl, A. Matyja, S. McOnie, T. Medvedeva, W. Mitaroff, K. Miyabayashi, H. Miyake, H. Miyata, Y. Miyazaki, R. Mizuk, G. R. Moloney, E. Nakano, M. Nakao, S. Nishida, O. Nitoh, T. Nozaki, S. Ogawa, T. Ohshima, S. Okuno, H. Ozaki, P. Pakhlov, G. Pakhlova, C. W. Park, H. Park, L. S. Peak, R. Pestotnik, L. E. Piilonen, H. Sahoo, Y. Sakai, O. Schneider, A. J. Schwartz, K. Senyo, M. Shapkin, C. P. Shen, H. Shibuya, B. Shwartz, J. B. Singh, A. Somov, S. Stanič, M. Starič, T. Sumiyoshi, S. Y. Suzuki, F. Takasaki, K. Tamai, M. Tanaka, Y. Teramoto, I. Tikhomirov, S. Uehara, T. Uglov, Y. Unno, S. Uno, P. Urquijo, G. Varner, K. Vervink, S. Villa, C. H. Wang, M.-Z. Wang, P. Wang, X. L. Wang, Y. Watanabe, R. Wedd, E. Won, B. D. Yabsley, Y. Yamashita, C. Z. Yuan, Z. P. Zhang, V. Zhulanov, A. Zupanc, and O. Zyukova. Observation of a resonancelike structure in the $\pi^{+-}\psi'$ mass distribution in exclusive $b \to k\pi^{+-}\psi'$ decays. *Phys. Rev. Lett.*, 100:142001, Apr 2008. doi: 10.1103/PhysRevLett.100.142001. URL https://link.aps.org/doi/10.1103/PhysRevLett.100.142001.

[65] R. et al. Aaij. Observation of the resonant character of the $z(4430)^-$ state. *Physical Review Letters*, 112(22):222002, 2014. doi: 10.1103/PhysRevLett.112.222002.

[66] R. et al. Aaij. Observation of j/ψ resonances consistent with pentaquark states in $\lambda_b^0 \to j/\psi k^- p$ decays. *Physical Review Letters*, 115(7):072001, 2015. doi: 10.1103/PhysRevLett.115.072001.

[67] Ernest Rutherford. Lxxix. the scattering of α and β particles by matter and the structure of the atom. *Philosophical Magazine Series 6*, 21(125):669–688, 1911. doi: 10.1080/14786440508637080.

[68] W. Heisenberg. On the structure of atomic nuclei. i. *Zeitschrift für Physik*, 77:1–11, 1932. doi: 10.1007/BF01342433.

[69] John M. Blatt and Victor F. Weisskopf. *Theoretical Nuclear Physics*. Springer, New York, NY, 1979. ISBN 978-1-4612-9961-5. doi: 10.1007/978-1-4612-9959-2. Softcover ISBN: 978-1-4612-9961-5, eBook ISBN: 978-1-4612-9959-2.

[70] M. Taketani, S. Nakamura, and M. Sasaki. The meson theory of nuclear forces. i. *Progress of Theoretical Physics Supplement*, 39:1–111, 1968. doi: 10.1143/PTPS.39.1.

[71] C. D. Anderson and S. H. Neddermeyer. Cloud chamber observations of cosmic rays at 4300 meters elevation and near sea-level. *Physical Review*, 50:263–271, 1936. doi: 10.1103/PhysRev.50.263.

[72] C. M. G. Lattes, H. Muirhead, G. P. S. Occhialini, and C. F. Powell. Processes involving charged mesons. *Nature*, 159:694–697, 1947. doi: 10.1038/159694a0.

[73] H. Fritzsch, M. Gell-Mann, and H. Leutwyler. Advantages of the color octet gluon picture. *Physics Letters B*, 47:365–368, 1973. doi: 10.1016/0370-2693(73)90625-4.

[74] E. D. et al. Bloom. High-energy inelastic e-p scattering at 6° and 10°. *Physical Review Letters*, 23:930–934, 1969. doi: 10.1103/PhysRevLett.23.930.

[75] G. D. Rochester and C. C. Butler. Evidence for the existence of new unstable elementary particles. *Nature*, 160:855–857, 1947. doi: 10.1038/160855a0.

[76] B. J. Bjørken and S. L. Glashow. Elementary particles and SU(4). *Physics Letters*, 11(3):255–257, August 1964. doi: 10.1016/0031-9163(64)90433-0. Received 19 June 1964.

[77] S. L. Glashow, J. Iliopoulos, and L. Maiani. Weak interactions with lepton-hadron symmetry. *Physical Review D*, 2:1285–1292, 1970. doi: 10.1103/PhysRevD.2.1285.

[78] J. J. et al. Aubert. Experimental observation of a heavy particle j. *Physical Review Letters*, 33:1404–1406, 1974. doi: 10.1103/PhysRevLett.33.1404.

[79] J. E. et al. Augustin. Discovery of a narrow resonance in e^+e^- annihilation. *Physical Review Letters*, 33:1406–1408, 1974. doi: 10.1103/PhysRevLett.33.1406.

[80] M. Kobayashi and T. Maskawa. Cp violation in the renormalizable theory of weak interaction. *Progress of Theoretical Physics*, 49:652–657, 1973. doi: 10.1143/PTP.49.652.

[81] H. Harari. A new quark model for hadrons. *Physics Letters B*, 57(3):265–269, July 1975. doi: 10.1016/0370-2693(75)90072-6.

[82] S. W. et al. Herb. Observation of a dimuon resonance at 9.5 gev in 400-gev proton-nucleus collisions. *Physical Review Letters*, 39:252–255, 1977. doi: 10.1103/PhysRevLett.39.252.

[83] F. et al. Abe. Observation of top quark production in $\bar{p}p$ collisions. *Physical Review Letters*, 74:2626–2631, 1995. doi: 10.1103/PhysRevLett.74.2626.

[84] D.J. Gross and F. Wilczek. Asymptotically free gauge theories. i. *Physical Review D*, 8(10):3633–3652, 1973. doi: 10.1103/PhysRevD.8.3633.

[85] F. Wilczek. Problem of strong p and t invariance in the presence of instantons. *Physical Review Letters*, 40:279, 1978. doi: 10.1103/PhysRevLett.40.279.

[86] H.D. Politzer. Reliable perturbative results for strong interactions? *Physical Review Letters*, 30(26):1346–1349, 1973. doi: 10.1103/PhysRevLett.30.1346.

[87] Kenneth G Wilson. Confinement of quarks. *Physical Review D*, 10(8):2445, 1974.

[88] John N. Bahcall. *Neutrino Astrophysics*. Cambridge University Press, Cambridge, 1989. ISBN 978-0-521-37975-4.

[89] Frank Close. *The New Cosmic Onion: Quarks and the Nature of the Universe*. CRC Press, Boca Raton, 2007. ISBN 978-1-4200-1016-1.

[90] David J. Gross and Frank Wilczek. Ultraviolet behavior of non-abelian gauge theories. *Physical Review Letters*, 30:1343–1346, 1973. doi: 10.1103/PhysRevLett.30.1343.

[91] Chen Ning Yang and Robert L. Mills. Conservation of isotopic spin and isotopic gauge invariance. *Physical Review*, 96:191–195, 1954. doi: 10.1103/PhysRev.96.191.

[92] Howard Georgi. *Lie Algebras In Particle Physics: from Isospin To Unified Theories*. Westview Press, Boulder, CO, 2nd edition, 1999. ISBN 978-0-7382-0233-2.

[93] B. W. Harris and J. Smith. Heavy quark correlations in deep inelastic scattering. *Nuclear Physics B*, 452(1-2):109–144, 1995.

[94] Richard P. Feynman. Very high-energy collisions of hadrons. *Physical Review Letters*, 23(24):1415, 1969.

[95] J.C. Collins, D.E. Soper, and G. Sterman. Factorization of hard processes in qcd. In A.H. Mueller, editor, *Perturbative QCD*, volume 5 of *Advanced Series on Directions in High Energy Physics*, pages 1–91. World Scientific, 1989.

[96] STEVEN D. BASS. The proton spin puzzle: Where are we today? *Modern Physics Letters A*, 24(14):1087–1101, 2009. doi: 10.1142/S0217732309031041.

[97] Y.L. Dokshitzer. Calculation of the structure functions for deep inelastic scattering and e+e- annihilation by perturbation theory in quantum chromodynamics. *Sov. Phys. JETP*, 46:641–653, 1977.

[98] R. Keith Ellis, W. James Stirling, and Bryan R. Webber. *QCD and Collider Physics*. Cambridge University Press, Cambridge, UK, 2011.

[99] R.D. Field. The underlying event in hard scattering processes. *Annual Review of Nuclear and Particle Science*, 62:453–484, 2012.

[100] J. D. Bjorken. Asymptotic sum rules at infinite momentum. *Physical Review*, 179: 1547–1553, 1969.

[101] NNPDF Collaboration. High precision global determinations of parton distributions. https://nnpdf.mi.infn.it/reference/, November 2023. Accessed: 17 November 2023.

[102] T. Sjostrand. Introduction to the lund string model. *Nuclear Physics B: Proceedings Supplements*, 157:329–339, 2006.

[103] B. Andersson, G. Gustafson, G. Ingelman, and T. Sjöstrand. Parton fragmentation and string dynamics. *Physics Reports*, 97(2):31–145, 1983. ISSN 0370-1573. doi: https://doi.org/10.1016/0370-1573(83)90080-7. URL https://www.sciencedirect.com/science/article/pii/0370157383900807.

[104] T. Sjostrand et al. Multiple interactions in high-energy hadron collisions. *Physics Letters B*, 651:124–130, 2004.

[105] ATLAS Collaboration. Pile-up mitigation at atlas. *ATLAS-CONF-2013-083*, 2013.

[106] Jacob J. Ethier and Emanuele R. Nocera. Parton distributions in nucleons and nuclei. *Annual Review of Nuclear and Particle Science*, 70:43–76, October 2020. doi: 10.1146/annurev-nucl-011720-042725. First published as a Review in Advance on June 02, 2020.

[107] Michał Czakon, Paul Fiedler, and Alexander Mitov. Total top-quark pair-production cross section at hadron colliders through o(α_s^4). *Physical Review Letters*, 110(25):252004, 2013.

[108] Jonathan M Butterworth, Stefano Carrazza, Amanda M Cooper-Sarkar, J Feltesse, Stefano Forte, Alberto Guffanti, Joey Huston, Jose Ignacio Latorre, Juan Rojo, and Maria Ubiali. Pdf4lhc recommendations for lhc run ii. *Journal of Physics G: Nuclear and Particle Physics*, 43(2):023001, 2016.

[109] Alexandre Deur, Stanley J Brodsky, and Guy F de Téramond. The spin structure of the nucleon. *Reports on Progress in Physics*, 82(7):076201, Jul 2019. doi: 10.1088/1361-6633/ab0b8f. Epub 2019 Feb 28.

[110] Zebo Tang, Wang-Mei Zha, and Yi-Fei Zhang. An experimental review of open heavy flavor and quarkonium production at rhic. *Nuclear Science and Techniques*, 31:81, 2020. doi: 10.1007/s41365-020-00785-8.

[111] O.S. Bruning, P. Collier, P. Lebrun, S. Myers, R. Ostojic, J. Poole, and P. Proudlock. Lhc design report vol. i: The lhc main ring. *CERN*, CERN-2004-003-V-1, 2004.

[112] Helmut Wiedemann. *Particle Accelerator Physics*. Springer, 2015. doi: 10.1007/978-3-319-18317-6.

[113] M. M. Block. Elastic and total cross sections in pp and $\bar{p}p$ collisions. *Physical Review D*, 86:051504, 2012.

[114] A. Djouadi. Production and decay of the higgs bosons. *Physics Reports*, 457:1–216, 2008.

[115] S.J. Brodsky et al. Intrinsic heavy quark distributions in qcd. *Physics Reports*, 522: 239–255, 2015.

[116] A Andronic et al. Heavy-flavour and quarkonium production in the lhc era: from proton–proton to heavy-ion collisions. *The European Physical Journal C*, 76(3):107, 2016.

[117] Aneesh V. Manohar and Mark B. Wise. *Heavy Quark Physics*, volume 10 of *Cambridge Monographs on Particle Physics, Nuclear Physics, and Cosmology*. Cambridge University Press, Cambridge, UK, 2000. ISBN 978-0-521-52996-7. doi: 10.1017/CBO9780511529351. URL https://doi.org/10.1017/CBO9780511529351. Online publication date: October 2009, Print publication year: 2000.

[118] PL McGaughey, JM Moss, JC Peng, et al. Heavy-quark production in pp and p a collisions at s= 800 gev. *International Journal of Modern Physics A*, 10(20): 2999–3010, 1995.

[119] Paolo Nason, Sally Dawson, and R Keith Ellis. The total cross-section for the production of heavy quarks in hadronic collisions. *Nuclear Physics B*, 303(4):607–633, 1989.

[120] Yuri L. Dokshitzer and Dmitri E. Kharzeev. Heavy quark colorimetry of qcd matter. *Physics Letters B*, 519:199–206, 2001. doi: 10.1016/S0370-2693(01)01130-3.

[121] A. A. P. Suaide. Open heavy flavor production at RHIC. *J. Phys. G*, 34:S369–376, 2007. doi: 10.1088/0954-3899/34/8/S24.

[122] R. Vogt. The status of open heavy flavor production at rhic. *Nuclear Physics B - Proceedings Supplements*, 214(1):129–133, 2011. ISSN 0920-5632. doi: https://doi.org/10.1016/j.nuclphysbps.2011.03.072. URL https://www.sciencedirect.com/science/article/pii/S092056321100140X. Proceedings of the Workshop "Three Days of Quarkonium Production in Proton-Proton and Proton-Nucleus Collisions".

[123] S. Acharya et al. Measurement of charm and beauty production at midrapidity in pp collisions at $\sqrt{s} = 5.02$ tev. *Journal of High Energy Physics*, 2021:159, 2021. doi: 10.1007/JHEP05(2021)159.

[124] A. Adare et al. Heavy quark production in p + p and energy loss and flow of heavy quarks in au + au collisions at $\sqrt{s_{NN}}$ = 200 gev. *Physical Review C*, 84:044905, 2011. doi: 10.1103/PhysRevC.84.044905.

[125] M. Cacciari, M. Greco, and P. Nason. Qcd analysis of hadronic z decays. *Nuclear Physics B*, 542(1-2):515–525, 1998.

[126] K. Aamodt et al. Charged-particle multiplicity density at mid-rapidity in central pb–pb collisions at $\sqrt{s_{NN}}$ = 2.76 tev. *Physical Review Letters*, 105(25):252301, 2010.

[127] ALICE Collaboration. Technical design report on forward detectors: Fmd, t0 and v0. Technical Report CERN-LHCC-2004-025, ALICE-TDR-011, CERN, September 2004.

[128] ALICE Collaboration. Technical Design Report of the Transition Radiation Detector. Technical Report ALICE TDR 9, CERN/LHCC, October 2001. CERN/LHCC 2001-021.

[129] V. I. Man'ko, W. Klempt, L. Leistam, J. De Groot, and Jürgen Schükraft. Alice photon spectrometer (phos): Technical design report. Technical Report CERN-LHCC-99-004 ; ALICE-TDR-2, CERN, Geneva, 1999. URL https://doi.org/10.5281/zenodo.47494.

[130] ALICE Collaboration and Beole, S. ALICE technical design report: Detector for high momentum pid. Technical Report CERN-LHCC-98-19, CERN, 1998. URL http://cds.cern.ch/record/331437. Experiments: CERN-LHC-ALICE.

[131] ALICE Collaboration. *Addendum to the Technical Design Report of the Time of Flight System (TOF)*. ALICE TDR 8 Addendum. CERN, Geneva, Switzerland, April 2002. ISBN 92-9083-192-8. CERN/LHCC 2002-016.

[132] ALICE Collaboration. Addendum to the technical design report of the dimuon forward spectrometer, 2000. URL https://aliceinfo.cern.ch/secure/system/files/documents/technical_coordination/tdr2-main.pdf.

[133] B. Abelev and The ALICE Collaboration. Technical design report for the upgrade of the alice inner tracking system. *Journal of Physics G: Nuclear and Particle Physics*, 41(8):087002, 2014. doi: 10.1088/0954-3899/41/8/087002. URL https://doi.org/10.1088/0954-3899/41/8/087002.

[134] G. Contin. Performance of the present alice inner tracking system and studies for the upgrade. *Journal of Instrumentation*, 7:C06007, June 2012. doi:

10.1088/1748-0221/7/06/C06007. URL https://doi.org/10.1088/1748-0221/7/06/C06007.

[135] D. Nouais, S. Beolè, M. Bondila, V. Bonvicini, P. Cerello, E. Crescio, P. Giubellino, M. Idzik, A. Kolozhvari, S. Kouchpil, E. Lopez Torres, M.I. Martinez, G. Mazza, S. Piano, C. Piemonte, A. Rashevsky, L. Riccati, A. Rivetti, F. Tosello, W.H. Trzaska, and R. Wheadon. The alice silicon drift detector system. *Nuclear Instruments and Methods in Physics Research Section A: Accelerators, Spectrometers, Detectors and Associated Equipment*, 501(1):119–125, March 2003. doi: https://doi.org/10.1016/S0168-9002(02)02020-X.

[136] P. Kuijer. The alice silicon strip detector system. *Nuclear Instruments and Methods in Physics Research Section A: Accelerators, Spectrometers, Detectors and Associated Equipment*, 447(1–2):251–256, 2000. doi: 10.1016/S0168-9002(00)00196-0. URL https://doi.org/10.1016/S0168-9002(00)00196-0. For the ALICE collaboration.

[137] M. Bregant, O. Borysov, L. Bosisio, P. Camerini, G. Contin, F. Faleschini, E. Fragiacomo, N. Grion, G.-V. Margagliotti, S. Piano, I. Rachevskaia, R. Rui, A.P. de Haas, R. Kluit, P.G. Kuijer, G.J.L. Nooren, C.J. Oskamp, A.N. Sokolov, A. van den Brink, F. Agnese, and G. Zinovjev. Assembly and validation of the ssd silicon microstrip detector of alice. *Nuclear Instruments and Methods in Physics Research Section A: Accelerators, Spectrometers, Detectors and Associated Equipment*, 566(1):18–21, October 2006. doi: 10.1016/j.nima.2006.05.024. URL https://doi.org/10.1016/j.nima.2006.05.024.

[138] Y. Zoccarato et al. Front end electronics and first results of the ALICE V0 detector. *Nucl. Instrum. Meth. A*, 626-627:90–96, 2011. doi: 10.1016/j.nima.2010.10.025.

[139] Ginés Martinez and for the ALICE collaboration. Physics of the muon spectrometer of the alice experiment. In *5TH INTERNATIONAL CONFERENCE ON PHYSICS AND ASTROPHYSICS OF QUARK GLUON PLASMA*, volume 50 of *Journal of Physics: Conference Series*, page 361, 2006. doi: 10.1088/1742-6596/50/1/049.

[140] P. Crochet and the ALICE Collaboration. The alice forward muon spectrometer. *Pramana*, 60(5):1051–1054, 2003.

[141] ALICE Collaboration. Alice dimuon forward spectrometer: Technical design report. Technical report, CERN, Geneva, 1999.

[142] Ginés Martinez and the ALICE Collaboration. The muon spectrometer of the alice experiment. *Nuclear Physics A*, 749:313–319, 2005. doi: 10.1016/j.nuclphysa.2004.12.059.

[143] Christian Finck and for Alice Muon Spectrometer collaboration. The muon spectrometer of the alice. In *5TH INTERNATIONAL CONFERENCE ON PHYSICS AND ASTROPHYSICS OF QUARK GLUON PLASMA*, volume 50 of *Journal of Physics: Conference Series*, page 397, 2006. doi: 10.1088/1742-6596/50/1/056.

[144] The ALICE collaboration. Performance of the alice vzero system. *Journal of Instrumentation*, 8:P10016, October 2013. doi: 10.1088/1748-0221/8/10/P10016.

[145] R. Brun, P. Buncic, F. Carminati, A. Morsch, F. Rademakers, and K. Safarik. Computing in alice. *Nuclear Instruments & Methods in Physics Research Section A-accelerators Spectrometers Detectors and Associated Equipment*, 502(1211 Geneva 23):339–346, 2003.

[146] CERN. Welcome to alice off-line project, 2023. URL https://alice-offline.web.cern.ch. Accessed: 15 October 2023.

[147] I. Hřivnáčová, D. Adamová, V. Berejnoi, R. Brun, F. Carminati, A. Fassó, E. Futó, A. Gheata, A. Morsch, and I. González Caballero. The virtual monte carlo. In *Proceedings of Computing in High Energy and Nuclear Physics (CHEP)*, La Jolla, California, 2003. ALICE Collaboration. 24-28 March 2003.

[148] R. Brun, F. Carminati, I. Hrivnacova, and A. Morsch. Virtual monte carlo. https://root.cern/root/vmc/, 2009. Last updated: 20 January 2009.

[149] PYTHIA Collaboration. Pythia 8 online manual, 2023. URL https://pythia.org//latest-manual/Welcome.html. Last accessed 15 April 2023.

[150] T. Sjostrand, S. Ask, J.R. Christiansen, R. Corke, N. Desai, P. Ilten, S. Mrenna, S. Presetel, C.O. Rasmussen, and P.Z. Skands. An introduction to PYTHIA 8.2. *Computer Physics Communications*, 191:159–177, 2015.

[151] Torbjörn Sjöstrand, Stephen Mrenna, and Peter Z. Skands. Pythia 6.4 physics and manual. *Journal of High Energy Physics*, 2006(05):026, 2006.

[152] G. Corcella et al. Herwig 6: An event generator for hadron emission reactions with interfering gluons (including supersymmetric processes). *Journal of High Energy Physics*, 2001(01):010, 2001.

[153] S. Bethke. Experimental tests of asymptotic freedom. *Progress in Particle and Nuclear Physics*, 58(2):351–386, 2007.

[154] S. Agostinelli, J. Allison, K. Amako, J. Apostolakis, H. Araujo, P. Arce, M. Asai, D. Axen, S. Banerjee, G. Barrand, et al. Geant4—a simulation toolkit. *Nuclear*

Instruments and Methods in Physics Research Section A: Accelerators, Spectrometers, Detectors and Associated Equipment, 506(3):250–303, 2003. doi: 10.1016/S0168-9002(03)01368-8.

[155] J. Allison, K. Amako, J. Apostolakis, P. Arce, M. Asai, T. Aso, E. Bagli, A. Bagulya, S. Banerjee, G. Barrand, B. R. Beck, A. G. Bogdanov, D. Brandt, J. M. C. Brown, H. Burkhardt, Ph. Canal, D. Cano-Ott, S. Chauvie, K. Cho, G. A. P. Cirrone, et al. Recent developments in geant4. *Nuclear Instruments and Methods in Physics Research Section A: Accelerators, Spectrometers, Detectors and Associated Equipment*, 835:186–225, 2016. doi: 10.1016/j.nima.2016.06.125. Under a Creative Commons license.

[156] Richard D. Ball, Stefano Carrazza, Juan Cruz-Martinez, Luigi Del Debbio, Stefano Forte, Tommaso Giani, Shayan Iranipour, Zahari Kassabov, Jose I. Latorre, Emanuele R. Nocera, Rosalyn L. Pearson, Juan Rojo, Roy Stegeman, Christopher Schwan, Maria Ubiali, Cameron Voisey, and Michael Wilson. An open-source machine learning framework for global analyses of parton distributions, 2021.

[157] Pavel M. Nadolsky, Hung-Liang Lai, Qing-Hong Cao, Joey Huston, Jon Pumplin, Daniel Stump, Wu-Ki Tung, and C.-P. Yuan. Implications of cteq global analysis for collider observables. *Phys. Rev. D*, 78:013004, Jul 2008. doi: 10.1103/PhysRevD.78.013004. URL https://link.aps.org/doi/10.1103/PhysRevD.78.013004.

[158] M. Maire. Experiments simulation of particles physics: The GEANT3 software. In *Instrumental Nuclear Physics: Elements for a Proper Choice*, pages 349–372, Maubuisson, France, September 1994. Joliot-Curie School of Nuclear Physics. 12–17 September 1994, Report number: IN2P3–94-03.

[159] R Brun, F Bruyant, M Maire, A C McPherson, and P Zanarini. GEANT 3. Technical report, CERN, Geneva, 1987. URL https://cds.cern.ch/record/1119728.

[160] Stephen Myers and Emilio Picasso. The lep collider. *Scientific American*, 263(1):54–61, 7 1990. URL https://www.jstor.org/stable/24996863.

[161] M. Breidenbach. Overview of the sld. *IEEE Transactions on Nuclear Science*, 33 (1):46–50, 1986. doi: 10.1109/TNS.1986.4337045.

[162] L. Evans. The large hadron collider. *Philosophical Transactions: Mathematical, Physical and Engineering Sciences*, 370(1961):831–858, 2012. URL http://www.jstor.org/stable/41348317.

[163] Stephen Holmes, Ronald S Moore, and Vladimir Shiltsev. Overview of the tevatron collider complex: goals, operations and performance. *Journal of Instrumentation*, 6:T08001, 8 2011. doi: 10.1088/1748-0221/6/08/T08001. Published 2 August 2011.

[164] Torbjörn Sjöstrand, Stefan Ask, Jesper R. Christiansen, Richard Corke, Nishita Desai, Philip Ilten, Stephen Mrenna, Stefan Prestel, Christine O. Rasmussen, and Peter Z. Skands. *PYTHIA 8 Online Manual*, 2023. URL https://pythia.org/latest-manual/Welcome.html.

[165] J. Rojo P. Skands, S. Carrazza. Tuning pythia 8.1: The monash 2013 tune. *European Physics Journal C*, 74(3024), 2014. doi: https://doi.org/10.1140/epjc/s10052-014-3024-y. URL https://link.springer.com/article/10.1140/epjc/s10052-014-3024-y.

[166] F Antinori. Naming scheme for alice trigger classes. ALICE Collaboration, 2008. URL https://alice-offline.web.cern.ch/sites/default/files/uploads/trigger/class-naming-01.pdf. Version 0.1 (draft).

[167] Md Samsul Islam. *Study of heavy flavour decay muons at forward rapidity in proton-proton and heavy-ion collisions at LHC energies*. Phd thesis, Saha Institute of Nuclear Physics, High Energy Nuclear & Particle Physics Division, Saha Institute of Nuclear Physics, 2022. URL https://cds.cern.ch/record/2848125. Presented 07 Oct 2022.

[168] Joyful Elma Mdhluli. *Probing heavy-quark production vs charged-particle multiplicity in pp collisions at* $\sqrt{s} = 5.02$ *TeV with ALICE*. Doctor of philosophy, University of the Witwatersrand, Johannesburg, 2 2023. URL https://hdl.handle.net/10539/37489. Supervisor: Prof. Zinhle Buthelezi; Co-Supervisors: Dr. Siegfried Foertsch, Prof. Deepak Kar.

[169] ALICE Collaboration. Heavy flavour decay muon production at forward rapidity in proton-proton collisions at $\sqrt{s} = 7$ TeV. *Physics Letters B*, 708:265–275, 2012.

[170] Zuman Zhang, Sha Li, Ning Yu, and Zhong Zhu. Heavy-flavor hadron decays producing muon cross sections in pp collisions at high transverse momentum. *Frontiers in Physics*, 11:1188989, 2023. doi: 10.3389/fphy.2023.1188989.

[171] CTEQ Collaboration. The coordinated theoretical-experimental project on qcd. https://www.physics.smu.edu/scalise/cteq/, November 2023. Accessed: 17 November 2023.

Appendices

Appendix A: Code Repository

For detailed access to all code and scripts developed and utilised during this research, please refer to the dedicated GitHub repository:

https://github.com/Mokhatla/alice-hf-muon-2025

This repository contains all relevant code, documentation, and supplementary materials, providing a comprehensive overview of the computational methodologies applied in this thesis.

Appendix B: Overview of PYTHIA

Programme Flow

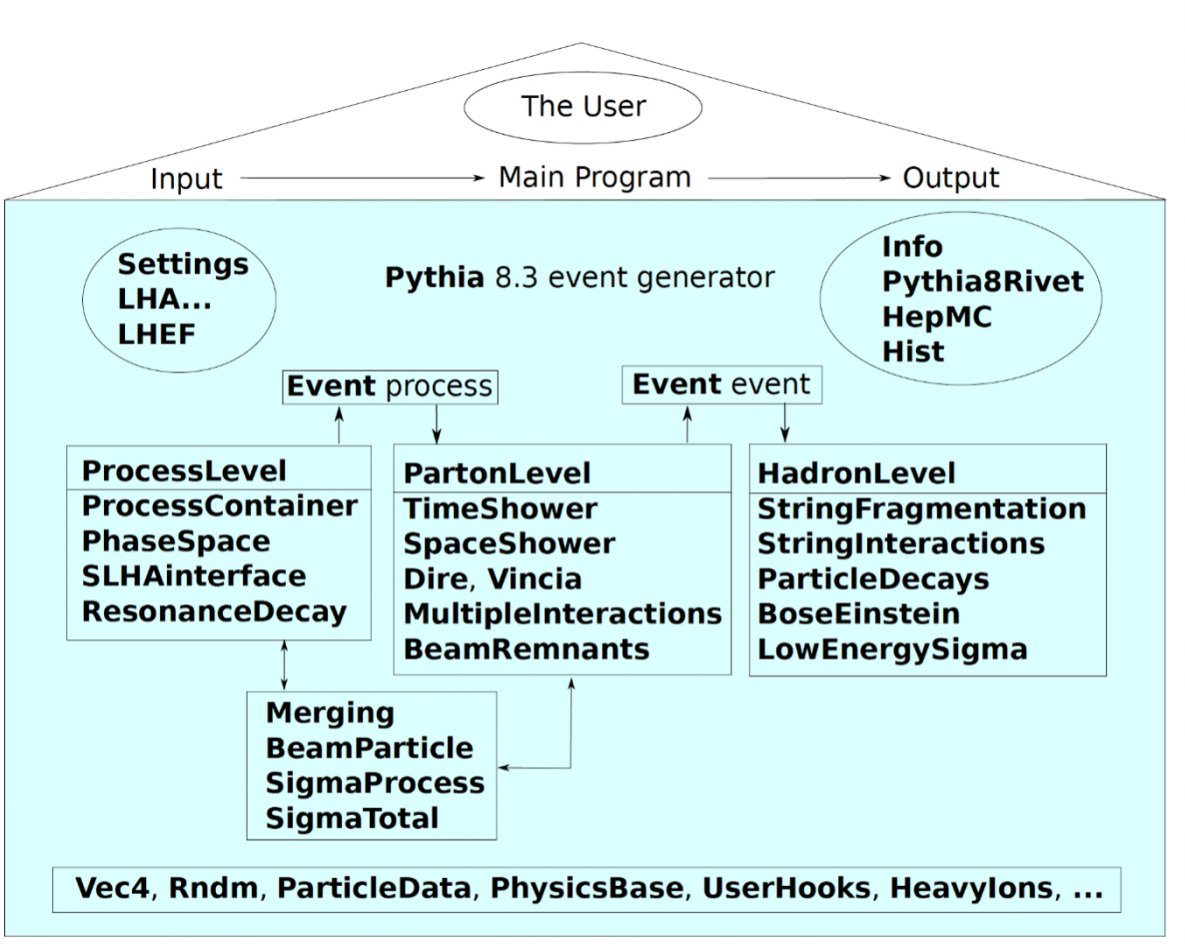


Figure 4: Pythia 8.3 programme structure with its main C++ classes.[13]

The **Pythia8::Pythia** class is the main class that manages the overall programme flow of the event generation. From a sequential perspective, the execution of a PYTHIA script consists of three phases: initialisation, generation, and finishing. During the initialisation phase, PYTHIA configures the requisite components for the simulation, such as the specific hard process to be simulated and the beam particles and their energies. This phase also involves configuring the parameters for the PDFs, settings and parameters for the event generation (such as the choice of the underlying physics models, showering algorithms, and hadronisation models).

PYTHIA 8 manages initialisation and programme flow using different classes, methods and functions. When an instance of the **Pythia8::Pythia** class is created, it initialises the internal data structures and sets the default values for the simulation settings. The user can then set the desired values for the settings by calling the appropriate methods or reading them from an external file. The **Pythia** class also provides a method to initialise the event generation process. This method sets up the initial state of the event, such as the energy and momentum of the incoming protons. It configures the different sub-systems of the event generator, such as the parton shower and hadronisation.

Generation is the main phase of the simulation, where PYTHIA generates a series of events based on the specified hard process and input parameters. Once the initialisation process is complete, calling the **Pythia8::Pythia** class's **next()** method begins the event generation process. This process performs the main event generation steps, such as the parton shower, hadronisation, and decay of the produced particles. The **next()** method will generate one event at a time until the user decides to stop the event generation. The user can also use the **Pythia8::Pythia** class event method to access the generated events. PYTHIA simulates the hard scattering process for each event, followed by initial and final state radiation (ISR and FSR), multiple parton interactions (MPI), beam remnants, and colour reconnection. After the parton-level simulation, PYTHIA moves on to the hadronisation process, where partons are transformed into colour-neutral hadrons. Finally, the decays of unstable hadrons and any additional final-state interactions are simulated, producing a set of simulated events that can be analysed further or compared to experimental data. In the finishing phase, PYTHIA terminates the simulation by calculating various event statistics, such as the total cross-section, the number of accepted and generated events, and any pre-defined histograms or observables. This phase helps users summarise the simulation results and analyse the data to better understand the underlying physics processes.

The Event Class

The Event class is a central component of the Pythia event generator framework, responsible for managing and storing the information related to a single event in a simulation. The Event class serves as a container for all the particles produced during the event, and it keeps track of their properties, interactions, and relationships. An instance of Pythia contains two members, process and event. The process member stores details of all the hard processes. The second member, event, stores the entire event history.

The Event class is the main result of a programme and comprises an array of particles, such that each particle has its own index within the event. The index is an integer value representing the particle's position in the list, starting from 0. When users use the index to access a particle, they can access all the methods and properties associated with that particle. If a user wants to access a particle with the index **`i`** within the event generated by Pythia, the user can use the following syntax: **`pythia.event[i]`**. Once the particle has been accessed using its index, a user can call various methods to retrieve or modify its properties. For instance, there are methods to access the particle's identity code, status code, four-momentum, mother and daughter indices, and more. For example, a user can retrieve a particle's transverse momentum (pT) using **`pythia.event[i].pT()`**. This data structure allows users to easily iterate through all the particles in an event, analyse their properties, and perform manipulations or computations on the particle data.[149]

Particle Data

Particle data is represented by the class **`Pythia8::ParticleData`**. This class stores information about each particle, such as its mass, spin, charge, and decay properties. The particle database is initialised with default values based on PDG's data. This information is stored in a particle data table, a collection of **`Pythia8::ParticleData`** objects.

Pythia's event generation process relies heavily on this information to accurately simulate particle collisions, decays, and other phenomena. By leveraging the high-quality data provided by PDG, Pythia ensures that its simulations are consistent with current experimental results and theoretical predictions in particle physics. Users can access and modify the particle properties in Pythia through the **`ParticleData`** class, tailoring the event generation to their specific research needs.

PYTHIA 8's particle data scheme stores various properties for each particle and uses this information to simulate the production and decay of particles at the multiple stages of high-energy collisions. The properties stored in **`Pythia8::ParticleData`** class allow PYTHIA 8 to generate events consistent with the experimental data and to extract information about the particles produced in the collisions. PYTHIA 8 uses the

Pythia8::Event class to store the final state particles. The **Pythia8::Particle** class stores information about individual particles. These classes are used to access and manipulate the particle data in PYTHIA 8.[149]

Configuration Settings

Table 4.1 outlines the fundamental configuration that is consistently implemented in all our simulations. Within this framework, the centre-of-mass energy and the PDF variables were subject to change for each simulation run. The centre-of-mass energy is designated by **Beams:eCM = 13000**. The Parton Distribution Function (PDF) used in the simulation, represented by **PDF:pSet**, can be assigned various values corresponding to different PDFs. In our simulations, we used CTEQ6.6 PDF, designated by **PDF:pSet = 7**, and NNPDF2.3 and NNPDF3.1, represented as options 13 and 19, respectively.[164][101][156]

- **"HardQCD:hardccbar = on"** and **"HardQCD:hardbbbar = on"**: These switches enable the hard production of charm-anticharm and bottom-antibottom quark pairs, respectively.
- **"4:mayDecay = true"** and **"-4:mayDecay = true"**, **"5:mayDecay = true"** and **"-5:mayDecay = true"**: These flags allow for the decay of charm and bottom quarks and their antiparticles.
- **"321:mayDecay = true"** and **"-321:mayDecay = true"**, **"211:mayDecay = true"** and **"-211:mayDecay = true"**: These settings allow for the decay of kaons and pions and their antiparticles.
- **"SoftQCD:nonDiffractive = on"**: This switch enables non-diffractive processes which constitute sources of heavy-flavour production.
- **"ColourReconnection:reconnect = on"**: This setting enables the colour reconnection mechanism.
- **"ColourReconnection:mode = 0"**: This setting sets the colour reconnection to operate under the Multi-Parton Interaction (MPI) based scheme as implemented in the original PYTHIA 8 model.
- **"ColourReconnection:range = 1.8"**: The parameter, set by default at 1.8, with a minimum value of 0 and a maximum of 10, determines the likelihood of colour reconnections in particle collision events. It is not a measure of physical distance but rather a probabilistic gauge. A higher value of this parameter indicates an increased propensity for reconnections.
- **"PhaseSpace:pTHatMin = ptHatMin"** and **"PhaseSpace:pTHatMax = ptHatMax"**:

These settings define the allowed range for transverse momentum transfer during event generation. We restrict the kinematic phase space for the generated hard-scattering events by specifying a minimum and a maximum, thereby controlling the simulated interactions' momentum scale.

- **`"Random:setSeed = on"`**: This command enables the manual setting of the seed for the random number generator.
- **`int randomSeed = std::chrono::system_clock::now()... % 900000000 + 1`**: This line of code generates a random seed based on the current time in nanoseconds. This seed is then modulated by 900,000,000 to ensure it falls within the valid range for the Pythia random number generator, and 1 is added to avoid a zero value.
- **`std::string seedString = "Random:seed = " + std::to_string(randomSeed); "pythia.readString(seedString)"`**: This command sets the generated random seed for the Pythia random number generator. The seed invokes the random number generator algorithm.

Random Seeds

Using different seeds for each core is critical to ensure that each core produces a unique sequence of pseudo-random numbers. This provides each simulation with distinct initial conditions, leading to variation in the generated events. It is crucial not to use the same seed for each core to prevent correlations between different simulations. If identical seeds were used, each simulation would produce the same sequence of random numbers and identical events, which is undesirable for a valid and diverse simulation.

The method of choosing the seeds also matters. For instance, selecting seeds in a simple sequence (like 1, 2, and 3) can occasionally lead to correlations due to the properties of the random number generator's algorithm. Thus, our seeds were chosen randomly using a well-established seed generation method. In PYTHIA, the seed for the random number generator can be set using the **`Random:setSeed`** and **`Random:seed`** commands. The first command decides whether a user-set seed should be used every time the **`Pythia::init`** routine is called, while the second command specifies the seed to be used. Pythia allows seeds between 1 and 900,000,000, resulting in unique random number sequences. Finally, the **`Parallelism:seeds`** command can be used to define the seeds for each Pythia object in parallel simulations using **`PythiaParallel`**.

By using a different seed for each core, each simulation becomes unique. This strategy avoids the issue of duplicate results and allows for a more extensive exploration of the potential event space in pp collisions.

Appendix C: ALICE Monte Carlo Productions with AliROOT

ALICE MC Productions Using AliROOT & PYTHIA

The trigger conditions in our analysis task are implemented to match the low-p_{T} trigger, and are executed in the code snippet `if(fTrack->GetMatchTrigger()!=2) continue;`, which is a part of the muon selection process. This snippet evaluates each muon track to ascertain if it meets the predefined trigger conditions. The method `GetMatchTrigger()` assesses the muon track against the trigger conditions and returns a value indicating the level of match:

- A return value of `0` means the muon track does not match any triggers;
- `1` signifies a match but failing p_{T} cut,
- `2` indicates a match with a Low p_{T} cut,
- `3` represents a match with a High p_{T} cut.

Based on this return value, the muon track is either accepted or rejected for further analysis. This conditional check is crucial for filtering out muon tracks that do not meet our p_{T} criteria.

Analysis Task Configuration

The `runAnalysis.C` file contains the settings and instructions required to run the analysis task on the CERN grid. Some of the key settings are listed below:

- `alienHandler->SetGridDataDir("/alice/sim/2018/LHC18j3")`: This line sets the directory on the Grid where your data files are stored. In this case, the data are from the LHC run in 2018, specifically the "LHC18j3" dataset.
- `alienHandler->SetDataPattern("AOD209/*/AliAOD.Muons.root")`: This line tells the system the pattern of the file names to look for in the data directory. In this case, it is looking for root files containing AOD (Analysis Object Data) in any subdirectory of the AOD209 directory. Specifically, it searches for files that contain muon data.
- `totruns += AddGoodRuns(alienHandler, "LHC15n")`: This line adds the number of good runs from the specified LHC period ("LHC15n") to the `totruns` variable. The "good runs" are those runs that meet specific quality criteria.

- `alienHandler->SetMaxMergeStages(2)`: This line sets the maximum number of stages in the merging process. When the analysis is run on the Grid, it is often divided into several jobs. The results of each job need to be merged, which can take multiple stages. This line sets the maximum number of merging stages to 2.

These settings allow the script to find and process the correct data files and set other parameters for analysis.